Noise and degradation of amorphous silicon devices

Druk: PrintPartners Ipskamp - Enschede

Noise and degradation of amorphous silicon devices

Ruis en degradatie van amorf silicium structuren

(met een samenvatting in het Nederlands)

PROEFSCHRIFT

TER VERKRIJGING VAN DE GRAAD VAN DOCTOR AAN DE UNIVERSITEIT UTRECHT OP GEZAG VAN DE RECTOR MAGNIFICUS, PROF. DR. W.H. GISPEN, INGEVOLGE HET BESLUIT VAN HET COLLEGE VOOR PROMOTIES IN HET OPENBAAR TE VERDEDIGEN OP MAANDAG 6 OKTOBER 2003 DES MIDDAGS TE 12.45 UUR

DOOR

JEROEN PIETER ROELOF BAKKER

GEBOREN OP 16 FEBRUARI 1976, TE OSS

Promotor: Prof.Dr. J.I. Dijkhuis
Faculteit Natuur- en Sterrenkunde
Debye Instituut
Universiteit Utrecht

CIP-gegevens Koninklijke Bibliotheek, Den Haag

Bakker, Jeroen Pieter Roelof

Noise and degradation of amorphous silicon devices/
Jeroen Bakker. - Utrecht: Universiteit Utrecht,
Faculteit Natuur- en Sterrenkunde, Debye Instituut
Proefschrift Universiteit Utrecht.
Met samenvatting in het Nederlands.
ISBN 90-393-3303-3
Trefw.: halfgeleiders / silicium / amorf / ruisspectroscopie /
degradatie.

Opgedragen aan mijn grootvaders
Pieter Jacobus Bakker en Roelof Timmerman

Contents

1 Introduction **10**
- 1.1 Hydrogenated amorphous silicon . . . 10
  - 1.1.1 General properties . . . 10
  - 1.1.2 Electronic properties . . . 11
  - 1.1.3 Degradation of *a*-Si:H . . . 14
- 1.2 Noise spectroscopy . . . 16
- 1.3 Noise measurements on amorphous silicon . . . 17
  - 1.3.1 $1/f$ noise in coplanar structures of doped *a*-Si:H . . . 18
  - 1.3.2 $1/f^{\alpha}$ noise in coplanar structures . . . 19
  - 1.3.3 $1/f^{\alpha}$ noise in sandwich structures of undoped *a*-Si:H . 20
- 1.4 Aim and outline of this thesis . . . 23

2 Devices, conductivity and setup **25**
- 2.1 Devices . . . 25
  - 2.1.1 Positioning of the device in the setup . . . 25
  - 2.1.2 Contact requirements . . . 25
  - 2.1.3 Device structure . . . 26
  - 2.1.4 Device preparation . . . 26
  - 2.1.5 Device properties . . . 28
- 2.2 Device simulations . . . 29
  - 2.2.1 Simulation program . . . 29
  - 2.2.2 Simulation of J-V curves . . . 30
  - 2.2.3 Band bending . . . 32
  - 2.2.4 Uniform resistivity layer . . . 33
- 2.3 Setup . . . 35

3 Study of g-r noise **37**
- 3.1 Introduction . . . 37

3.2 Ingredients of g-r noise theory . . . 39
3.2.1 Relaxation . . . 40
3.2.2 Multi-level model . . . 41
3.2.3 Green's function procedure . . . 43
3.3 Calculation of g-r noise intensity . . . 45
3.3.1 Computational details . . . 45
3.3.2 Rates and spectra . . . 47
3.4 Discussion of the model assumptions . . . 52
3.5 Conclusion and perspectives . . . 54

4 Long-range potential fluctuations 55
4.1 Introduction . . . 55
4.2 Theory . . . 58
4.2.1 Autocorrelation function . . . 58
4.2.2 Single layer approach . . . 59
4.2.3 Screening . . . 61
4.2.4 Description of deep defects . . . 64
4.2.5 Activation barriers . . . 67
4.2.6 Rates and rate equations . . . 68
4.2.7 From potential fluctuations to noise . . . 70
4.3 Temperature dependence . . . 73
4.3.1 Noise spectra . . . 73
4.3.2 Distribution of potential barriers . . . 75
4.3.3 Dutta-Dimon-Horn analysis . . . 76
4.3.4 Discussion of Dutta-Dimon-Horn analysis . . . 78
4.4 General discussion . . . 78
4.5 Conclusion . . . 80
4.6 Appendix: Equilibrium statistical description . . . 81

5 Further experimental evidence 83
5.1 Introduction . . . 83
5.2 Devices . . . 85
5.3 Experimental results . . . 86
5.4 Conclusion . . . 90

6 Noise study of degradation 91
6.1 Motivation . . . 91
6.2 Measurements on silver-epoxy contacted devices . . . 92
6.2.1 Measurement conditions . . . 92

6.2.2 Effect of degradation . . . 92
6.3 Analysis of noise data of silver-epoxy contacted devices . . . 93
6.3.1 Parallel resistances . . . 93
6.3.2 Extraction of the degradation term in the noise . . . 94
6.3.3 Noise data of degraded part . . . 95
6.4 Measurements in wire-bonded devices . . . 95
6.4.1 Measurement conditions . . . 96
6.4.2 Device simulations . . . 97
6.4.3 SCLC analysis . . . 99
6.4.4 Noise measurements in wire-bonded devices . . . 99
6.5 Conclusion . . . 100

7 Diffusion noise in TFTs **103**
7.1 Introduction . . . 103
7.1.1 Thin-film transistors . . . 103
7.1.2 $1/f$ noise in the on-state of TFTs . . . 104
7.1.3 Aim . . . 105
7.2 TFT characterization . . . 105
7.2.1 TFT fabrication . . . 105
7.2.2 Linear transfer characteristics . . . 106
7.3 Noise measurements . . . 108
7.3.1 Noise in the above-threshold regime . . . 108
7.3.2 Noise spectra in the sub-threshold regime . . . 108
7.4 1D Diffusion noise . . . 109
7.4.1 1D diffusion noise theory . . . 109
7.4.2 Fits to the spectral kink . . . 110
7.4.3 Mobility from noise intensity . . . 111
7.4.4 Total number N from noise intensity . . . 112
7.4.5 Mobility and N directly computed from the conduction only . . . 114
7.5 Discussion . . . 115
7.5.1 Diffusion noise phenomenon . . . 115
7.5.2 Mobility values . . . 115
7.6 Conclusion and outlook . . . 116

References **117**

Summary **123**

Samenvatting voor niet-vakgenoten **127**

Dankwoord **131**

Curriculum Vitae **135**

Chapter 1

Introduction

1.1 Hydrogenated amorphous silicon

1.1.1 General properties

The crystalline form of the material *silicon* is well known for numerous applications in information technology. The material is used to make structures with a specific purpose, *devices*. The manufacturing of silicon devices relies very much on the advantagous properties of oxides and nitrides, which are insulators, allowing for the fabrication of structures with alternating semiconductor-insulator layers. In that way, charge carriers can be effectively confined and/or controlled. The addition of various concentrations of dopant atoms yields silicon layers with the desired electron concentration. Various combinations of doped, intrinsic, insulator and contact layers has lead to a multitude of devices. A few examples of crystalline silicon (*c*-Si) devices are the transistor, the optical sensor, and the solar cell.
Two types of devices play a role in this work: the solar cell and the thin film transistor. A solar cell consists at least of layers of *p*-type doped and *n*-type doped material, and sometimes of intrinsic material in between. Light generates mobile electrons and holes, which are separated by an internal electric field and collected at the contacts. In the field-effect-transistor (FET) a variable electric field at the semiconductor/insulator interface is used to control the concentration of charge carriers in a conducting channel near the interface. The current through the conducting channel can even be switched on and off by application of a properly chosen electric field.
The invention of the disordered variant of crystalline silicon (*c*-Si), *amorphous silicon* (*a*-Si) provided a perspective to reduce material costs of solar

cells, since it can be deposited as thin layers, on large area's while *c*-Si solar cells require wafers, which are relatively thick and expensive. Whereas *c*-Si has an indirect bandgap, *a*-Si can be considered as a direct semiconductor. Further, the amorphous structure exhibits a significant variation of bond angles between the atoms, which turns out to lead to dangling bonds with a large defect density in the band gap, which enhances electron-hole recombination, and limits the conductivity of the material. However, defects can be passivated to a large extent when hydrogen is incorporated in the amorphous network during growth.
Hydrogenated amorphous silicon (*a*-Si:H) can be formed by dissociation of a mixture of silane (SiH_4) and hydrogen (H_2) in a plasma deposition process. The concentration of deep defects in *a*-Si:H is reduced by the presence of hydrogen, but still orders of magnitude higher than in *c*-Si. Trapping of charge carriers by the deep defects in *a*-Si:H limits the efficiency of solar cells and the mobility of thin film transistors (TFTs). The doped layers which are necessary in these devices are created by addition of phosphorus- and boron-containing gases. For a review of *a*-Si:H see Ref. [1].

1.1.2 Electronic properties

The randomness of the amorphous network leads to the presence of electronic states below the conduction band, which are localized. These states can capture electrons and are called *tail states*, which refers to the exponential tail representing their distribution in energy. Optical absorption measurements allow for sensing the density of states profile, which rapidly decreases below the conduction band. In a logarithmic representation of the density of states in Fig. 1.1, the exponential distributions of tail states near the band edges are straight lines. According to Mott, the transition between localized states and extended states is sharp and marks the energy above which electrons are mobile [2]. In view of that, the conduction band edge E_C is often called the *mobility edge*. However, the properties of states near the mobility edge are actually more complicated (see Ref. [1]). The theory of conductivity near the mobility edge in disordered systems has been debated for many years and is still not completely agreed on. Nevertheless, for practical purposes, the conduction of *a*-Si:H films can well be described in terms of the mobility edge. The conduction appears to be thermally activated with a barrier $E_C - \mu$, in case electrons are the majority carriers. Here, μ is the chemical potential, which is defined as the average energy required to add a single electron to the system. It is the widespread practice to refer

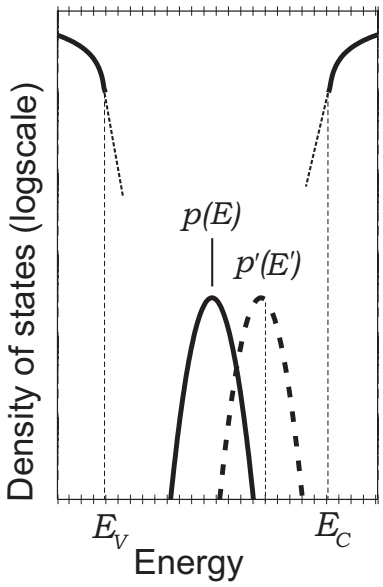

FIGURE 1.1: Schematic presentation of the density of states in the center of the band gap, including extended states below the valence band edge E_V and above the conduction band edge E_C, tail states within the band gap, and two Gaussian distributions of defect states. $p(E)$ is related to transitions involving a single electron and $p'(E')$ involves a second electron, shifted by the correlation energy U, i.e. $E' = E + U$.

to the chemical potential of a semiconductor as "the Fermi level", although there is a subtle difference [3]. The Fermi level namely is the energy level where the electron occupation is one-half. The Fermi level coincides with μ at zero temperature. Also at higher temperatures, where the distribution of electrons is spread thermally, the Fermi level is shifted and effectively coincides with μ. Given the continuous distribution of levels in the gap of an amorphous semiconductor, the Fermi level effectively tracks an existing level where the occupation number equals one-half. In the context of amorphous semiconductors "Fermi level" and "chemical potential" are thus synomyms. We choose to use the term "chemical potential" in this thesis. In case of crystalline semiconductors, which have no or very few discrete (impurity) levels in the band gap, the difference between the two terms is more pronounced, since the Fermi level in general does not coincide with an existing level in the gap. Therefore the term "chemical potential" is preferred in case of crystalline semiconductors [3].
In intrinsic (undoped) *a*-Si:H the chemical potential is located in the midgap region. Dangling silicon bonds constitute the deep defects, which are close to midgap and may contain up to two electrons. The dangling bonds can be singly occupied (D^0), doubly occupied (D^-) or empty (D^+). To put a second electron on a singly occupied defect requires an extra energy U, the correlation energy. All existing defect models assume a Gaussian energy distribution of deep defects. The simplest defect model uses two Gaussian distributions; one of these is related to transitions to and from the doubly occupied defect states and is therefore shifted in energy by U (see Fig. 1.1). Above the conduction band edge the density of states deviates from the square-root dependence on the energy in crystalline materials [1].
An important phenomenon observed in some disordered structures is *percolation*. Due to the random position of the atoms in the network, the potential landscape depends strongly on the local configuration of the atoms. Electrons, when injected in the structure, tend to follow a current path through the lower (localized) energy states. At a specific energy, the percolation threshold, excitation over the saddle points of the potential landscape is possible and various parts of the film get connected, resulting in a conductive flow. A percolation description, however, turns out not to fully describe the physics around the mobility edge of *a*-Si:H.
The existence of a random distribution of charged deep defects in undoped *a*-Si:H results in long-range *potential fluctuations* of the conduction and valence band edges. The amplitude and spatial frequencies of the potential fluctuations are different for undoped, doped and compensated amorphous

silicon.
The electronic properties of hydrogenated amorphous silicon are usually studied below the annealing temperature ($\sim$ 420 K), where the amorphous structure is 'frozen in'. At temperatures below 200 K variable-range hopping in tail states limits the conduction of this material [4]. In the cases of *a*-Si and silicon suboxides, which have defect densities larger than the typical defect density of *a*-Si:H , variable-range hopping is observed up to room temperature [5].

1.1.3 Degradation of *a*-Si:H

A serious drawback for commercial application of *a*-Si:H in devices is *degradation* of the electronic properties over time due to defect creation. In case of solar-cell devices, prolonged exposure to light leads to breaking of weak Si-Si bonds via electron-hole recombination. As a concequence, newly created defects can lead to either rotation or breaking of Si-H bonds. In a degraded solar cell the defect density is thus increased, which enhances total recombination and reduces the *efficiency*. Degradation in *a*-Si:H is a reversible process and called the Staebler-Wronski effect [6]. By thermal annealing the material can reach a state equivalent to the original state.
In case of thin-film transistors (TFTs), where electrons are injected in the channel region of a transistor due to a high applied voltage at the gate contact, trapping is enhanced, Si dangling bonds are created, which leads to a shift of the threshold voltage. The threshold voltage corresponds to the gate voltage, at which all deep defects are filled. Gate stressing creates a higher defect density and a *threshold-voltage shift*. It is believed that the defect-creation reactions in solar cells and TFTs have a common origin [7].
A large number of experimental studies on defect creation kinetics of *a*-Si:H resulted in an empirical law: the defect density depends sub- linearly on both the illumination time and power and saturates after a sufficiently long period of illumination. Branz formulated microscopic kinetic equations with a corresponding exact solution [8]. Deane *et al.* have introduced the thermalization energy concept for defect creation, and measured the activation energy and attempt-to-escape frequency of this process [9]. Compared to defect creation, thermal annealing has a much higher energy barrier and a higher attempt-to-escape frequency [10]. That suggests that defect creation and annealing are caused by a different mechanism. Progress in the description of defect creation kinetics has been made by recognizing that the reverse reaction by thermal annealing is not negligible at finite temperature

(see Refs. [10, 11]).
More than ten microscopic models have been proposed for the microscopic mechanism that would explain the Staebler-Wronski effect [7] and still, there are ongoing discussions in literature about the microscopic description of defects and the degradation mechanism. An important issue is the distance traveled by hydrogen atoms after defect creation. Electron spin resonance (ESR) measurements are instrumental in discriminating between the models. When hydrogen atoms would remain at the bond- centered position, the separation between the dangling bond and hydrogen atom would be about 0.2 nm, which would lead to a measurable hyperfine broadening of the ESR signal, but which has never been observed [12]. This experimental fact seems to favor mechanisms involving long-range hydrogen motion. In the *hydrogen collision model*, mobile H travels through the network until it "collides" with another mobile H, thus accounting in a natural way for the wide separation between the dangling bond and hydrogen as indicated by ESR experiments. As mentioned before, Branz' model also explains the observed defect creation kinetics [8].
Recently, Powell *et al.* proposed a solution for the inconsistency of their local defect-pool model [13] with ESR data. They suggested that the hydrogen atom is located in the tetrahedral-like site instead of the bond centered site in the amorphous network [7]. The microscopic mechanism for defect creation proposed by Powell *et al.* is as follows [7]: light or gate bias (in case of TFTs) causes accumulation of electron- hole pairs and electrons, respectively, on short, weak Si-Si bonds, which then break due to released energy from recombinations. A hydrogen atom from another, neighboring weak Si-Si bond then moves to the tetrahedral-like site of the broken Si-Si bond. The *improved defect-pool model* takes the chemical equilibrium description of the defects in the three different charge states (+,0,-) into account [13]. The related hydrogen density of states is described in Ref. [14]. Defect formation leads to an energy shift of the peak of formed defects, consistent with a minimum free energy. In other words, the ratios between the three kinds of newly created defects depend on the location of the chemical potential. In doped layers, the chemical potential is located close to the band edge, resulting in a surplus of defect states at energies near the opposite band edge. Without the defect-pool model that observation would have remained a mystery.

1.2 Noise spectroscopy

The main experimental technique used in this thesis is electrical noise spectroscopy, which turns out to complement standard conductivity measurements. Electrical noise measurements analyze the amplitude and the specific time constants of spontaneous electrical fluctuations. The coherence of a noise signal $V(t)$ is revealed by transforming it into the frequency domain. Experimentally, $V(t)$ is measured an its autocorrelation function $\langle V(t)V(0)\rangle$ computed, which is subsequently Fourier transformed to obtain the noise spectrum $S_V(f)$. The mathematical connection is the so-called Wiener-Khintchine theorem [15], which reads

$$S_V(f) \;=\; 4\int_0^\infty \langle V(t)V(0)\rangle \cos(2\pi f t)\; dt. \tag{1.1}$$

Electrical noise can be classified in equilibrium and non-equilibrium noise, corresponding to noise in absence or presence of current. In zero current conditions, thermal velocity fluctuations of charge carriers lead to *thermal noise*, which has a noise level proportional to temperature and film resistance. Since the spectra have equal intensity in the full frequency range, it is called 'white noise' or Johnson-Nyquist noise. Thermal noise is usually subtracted from the total noise intensity to study the excess noise.
In the presence of current, several types of non-equilibrium noise can exist, either induced by current, or originating from resistance fluctuations. *Shot noise* is a fundamental type of noise which corresponds to current fluctuations of uncorrelated charged particles, and depends linearly on current. It leads to a white current noise spectrum and is commonly found in e.g. semiconductor diodes. Two examples of resistance fluctuations with comparable noise spectra are *random telegraph signal noise* (RTSN) and generation-recombination (g-r) noise. These two classes of noise signals can only be distinguished because of their different behavior in the time-domain. In case of RTSN, the device resistance fluctuates as a result of an individual random fluctuator which can occupy two different states. The measured time-trace of the voltage over the device will show random switching between two levels. The average time the system spends in each of the two states are denoted τ_{up} and τ_{down}, corresponding to the voltage level, which switches between up or down. The effective time τ_{eff} which appears as a cut-off frequency in the noise spectrum is given by [16]

$$\frac{1}{\tau_{eff}} \;=\; \frac{1}{\tau_{up}} + \frac{1}{\tau_{down}}. \tag{1.2}$$

The effective frequency $1/(2\pi\tau_{eff})$ separates two parts of the *Lorentzian spectrum*: a part at lower frequencies, which is white, and a part with spectral dependence $1/f^2$ at higher frequencies.
In contrast, the voltage signal of *generation-recombination noise* is in general uncorrelated due to the presence of more than two (uncorrelated) levels. Here, the fundamental processes are capture and emission transitions of charge carriers between trap and/or band levels [17]. When a fluctuation causes an excess in the number of majority carriers, the time it takes to restore that fluctuation, and reach the average number, is characterized by this exponential relaxation time τ. The relaxation time τ in g-r noise has the same role in the noise spectrum as the effective time in RTSN. For a process characterized by a single relaxation time, the spectrum is Lorentzian. In case of thermally activated processes and a broad distribution of energy levels the spectrum will be $1/f$ [18]. However, in many cases Fermi statistics imply a narrow effective distribution of relaxation times, i.e. over a range of $\sim 4k_BT$ [19], and the spectrum is Lorentzian again.
Generally, the transport of charge carriers in a semiconductor with traps can be described by taking generation-recombination, drift, and diffusion into account [17]. In the special case where diffusion is the only relevant term, the spectrum will show different branches with a distinct slope. The device geometry determines the occurrence of 1-, 2- or 3-dimensional *diffusion noise*. Irrespective of geometry, a spectral dependence $\propto 1/f^{3/2}$ is observed in the branch at the highest frequencies.
Another noise source which is found in virtually all physical systems is $1/f^{\alpha}$ noise, where α is close to unity and may depend on temperature and/or frequency. When the $1/f$ noise is inversely proportional to the number of carriers, Hooge's law is satisfied [20]. The analysis is then limited to the determination of the empirical, so-called Hooge parameter. Occasionally, the noise can be attributed to a superposition of Lorentzian noise sources that have a sufficiently broad range of characteristic time constants [18]. This approach was shown to work for a number of metal-oxide films [18, 21], but the model inherently fails to predict the absolute noise intensity.

1.3 Noise measurements on amorphous silicon

In the following, low-frequency noise measurements on hydrogenated amorphous silicon performed up to now are reviewed. The low-frequency range of the measurements refers to a typical range from 1 Hz to 10 kHz. The

measurements are classified according to the device geometry and doping. Finally, some attention is paid to degradation studies.

1.3.1 $1/f$ noise in coplanar structures of doped *a*-Si:H

Many contributions to the examination of $1/f$ noise in amorphous silicon are from Kakalios' group (University of Minnesota, USA). In a number of publications a connection between correlated or non-Gaussian $1/f$ noise and long-range disorder was established [22], but recent experiments have raised some doubt about that interpretation [23, 24], and are discussed later in this section. Noise measurements in *n*-type doped *a*-Si:H devices in coplanar geometry reveal $1/f$ noise and 'noise in the noise' close to $1/f$. The measured correlation between noise in different parts of the spectrum was attributed to the spontaneous fluctuations of *current filaments* which in turn affect the conduction of neighboring filaments. The choice for a coplanar geometry forces the current through a relatively long path, connecting local minima of the potential landscape. Random resistor lattice simulations predict the presence of current filaments near the percolation threshold [22, 25]. The activation energies measured from thermopower and conduction are different [22, 23], which was ascribed to the influence of long-range disorder on the electronic transport states (see also Ref. [26]).
In several studies the material composition was varied or alternatively the material was degraded by illumination, and the effect on the noise spectra examined. Fan and Kakalios measured an *increase* in the Gaussian behavior of the $1/f$ noise upon light soaking of an *n*-type *a*-Si:H film [27]. According to the authors, that could point to weaker correlation between filaments in the presence of a higher defect density. In contrast, Quicker, West, and Kakalios found *no change* in the non-Gaussian statistics after degradation of two *n*-type films, a compensated film and a sulfur-doped film [28]. Later, this was confirmed by measurements of Belich and Kakalios on (degraded) *n*-type devices prepared under various deposition conditions [23]. In addition, those devices exhibited *no change* in activation energy E_Q, which was independently determined from thermopower and conduction measurements and was proposed as a measure for the long-range potential landscape.
In an ultimate attempt to probe the correlation of the noise a recent experiment was performed on an *a*-Si:H film with 'crystalline' silicon small particles of $\sim$ 150 nm in diameter [24]. The size of these particles was so small that they contained just one filament on average (the estimated filament-

diameter was 1 μm). If interactions between filaments would be the primary cause of the noise statistics then one would expect the statistics in the nano-particles to be Gaussian. Therefore, a mixture of Gaussian and non-Gaussian components was expected in the film. However, the noise statistics of coplanar devices with or without nano-particles turned out to be identical! That, together with the absence of an increase in the Gaussian statistics after degradation [23, 24], puts the original explanation of Fan and Kakalios in serious doubt. Belich and Kakalios conclude that the noise studied in Kakalios' group might have been not as universal as was previously claimed [23, 24]. Belich and Kakalios suggest that very few noisy filaments or other fluctuators may dominate the noise and mask contributions from (changes in) the bulk material. That might also explain why the noise intensity diverges at the percolation threshold. In a comparable situation for an system with uncorrelated noise, the noise would vanish at zero bias current. Instead, the observed noise varies from device to device, due to the strong sensitivity to local filaments. The conclusion applies also to the early work of Parman and Kakalios [29], reviewed by Verleg [30], and further to Parman's later work [31].

1.3.2 1/f^α noise in coplanar structures

A Canadian research group, consisting of Günes, Johanson and Kasap, has studied noise in undoped and doped thin films of *a*-Si:H and of *a*-SiGe:H alloys in coplanar geometry [32, 33, 34, 35, 36]. The films exhibit Gaussian statistics, in contrast to the non-Gaussian statistics found in the films of Kakalios' group. In order to reach a sufficiently low film resistance, noise measurements were performed mainly in the temperature range 450 K to 500 K. Unintensionally, significant structural changes must have been induced since the temperature was above the thermal annealing of *a*-Si:H (420 K) [4]. Hydrogen movement plays a crucial role in that process. It is very likely that mobile hydrogen diffuses through the network at the temperatures of the experiment. Even out-diffusion of hydrogen is known to occur [37].
The observed $1/f$ noise exhibits a quadratic dependence on bias current. The noise spectra show two branches each fitting to a $1/f^\alpha$ power law but with different slopes α and different temperature dependences. In the low-frequency range and for undoped films, $\alpha \approx 1.2$. Further, the noise intensity is independent of temperature, but α increases slightly with temperature. In the high-frequency range, $\alpha \approx 0.6$ and temperature independent, but the

noise intensity decreases rapidly with temperature. Günes *et al.* distinguish two different noise mechanisms based on the difference in temperature dependence of the two branches [32]. However, they do not propose a microscopic mechanism to explain the observations in the two regions. Their measurements were followed by the investigation of the influence of the Ge content in *a*-SiGe:H on the noise spectra [35, 36]. Further, in *p*-type *a*-Si:H films, the slope parameter α increases with temperature from near unity to over 1.4, for temperatures from 295 K to 473 K [33], while marked deviations from a strict power law are observed. A degradation study of *n*-type *a*-Si:H films revealed a decrease of the parameter α from 1.1 to 0.8 upon degradation. The exact mechanisms underlying this multitude of effects are not clarified so far.

1.3.3 $1/f^{\alpha}$ noise in sandwich structures of undoped *a*-Si:H

The first paper on noise measurements on non-hydrogenated undoped *a*-Si dates back from 1985 [38], was performed in a sandwich configuration, and reports on $1/f^{\alpha}$ noise with $\alpha \approx 1.16$ at room temperature. A second paper, by Baciocchi *et al.*, describes measurements on hydrogenated amorphous silicon [39]. Both thin films (0.2 - 0.5 μm) were sandwiched between Cr contacts. The $1/f^{\alpha}$ excess noise spectra exhibit a frequency dependent slope α. The noise intensity level and its quadratic dependence on the voltage over the device points to resistance fluctuations. These features and the spectral shape turn out to be similar to the observations in sandwich structures carried out later in our group.
The first publication on *nin* (sometimes denoted *n-i-n*, referring to electron doped-intrinsic-electron doped layers) *a*-Si:H devices with a 2-μm-thick intrinsic layer and Cr contacts appeared in 1987 from the hands of Bathaei and Anderson [40]. The noise was found to exhibit a $1/f^{\alpha}$ dependence with $0.7 < \alpha < 1.1$. The authors explicitly reported an increasing spectral slope with frequency. The slope in the high-frequency range ($\sim$1 kHz) increases with temperature. From the temperature dependence of the conductivity and the noise intensity at 1 kHz, the activation energies were found to be 0.91 eV and 1.10-1.17 eV, respectively.
The work of Verleg and Dijkhuis on 1.5-μm-thick [1] *nin a*-Si:H films confirmed the frequency dependence of the slope of $1/f^{\alpha}$ noise spectra: $0.6 < \alpha < 1.4$ [41, 42], measured in a broader frequency domain, from 1 Hz to

[1] We re-determined the device thickness using a DekTak step profiler.

100 kHz. An example of a noise spectrum, measured in comparable conditions and reproducing the result of Verleg, is presented in Fig. 1.2. The

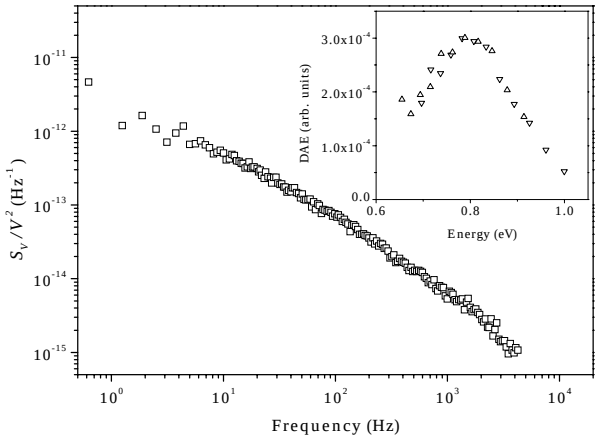

FIGURE 1.2: Relative voltage noise intensity of a 1-μm-thick *nin a*-Si:H device, *B1*, measured at 50-mV bias voltage (in Ohmic conditions), at 402 K. The inset shows the effective distribution of activation energies (DAE) responsible for the (curvature of) noise spectra at various temperatures, calculated from Dutta-Dimon-Horn analysis [18]. The energy scale was derived from the temperature dependence of the characteristic frequency, while the analysis was carried out using data at 10 Hz ($\bigtriangledown$) and at 100 Hz ($\bigtriangleup$). For details of device *B1*, refer to Table 2.1.

measured noise exhibits Gaussian statistics, indicative of uncorrelated noise and a V^2-dependence on the bias voltage in the Ohmic regime. In addition, the slope at a fixed frequency (10 Hz) was found to decrease with temperature. The activation energies of the conduction and the apparent characteristic noise frequency were found to be 0.73 eV and 0.83 eV, respectively [41]. The *corner frequency* f_1 in the noise is defined as the frequency where the spectral shape is exactly $1/f$. What it measures can unfortunately not be compared directly with the temperature dependence of the noise intensity at *fixed frequency* found by Bathaei and Anderson. Nevertheless, the general observation of a larger activation energy of noise compared to conduction is likely to be the clue to the explanation for the noise in sandwich structures of *a*-Si:H.

The noise spectra could be successfully analyzed using the phenomeno-

logical Dutta-Dimon-Horn approach [18, 21], owing to the the thermally activated behavior of the noise in sandwich *a*-Si:H devices [41]. The approach assumes the presence of a distribution of energy barriers, and considers thermally activated transitions between various two-level systems. The effective distribution of activation energies $D(E_a)$ takes the occupation numbers of all energy levels into account. For a proper analysis, $D(E_a)$ is required to vary slowly on the scale of k_BT. Then, the effective distribution follows from the noise spectrum, using

$$S_V(\omega, T) \propto \frac{k_BT}{\omega} D(E_a), \tag{1.3}$$

where $E_a = -k_BT\ln(\omega/\omega_0)$, and ω_0 is to be determined from the temperature dependence of the characteristic frequency f_1. Clearly, an exact $1/f$ spectrum corresponds to a constant $D(E_a)$. However, in case of a slowly varying effective distribution, the resulting noise spectrum will be $1/f^\alpha$, with α close to unity. Finally, we note that the proportionality sign in Eq. (1.3) indicates that the DDH-approach does not quantitatively predict the noise intensity level.

Verleg and Dijkhuis concluded that the frequency and temperature dependence of the voltage noise spectra can be traced back to originate from a single distribution of the barriers governing the thermally activated processes [41]. We carried out the analysis on a new device and qualitatively reproduced the distribution of activation energies (see inset of Fig. 1.2). The original explanation for the observed noise spectra and barrier distribution was given in terms of generation-recombination noise processes taking place at deep traps. The experimental and analytical work of Reynolds [43] and Main [44] also considers generation-recombination noise as the explanation for the observations.

Importantly, two other groups have experimentally studied $1/f$ noise in undoped *nin a*-Si:H devices inspired by the publication of Verleg's work. Recent results were reported by Kasap *et al.*, who found a slope parameter $\alpha = 0.96$ in a sandwich device at T = 375 K. In a small frequency range, they do not observe a significant change of the spectral slope, despite the significant degree of band bending in the studied device [45]. The measured noise intensity, however, is of the same order of magnitude as for our devices.

Again, inspired by the work at Utrecht University, Goennenwein *et al.* combined noise spectroscopy and electron paramagnetic resonance (EPR) to study *nin a*-Si:H devices. For a continuously illuminated device, application of a magnetic field leads to resonant changes in the electronic noise of semi-

conductors, predominantly at the central time constant $1/f_1$. That allows for the direct identification of a defect state dominating noise under non-equilibrium conditions. Hole hopping in the valence band tail is identified as the dominant spin-dependent step governing the noise under illumination conditions, when the number of holes is comparable to the number of electrons.

1.4 Aim and outline of this thesis

The aim of this thesis is to obtain a quantitative description of observed $1/f$ noise in *a*-Si:H films and of noise in *a*-Si:H thin-film transistors. We will show that noise spectroscopy is a new tool to obtain information on the structural electronic changes in the material. To reach our goals, a thorough analysis of the conductivity data is needed and performed in Chapter 2, from which all relevant device parameters are deduced. The value for the device parameters are used as input for a the *quantitative analysis* of the noise measurements. Our goal is to predict both the intensity and the shape of the noise spectrum.
In Chapter 3, a quantitative generation-recombination theory for one-dimensional devices is applied to our device using the material- and device parameters. The existing theory is extended to a system with a large number of defect states within the band gap. Our research contributes to the unresolved question whether g-r noise can produce $1/f$ noise.
In Chapter 4, a first-principle approach is presented to describe long-range potential fluctuations in *nin a*-Si:H devices. Local fluctuations of the Coulomb potential due to charged defects lead to voltage fluctuations via the screening by surrounding defects and by the contacts. The theory is capable to quantitatively predict both the noise intensity and the spectral shape, measured at different temperatures, and provides new insight in the distribution of barriers above the conduction band edge due to the random location of charged defects. Experimental data obtained from *p*-type doped sandwich structures is presented and analyzed in Chapter 5, yielding information about the potential landscape below the valence band edge. Further, the distribution of barriers from a deuterated film is compared to the result from a hydrogenated film.
In Chapter 6 we report on the effect of prolonged illumination on the noise intensity of *a*-Si:H. Previous work left us with an apparent contradiction: while a slight increase of the noise intensity is to be expected, an increase

by a factor of 10 was observed [30]. A proper analysis turns out to explain that increase in rather trivial terms. New measurements show only a slight increase of the noise intensity, which turns out to be consistent with the theory presented in Chapter 4.
Finally, Chapter 7 deals with thin-film transistors (TFTs), which have the interesting feature that the concentration of charge carriers in the conducting channel is controllable via the gate voltage. The noise measurements are focused to the near-threshold regime, in which diffusion noise in the one-dimensional conducting channel turns out to dominate. A quantitative analysis of the noise yields the effective diffusion coefficient and the mobility in the near-threshold regime, consistent with conductivity measurements.

Chapter 2

Devices, conductivity and setup

2.1 Devices

2.1.1 Positioning of the device in the setup

The device holder is located in a vacuum chamber, which is electrically Connected to other parts of the setup. The copper holder, which is in thermal contact with a heater, has room for a removable copper block. The substrate which is glued on top of the copper block provides good thermal contact between the device and the heater. The copper holder contains a Pt100 thermocouple, allowing for temperature monitoring and stabilization by a Lakeshore temperature controller between room temperature and 450 K. Our thin-film *a*-Si:H devices have typical dimensions 7×8 mm and are glued onto the central gold-square of a special ceramic substrate (of 27 mm^2) using a conducting silver epoxy, EPOTEK P1011. A hardening step is required of 1 hour, during which the entire substrate is kept at 150 °C. A copper or aluminum wire is electrically connected between the top contact and a gold pad on the substrate (see Fig. 2.1).

2.1.2 Contact requirements

Low-ohmic electrical contacts with top- and bottom layers are required for our electrical measurements. To reduce oxidation, we need noble metal as contact material. Unfortunately, sputter deposition of gold is impossible. We decided to use copper instead, and to insert titanium as a barrier to prevent copper ions from diffusing into the material at high temperatures and causing contamination of the semiconductor. In some cases, a metal oxide

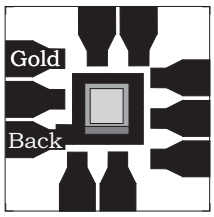

FIGURE 2.1: Ceramic device substrate and its golden contact pads plotted to scale. Back contact pad is indicated. Top-contact of the device, is glued on the central pad, and connected to a gold pad via a copper wire or an aluminum bond.

forms between the contact and the semiconductor film, signified by a strong $1/f$ noise and a relatively large device resistance in the high (400 K) temperature range, preventing usefull noise measurements.

2.1.3 Device structure

For our noise measurements, we use amorphous silicon devices with a doped-intrinsic-doped sandwich structure, either *nin* or *pip*. To avoid direct contact between the back metal layers and amorphous silicon layers, we did not use a glass substrate but a low-resistivity (1-3 Ωcm) n^{++} doped *c*-Si wafer (see Fig. 2.2). In case of the *pip* devices a p^{++} wafer was used, instead. The current runs through the sandwich structure to the wafer, metal layers, silver epoxy, and the central gold-pad (see Fig. 2.2). The contact materials were sputtered in the same run using a mask, which leaves a square of 5×6 mm uncovered for metal deposition (the lightly shaded part in Fig 2.1). Sputtering was performed under UHV conditions in a clean-room environment. The native oxide between the wafer and the amorphous silicon film is roughly one monolayer thick [46], thin enough to ensure that electrons can tunnel easily through it and do not contribute to the noise. The estimated resistance of the 500 μm n^{++} *c*-Si wafer is 1 mΩ.

2.1.4 Device preparation

Prior to deposition the wafer was cleaned in a 66% HNO_3 solution for 10 minutes, followed by a HF dip during 2 minutes, and finally a water dip.

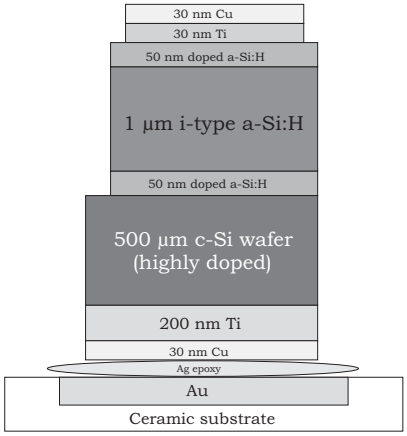

FIGURE 2.2: Cross section of the layered device (not to scale). Indicated thicknesses are standard values, from which actual deposition data might deviate (see Table 2.1).

Hydrogenated amorphous silicon is deposited in the Utrecht Solar Energy Lab. (USEL) on a wafer by dissociation of silane gas (SiH_4). All devices reported in this study where grown by Plasma Enhanced Chemical Vapor Deposition (PECVD). This deposition technique is based on the enhancement of gas dissociation into various radical species by electrons in a plasma. The applied RF field was set to a frequency of 13.56 MHz, while the substrate temperature was stabilized at 468 K. Under these conditions the growth rate is 0.20 nm/s. Additional gases can be admitted in the reactor to passivate and to grow doped layers: hydrogen (H_2) for passivation, phosphine (PH_3) for *n*-type, and tri-methylborane (TMB) for *p*-type layers. Application of a relatively high RF power (10 W instead of 3 W for amorphous *n*-layers) made the *p*-type layers microcrystalline, which gives the best possible layers. The energy barrier height between the *p*-type layer and the metal contact is estimated to be as small as 0.06 eV [47], approximately $2k_BT$ at room temperature. The intrinsic layer of deuterated amorphous silicon devices was deposited using SiD_4. Each intrinsic layer was exposed to air before and after deposition of the intrinsic layer. Another air exposure was needed prior to sputter deposition of the metal layers. Despite some unavoidable oxidation of the surfaces we could detect no signs of contact noise.
The devices used in this thesis are specified in Tab. 2.1. To each batch is

assigned a character, while numbers indicate different samples of the same batch. The *nin* devices were made in batch *A*, *B* and batch *D*, the latter with deuterium (D) in the intrinsic layer. In batch *C pip* devices were deposited. For comparisson, the conditions for the *nin* devices of Verleg are included as batch *V*.

The procedure for the measurement of the device thickness makes use of

device	structure	*n* layer (nm)	*i* layer (μm)	area (cm^2)
A	*nin*	55	1.1	0.55
B1	*nin*	40	0.91	0.55
B2	*nin*	40	0.91	0.64
B3	*nin*	40	0.91	0.11
C	*pip*	28 (*p*)	0.84	0.57
D1	*nin* (D)	55	1.12	0.57
D2	*nin* (D)	55	1.12	0.55
D3	*nin* (D)	55	1.12	0.56
V	*nin*	50	1.50	0.56

TABLE 2.1: Area and thickness of the devices.

the fact that the substrate is contained in a strip mask. The strips are thin metallic ribbons, 1-mm wide, that cover the substrate partially. Deposition of amorphous silicon creates a vertical step along the edges of the mask. This step is indicated in the cross section of the *a*-Si:H structure shown in Fig 2.2. A Dektak step profiler was used to determine the height of this vertical step, which equals the total thickness of all amorphous silicon layers. Since batch *A* was deposited without such a step, its thickness was estimated from the growth rate and deposition time.

2.1.5 Device properties

In case of batch *C*, the holes are the majority carriers and the conductivity σ equals $pe\mu_p$, with μ_p the hole mobility. ¿From the measured J-V characteristics in the Ohmic regime, the conductivity prefactor σ_0 was determined at $(7 \pm 1)\cdot 10^3\ \Omega^{-1}\mathrm{m}^{-1}$. In case of batch *B*, the electrons are the majority carriers and the conductivity σ is given by $ne\mu_n$, with μ_n the electron mobility. The measured conductivity prefactor σ_0 is found to be a factor of three larger compared to *pip a*-Si:H devices. The unavoidable difference in thickness between the devices *C* and *B1* has influence on the conductivity prefactor and

therefore prevents a direct determination of the ratio μ_n/μ_p. Assuming that $N_V = N_C$, we estimate for intrinsic PECVD *a*-Si:H material grown at 468 K that $\mu_n \approx 3\mu_p$.
The *nin* device with hydrogen (*B1*) has a 35-% higher conductivity than the device with deuterium (*D1*), while the deuterium device is 23% thicker, due to a different growth rate than anticipated. As a result, the dilution with deuterium during the deposition process might have been larger.

2.2 Device simulations

2.2.1 Simulation program

To analyze time-dependent fluctuations, the steady-state electrical properties have to be known to sufficient precision. Some can be found in literature, others have to be determined from experiments on a device from a specific batch, since material properties may vary from batch to batch. For example, the activation energy of the conduction is determined from the measured temperature dependence of the J-V characteristics in the linear regime, where J is the current density and V the voltage. The idea developed in this thesis is to use a computer simulation program to extract defect parameters relevant for our noise measurements, by adjusting the parameters to the non-linear part of the J-V curve. This procedure is called inverse fitting.
A variety of computer programs is available to compute the steady-state electrical properties in layered semiconductor films by solving the Poisson equation and the continuity equations for electrons and holes. Input parameters are mobility, defect concentrations, etc. We used the Windows version of AMPS-1D [48], in which deep defects are modeled using two Gaussian distributions while the tail states are approximated by exponential distributions. Further details are given below.
We checked that other, even more advanced programs, based on the so-called Defect Pool Model [13] produce qualitatively the same band diagram as AMPS-1D. The comparison was made with results obtained from an extended version of AMPS-1D, D-AMPS-1D [49] and ASA [50]. The quantitative difference in the results obtained out of these more computer-time-consuming models turned out to be negligible for our purposes.
Amphoteric defects deep in the gap play an important role in amorphous silicon and have the ability of capturing zero, one or two electrons, and consequently have three charge states called D^+, D^0, and D^-, respectively. An

amphoteric defect in the D^0 state can either capture or emit an electron. The model description of defects is limited to only two kinds of transitions. Capture corresponds to acceptor levels, and emission to donor levels in that model. A typical donor transition is $D^- \rightarrow D^0 + e$. Defect states are assumed to be distributed in energy according to a Gaussian profile. Donor and acceptor states are separated by the correlation energy U. For example, in the typical acceptor transition $D^0 + e \rightarrow D^-$, the additional energy needed to put a second electron on the defect equals U.
The one-dimensional device simulation program AMPS-1D [48] computes a set of electron and hole concentrations and potential as a function of position that is consistent with the measured *J-V* curve for all given combinations of temperatures, bias voltages, and even illumination intensities. Details of the AMPS-program are available on the AMPS-web site (see Ref. [48]) and in Chapter 2 of Van Veghel's masters thesis [51]. The transitions between defect levels and carrier bands are described using the Shockley-Read-Hall model (see section 3.2.2).

2.2.2 Simulation of J-V curves

In order to reduce the number of free parameters in our model, we use estimates from literature. Using the measured activation energy of an *n*-type layer of PECVD *a*-Si:H [52], we find the same activation energy in the calculated band diagram for a donor density of $3.3 \cdot 10^{17}$ cm^{-3}. In order to mimic the smooth connection between the *n*-layer and the contact, we fixed the contact potential ϕ to 0.20 eV.
Capture cross-sections were set to $1 \cdot 10^{-15}$cm^2. The tail states were modeled by an exponential energy distribution below the band edges, with a decay factor of 0.03 eV for the conduction band and 0.045 eV for the valence band, respectively. The electron mobility μ_n was fixed to 10 cm^{2}V^{-1}s^{-1} [1].
The fitting procedure was performed in two steps in which we adjusted to the linear and the non-linear part of the J-V curve, respectively. ¿From the fit to the *linear part* of the J-V curve at three temperatures we obtain: density of states at the conduction band edge $N_C(E_C)$ and the band gap. The former is obtained via the temperature-independent prefactor of the conductivity $\mu_n N_C(E_C)$, and the latter from the activation energy of conduction that characterizes the interaction between the band gap E_g and the defect levels, with central positions E_0 and E_0', representing the $D^+ \leftrightarrow D^0$ transitions and the $D^0 \leftrightarrow D^-$ transitions, respectively. With a fixed band gap, we subsequently fitted to the *non-linear part* of the *J-V* curve in order to extract

the defect density n_D, the central positions of the D^+/D^0 level E_0, and the D^0/D^- level E_0' with respect to the valence band edge E_V, and the width $2\Delta E$ of the Gaussian energy distribution of these defect levels. These defect parameters turn out to be important parameters for computing the absolute noise intensities in our device.
The central positions of the Gaussian defect distributions E_0 and E_0' influence the location of the Fermi level, and therefore are adjusted until the temperature dependence of the linear part of the data fits well. It turns out that the sensitivity of the non-linear part to the width ΔE is rather small. In our approach, we can determine the above mentioned defect parameters including n_D within 10 % by a fitting procedure which requires only a few data points.
A typical example of our fit is plotted in Fig. 2.3, and shows the excellent agreement between simulation and experiment. The fitted parameters are

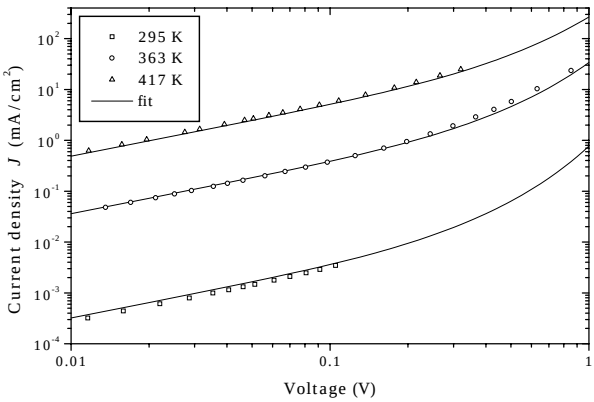

FIGURE 2.3: $J - V$ characteristics of *nin a*-Si:H device *B1* at three temperatures, including the result of fitting according to parameter set (1).

listed in Table 2.2. Since the number of fitting parameters is large, some ambiguity of the fitting parameters exists. To indicate the range in the fitted values in case of device *B1*, parameter set (1), parameter set (2), both leading to acceptable fits, are included. For the thin devices of batch *B*, equally well fits can be obtained with a defect density that ranges from 4 to 8 $\cdot 10^{15}$ cm^{-3}, while for the thicker devices that range is narrower. The first lines of the table show the two measured (not adjusted) quantities: the activation

energy of conduction E_σ and the thickness of the intrinsic layer.

Measured parameters	*A*	*B1* (1)	*B1* (2)
Activation energy E_σ	0.68 eV	0.63 eV	0.63 eV
Thickness *i*-layer	1.1 μm	0.91 μm	0.91 μm
Adjustable parameters			
$N_C(E_C)$	$3.4{\cdot}10^{20}$cm^{-3}	$2.0{\cdot}10^{20}$cm^{-3}	$3.35{\cdot}10^{20}$cm^{-3}
Defect density n_D	$2.5{\cdot}10^{15}$ cm^{-3}	$6.0{\cdot}10^{15}$ cm^{-3}	$4.6{\cdot}10^{15}$ cm^{-3}
Bandgap E_g	1.82 eV	1.80 eV	1.80 eV
D^+/D^0 level $E_0 - E_V$	0.78 eV	0.95 eV	0.89 eV
D^0/D^- level $E_0' - E_V$	1.12 eV	1.15 eV	1.09 eV
Resulting parameters			
E_{C0}-μ	n.a.	0.63 eV	0.71 eV
E_{B0}-E_{C0}	n.a.	0.27 eV	0.19 eV

TABLE 2.2: Device parameters, obtained from direct measurement or fitting with AMPS. Fixed parameters: mobility μ_n = 10 cm^{2}V^{-1}s^{-1}, contact potential ϕ = 0.20 eV, correlation energy U = 0.20 eV and the halfwidth ΔE of the defect distributions = 0.15 eV. The energy levels E_{C0} and E_{B0} indicate the conduction band edge and the average barrier height (see section 4.3), respectively.

2.2.3 Band bending

A typical band diagram (for thin devices) consistent with all J-V measurements is plotted in Fig 2.4. The coordinate x is perpendicular to the film. The variable x_T is the characteristic length of the uniform resistivity layer, which will be introduced in section 2.2.4. Further, the location and thickness of the n^{++}-doped layers and the intrinsic layer are indicated. The diagram shows the conduction band profile $E_C(x)$ and the chemical potential μ. Zero energy is chosen at the valence band edge E_V in the doped layers. The doping induces a high electron concentration in the intrinsic layer, because of the requirement of continuity of the potential at the boundaries. As a result, the conduction band bends in the interface region. Since the device thickness is only ≈ 1 μm, and the defect density is low, interface effects persist through the entire device. This leads to the strong band bending indicated in Fig. 2.4. Thermally activated processes therefore depend strongly on the

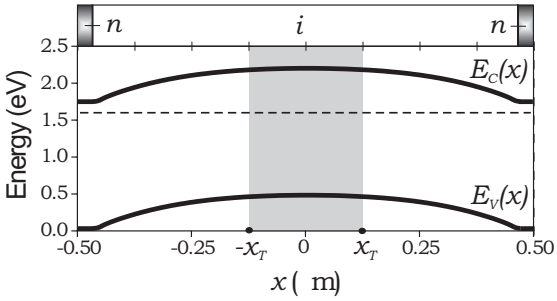

FIGURE 2.4: Band diagram of *a*-Si:H device *B1*, indicating conduction and valence band levels E_C and E_V *vs* position x in μm. The *nin* geometry is illustrated at the top. The shaded region corresponds to the "uniform resistivity layer".

position in the device. Another consequence of n^{++} doping is that electrons are the majority carriers and that the entire device contains only one hole (from device simulations).
The total device resistance can be viewed as a series sum of local resistances. These are inversely proportional to the local electron concentrations $n(x)$ per unit length and are exponentially dependent on the local energy difference $E_C(x) - \mu$. A consistency check of the AMPS calculations was performed by integration of $1/n(x)$ over position, which indeed yielded the measured resistance. The central part of the device limits the conductance, due to the low electron concentration and the high local activation energies: the activation energy of the conduction is only slightly smaller than the maximum energy difference in the center. As a result, the external voltage predominantly drops over the central region of the device.

2.2.4 Uniform resistivity layer

For future convenience, we approximate our thin film as a uniform resistance layer which mimics the resistance and can be used to calculate the resistance noise. From the band diagram, one observes that the conduction band $E_C(x)$ can be taken as parabolic around the center of the film and written as

$$E_C(x) = E_{C0} - \beta x^2. \tag{2.1}$$

The central activation energy of the conduction is $E_C(0)-\mu$, where μ is again the chemical potential. The values of the parabolic parameter β are listed in table 2.3, increase with decreasing thickness and have a relative error of 5%. For the *pip* device *C* a parabolic fit was, of course, fitted to $E_V(x)$. Using the

Device	d_i (μm)	β (eV/μm^2)	n_D (cm^{-3})
A	1.45	1.26	2.5·10^{15}
B1	0.91	1.59	6.0·10^{15}
C	0.84	1.54	6.0·10^{15}
D1	1.12	1.24	4.0·10^{15}

TABLE 2.3: Band bending parameter and defect density of best AMPS fits to J-V curves of various devices.

device simulation program AMPS for *pip* device *C* we obtain for the defect density n_D = 6·10^{15} cm^{-3}eV^{-1} and the central position of the Gaussian distribution of defects E_0 = 0.03 eV below to the Fermi level μ. The activation energy $\mu - E_{V0}$ in the center of the device appears to be 0.03 eV above the measured value of conductivity, as expected. The band bending of the valence band can again be described by a parabolic coefficient β (just as for the conduction band in Eq. (2.1)) and amounts to 1.54 eV/μm^2.
We now will define a layer of uniform resistance. The local resistivity $\rho(x)$ is inversely proportional to the local density of free electrons $n(x)$, which is thermally activated. Therefore we may write

$$\rho(x) = \chi/n(x) = \chi' \exp\Big(\frac{E_C(x)-\mu}{k_B T}\Big), \tag{2.2}$$

where χ and χ' are proportionality constants, k_B is Boltzmann's constant, and T the temperature. The resistivity is strongly peaked around $x = 0$. In the parabolic approximation, the total resistance R_0 of the device is

$$R_0 = \frac{1}{A}\int \rho(x)dx \approx \frac{\rho(0)}{A}\sqrt{\frac{\pi k_B T}{\beta}}, \tag{2.3}$$

where *A* is the device area. We assign to the layer a constant resistivity $\rho_0 = \rho(0)$ and adjust the thickness, $2x_T$. To arrive at the same resistance R_0, we find $x_T = \frac{1}{2}\sqrt{\frac{\pi k_B T}{\beta}}$. The thickness of the layer of uniform resistivity ($2x_T$) is obviously temperature dependent and indicated by the shaded region in the band diagram. A typical value of x_T is 0.13 μm, i.e. conveniently within the region of the device, where the parabolic approximation is valid.

2.3 Setup

The experimental setup used for the noise measurements is schematically shown in Fig. 2.5. The device (indicated by *nin*) was mounted in a vacuum chamber equipped with an optical window. The device (of resistance R) is connected in series with a resistance R_{series}, which is chosen to be at least 20 times higher. As a result, the current I supplied by the voltage source V_B is virtually constant. Spurious noise contributions from the voltage source, a dry battery, if present at all, is further reduced by an RC filter circuit connected to the source (not shown). The voltage fluctuations δV are amplified by a low-voltage noise amplifier (NF Electronics LI 75A). The Advantest R9211A digital spectrum analyzer determines the autocorrelation function $\langle \delta V(t) \delta V(0) \rangle$ and computes the Fast Fourier Transform (FFT) in a frequency bandwidth from 250 mHz to 100 kHz. Special care is taken in shielding and grounding of the setup to eliminate RF pick-up. A voltage noise measure-

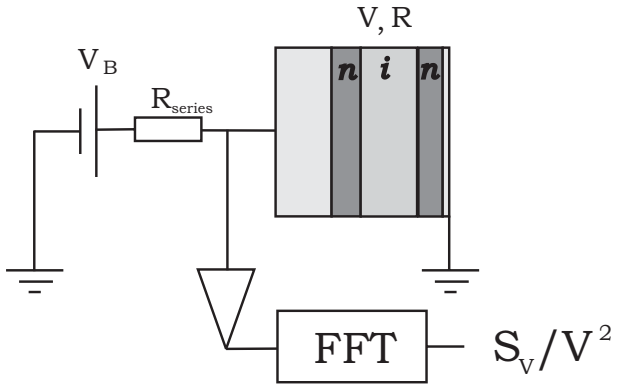

FIGURE 2.5: Schematic diagram of the experimental setup for noise measurements, with a device resistance R and series resistance R_{series}.

ment under voltage-biased conditions has to deal with at least three noise contributions: thermal noise, amplifier noise, and the noise signal which we wish to measure: the voltage-dependent resistance fluctuation. In absence of bias voltage (and thus of current) a background noise spectrum is measured, consisting of thermal noise and amplifier noise. The background spectra are subtracted from the spectra taken under voltage bias to obtain the resistance noise. Finally, the spectra are gauged using a calibrated white noise source (Quan-Tech 420) in series with the device. The measurements

were repeated several hundreds of times to obtain a lower error of the spectra (about 3 % for averaging over 300 individual spectra).
An optical window allowed us to *in-situ* degrade the sample with a halide lamp. Details of the conditions during degradation will be given in Chapter 6. After deposition, the device was annealed at 450 K during 8 hours and slowly cooled to room temperature. The measurements at elevated temperatures were invariably carried out from room temperature upwards.

Chapter 3

Study of g-r noise

3.1 Introduction

The experimental and analytical work described in Verleg's thesis [30] on the electrical noise in *a*-Si:H devices strongly suggested generation-recombination (g-r) noise as the main source. According to the definition of Van Vliet [17], g-r noise originates from individual capture and emission processes of charge carriers to and from the conduction band or valence band in a semiconductor. Possible transitions often involve traps in the forbidden band, but may also be direct (band-to-band). Numerical evaluation of g-r noise spectral intensities is feasible using theories in literature but has never been actually applied to check if it can quantitatively explain the noise in amorphous silicon.
Therefore, we decided to use g-r noise theory described in a recent paper by Van Vliet [53], to compute quantitatively the g-r noise in our inhomogeneous multi-level device. From device simulations we already know that the conductivity and all other time-averaged electrical properties of our device can be consistently described by a multi-defect level system and position-dependent occupations (see section 2.2). In Fig. 3.1 the relevant carrier trapping and emission processes are indicated by arrows in a schematic band diagram. Here, the conduction band E_C and the valence band E_V are taken independent of position, implying that the chemical potential μ varies with position given the band bending. The trap levels E_i located within $\pm\, 2k_BT$ around the chemical potential dominate the fluctuations δn_0 in the free electron density, since electrons obey Fermi-Dirac statistics. The local density fluctuations (indicated in the box at position $x = x_0$) are measured at the

contacts as voltage fluctuations δV. The full derivation for g-r noise in such

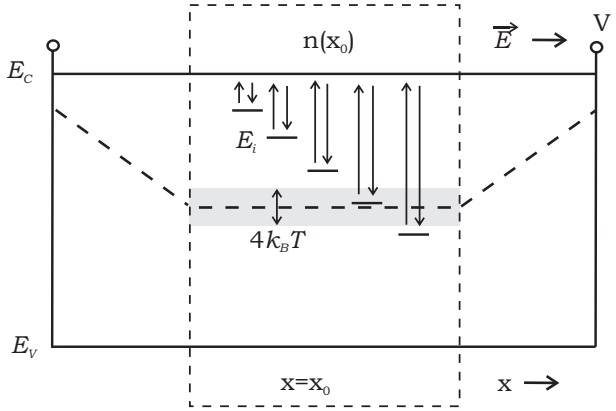

FIGURE 3.1: Diagram of local g-r noise processes, resulting in density fluctuations δn_0, which are measured as voltage fluctuations δV at the contacts.

a system was described by Van Vliet and Fassett in 1965 [17] and is also found in a review paper by Van Vliet, Ref. [54]. We will review the course of the calculation and highlight the essential elements very briefly. In section 3.3 the results of our computations are reported. The devices in our study are assumed to have only one type of carrier, the majority carrier, i.e. electrons in case of *nin* devices. In that case, the hole contribution to the electrical conduction can be neglected and the valence band does not need to be considered in our model. Only fluctuations in the number of *free electrons* will cause significant resistance fluctuations. Since all defect levels are allowed to communicate with the conduction band level and the total number of electrons is constant, the number of free electrons at the conduction band level may be eliminated as a parameter without loss of information. Thus the number fluctuations can be expressed in terms of fluctuations of the defect levels, and become accessible for measurement as voltage fluctuations at the contacts. The problem can be taken to be one-dimensional because of the sandwich geometry of our device and the negligible in-plane diffusion current (see section 2.2). The electron distribution and the electric field were taken from the simulations that simultaneously fit all time-averaged electrical characteristics of our device (these will be used in section 3.3). Further assumptions appear to be needed to make the model tractable: absence of spatial correlation in the noise, no direct transitions between the defect lev-

els, and absence of hopping of electrons between neighboring defects. Spatial correlation only exists on length scales of the order of the localization length of an electron, which is less than one nanometer (see estimate in section 4.4). In our calculation, the spatial separation between the subsequent layers is taken larger, because the result turns out to be independent of the separation width. The principle of local detailed balance between capture and emission events is used. Stochastic processes are assumed to be stationary.

3.2 Ingredients of g-r noise theory

We start by introducing the voltage noise intensity S_V in its most general form and then derive a more practical form. The Wiener-Khintchine theorem [15] (Eq. (4.2)) connects the spectral noise intensity to the Fourier transform of the autocorrelation function of the measured time dependent voltage signal $V(t)$, and contains the Fourier transform of the voltage signal $\tilde{V}(\omega)$ and its complex conjugated form $\tilde{V}^*(\omega)$, with ω is the angular frequency,

$$S_V(\omega) = 2\left\langle \tilde{V}(\omega)\tilde{V}^*(\omega)\right\rangle. \tag{3.1}$$

Van Vliet has derived a general expression for the g-r spectral noise intensity in case of a one-dimensional multilevel inhomogeneous device [53],

$$S_V(\omega) = 2\sum_{i,k,l}^{s-1}\int_0^L dx\, W_g(x)[M_{ik}(x)+i\omega\delta_{ik}]^{-1}B_{ii}(x)[M_{li}(x)-i\omega\delta_{li}]^{-1}. \tag{3.2}$$

This complicated expression will be explained in the following sections. The qualitative meaning of the terms in Eq. (3.2) is, however, quite straightforward. The *intensity* of g-r noise is governed by the term B_{ii}, which equals the total number of transitions to and from a level i per unit time and per unit length. The transition rates can be specified, and concequently be summed over all defect levels. The *spectral shape* of g-r noise is contained in the terms M_{ik} and ω. From the general expression it is recognizable that Eq. (3.2) effectively represents a Lorentzian spectrum, with a characteristic feature: the cut-off frequency. That cut-off frequency corresponds to the average time it takes for an excess charge in the conduction band to relax and bring the system back into equilibrium. For a given measuring frequency and for each position, one can sum the Lorentzian contributions to the noise intensity from all trap levels. As a result, the intensity of number fluctuations per

unit length $S_n(\omega, x)$ yields $S_V(\omega) = \int \mathrm{d}x\, W_g(x) S_n(\omega, x)$ (c.f. Eq. (3.2)). The weight factor W_g defines the *conversion factor* of local carrier number fluctuations into voltage fluctuations measured at the contacts.

3.2.1 Relaxation

In this section the general expression for M_{ij} in terms of transition rates will be given. In section 3.2.2 that expression will be evaluated for the case of a multi-level system. As stated above, the noise relaxation time τ is defined as the time it takes for the system to be restored to the steady state after a fluctuation has taken place. In our experiments, we are sensitive to processes on the time scale of 10 μs to 1 s, because of the finite RC-time of the measuring circuit at high frequencies, the amplifier noise at low frequencies, and the spectrum analyzer used. The important question is: do significant g-r processes occur on this time scale in our system, and can they quantitatively explain the observed noise?
Let us briefly describe the framework in which the relaxation time can be discussed. The electron density at some position x is denoted n_i for each level i (including the conduction band). Deviations from the average steady state density $n_{i,0}$ of level i are denoted as Δn_i and are subject to relaxation. Conservation of charge implies that the number fluctuations in the conduction band Δn_s can be expressed as

$$\Delta n_s = -\sum_{i}^{s-1} \Delta n_i, \tag{3.3}$$

which converts the fluctuations in the various defect levels to the free carrier fluctuations. From now on, the free-electron density n_s is eliminated, and summation is up to level $s-1$. The *phenomenological relaxation matrix elements* M_{ij} govern the relaxation of excess trap densities [17]:

$$\frac{\partial \langle \Delta n_i \rangle}{\partial t} = -\sum_{j=1}^{s-1} M_{ij} \langle \Delta n_j \rangle. \tag{3.4}$$

Here the coupling between levels i and j is only indirect, via the conduction band. These are standard phenomenological rate equations. The coupling matrix elements in absence of direct transitions between the levels read:

$$M_{ij} = \left[\frac{\partial p_{is}}{\partial n_j} - \frac{\partial p_{si}}{\partial n_j} \right]_{n_i = n_{i,0}}. \tag{3.5}$$

For our specific case, M_{ij} contains all relevant conditions of the relaxation, expanded around steady state, expressed in the transition probabilities p_{is} and p_{si} per unit volume. Other details on the transition rate are given in the next section. The noise relaxation times τ_i of the system can be found by solving the eigenvalue problem of the relaxation matrix $\mathbf{M}$ [17]:

$$\det(\mathbf{M} - \frac{1}{\tau_i}\mathbf{I}) = 0. \tag{3.6}$$

We note that a system of s levels will have $s - 1$ relaxation times.

3.2.2 Multi-level model

For calculation of the g-r noise intensity the transition rates which determine B_{ii} and M_{ij} are given in this section. The continuous distribution of defect states in an amorphous semiconductor can be adequately modeled by a limited number of levels. The equations for emission and trapping processes are constructed on basis of the so-called mass-action law. For example, the transition rate p_{si} from the conduction band s to any level i is proportional to the concentration of electrons in the original level s and the concentration of available positions in the final level i

$$p_{si} = \sigma v_{th}(N_i - n_i)n_s, \tag{3.7}$$

where N_i is the defect density at level i, n_i the density of trapped electrons at level i, $N_i - n_i$ the density of available locations at level i, $n_s \equiv n$ the free-electron concentration, σ the capture cross section, and v_{th} the thermal velocity. The transition rate for emission is proportional to the particle density in level i

$$p_{is} = \alpha n_i, \tag{3.8}$$

with α a proportionality constant. Now the principle of *detailed balance* is imposed, which means $p_{si} = p_{is}$ in steady state, and yields

$$\sigma v_{th} n_0(N_i - n_{i0}) = \alpha n_{i0} \equiv \sigma v_{th}\hat{n}_i n_{i0}, \tag{3.9}$$

where n_0 and n_{i0} are equilibrium concentrations of free electrons and traps, respectively, and $\hat{n}_i$ defines the so-called Shockley-Read densities. From Fermi statistics for the trap occupancy for trap level ϵ_i

$$\frac{n_{i0}}{N_i} = \frac{1}{1 + \exp[(\epsilon_i - \mu)/k_B T]}, \tag{3.10}$$

the Shockley-Read densities can be computed

$$\hat{n}_i = n_0 \exp\left[\frac{\epsilon_i - \mu}{k_B T}\right], \tag{3.11}$$

which corresponds to the actual free electron densities, would the Fermi level coincide with the trap level. The above formulation was introduced by Shockley, Read and Hall, is e.g. described in Ref. [55], and serves to cope with the large number of empty states above the conduction band edge. Mutual transitions between localized states are neglected, thus $p_{ij} = 0$ unless i or j equals s. Now the matrix elements of g-r noise, introduced in Eq. (3.2), can be specified. The transition rates B_{ii} and relaxation times τ_i relevant for g-r noise, are based on the specific multilevel model we described. The matrix elements B_{ii} are defined as the sum of the two transition rates between level i and level s

$$B_{ii} = (p_{si} + p_{is})_0 = 2\sigma v_{th}(N_{i0} - n_{i0})n_0. \tag{3.12}$$

The transition matrix elements $B_{ij} = 0$, since the mutual transition rates between the levels p_{ij} are taken zero.
With the transition rates based on the formalism used by Shockley, Read and Hall, we are at the point to specify another ingredient of the g-r noise spectrum: the phenomenological relaxation matrix elements M_{ij}. The relaxation times τ_i are the eigenvalues of the relaxation matrix $\mathbf{M}$ defined in Eq. (3.5). Since relaxation involves the expansion of the transition rates around steady state, the determination of $\mathbf{M}$ requires the differentiation of the transition rates to the trap electron densities. The chain rule implies that $\partial/\partial n_j$ generates terms $(\partial/\partial n_0)(\partial n_0/\partial n_j) = -(\partial/\partial n_0)$, resulting in

$$\begin{aligned} M_{ii} &= \sigma v_{th}(\hat{n}_i + n_0 + N_i + n_{i0}), \\ M_{ij} &= \sigma v_{th}(N_i + n_{i0}). \end{aligned} \tag{3.13}$$

Now we will consider the effects of the transition statistics for the g-r noise spectrum. The solution of the linear first-order differential equation for the relaxation, Eq. (3.4), is an exponential decay function in time. The Fourier transform of that function enters the noise spectra, and is a Lorentzian spectrum. Therefore, a sum of Lorentzians is anticipated in the calculated noise spectrum.
Next, we will demonstrate the Lorentzian nature of the spectra. We focus on the noise intensity per unit length $S_n(\omega, x)$, defined in $S_V(\omega) = \int \mathrm{d}x\, W_g(x) S_n(\omega, x)$. Consider the case where the number of traps $N_i \ll n_0$,

the number of free electrons. (This condition is met near the edges of the device.) In that case all elements M_{ij} vanish, while the elements M_{ii} equal $1/\tau_i$ and the simple expression for the noise intensity (per unit length) yields

$$S_n(\omega, x) = 2 \sum_i \frac{B_{ii}(x)\tau_i^2(x)}{1 + \omega^2 \tau_i^2(x)}, \tag{3.14}$$

which is a sum of Lorentzian spectra [53]. Now, consider the central region of the device, where the situation is more complex. In that case the number of traps N_i is large compared to n_0 and the eigenvalues $1/\tau_i$ are not simply the M_{ii}'s. Then, the source B_{ii} is combined with two relaxation terms of the form $[M_{ik} + i\omega\delta_{ik}]^{-1}$ in the final expression Eq. (3.2). This issue is addressed in the review article of Van Vliet [54]. Yet, Eq. (3.14) helps to recognize a Lorentzian type of spectrum in Eq. (3.2). That Lorentzian form times the local source term $B_{ii}(x)$ represents the local intensity of *carrier density fluctuations* (intensity per unit length in our 1D model). The concept of carrier-density fluctuations is introduced to be able to account for the spatial variation of the electron densities. The spatially dependent matrices $\mathbf{B}(x)$ and $\mathbf{M}(x)$ are used in the matrix computations. After integration over position, the intensity of *number fluctuations* is obtained.

3.2.3 Green's function procedure

The next task is to convert the local density fluctuations into voltage fluctuations at the leads, so that the theoretical result can be directly compared to the data. The conversion is done by introducing the local weight factor W_g. It measures how fluctuations from different positions in the device will be observed at the leads. When noise is spatially uncorrelated, this factor can be separated from the local noise intensity

$$W_g(x) = \left| \int_0^L dx' \; g(x', x) \right|^2, \tag{3.15}$$

where $g(x', x)$ is the Green's function [53]. We will briefly describe the procedure introduced by Fassett [56] to determine the Green's function. The Green's function measures the response of the electric field at the leads to a local fluctuation in the carrier density. More specifically, it is the frequency-dependent solution of the transport operator $\mathcal{L}$ of the system evaluated at the contact at time t due to a single instantaneous fluctuation (at time zero) at a specific point in the device.

Transport The response depends on the precise form of the transport operator $\mathcal{L}$. In general, $\mathcal{L}$ includes drift, diffusion, and ohmic relaxation, which, in turn, are governed by device parameters like mobility, electron density etc. The amplitude of the Green's function is a measure of the voltage fluctuation to which one local charge fluctuation at position x leads at the contacts.
Next, we will define the linear differential transport operator $\mathcal{L}$ relevant for our one-dimensional inhomogeneous device. Diffusion can be neglected in current-driven space-charge limited devices at the applied voltages, since drift dominates [53]. We are left with the drift term, and the related term of ohmic relaxation. The Green's function appears to be solved most conveniently in the frequency domain. For this, we use the Laplace transformed operator $\hat{\mathcal{L}}$, which reads in our case [53]

$$\hat{\mathcal{L}} = \frac{\varepsilon\varepsilon_0}{q}\frac{\partial}{\partial x} - \frac{n_0(x)(1+i\omega\tau_\Omega)}{\mathcal{E}_0(x)}, \tag{3.16}$$

where $\varepsilon\varepsilon_0$ is the dielectric constant of the material, q the elementary charge per unit area, and $\mathcal{E}_0$ the local field strength, dominated by the internal field, and τ_Ω the Ohmic or dielectric relaxation time, defined as $\tau_\Omega = \varepsilon\varepsilon_0/q\mu n_0$, which is taken position independent for simplicity. The above transport operator is frequency-dependent, and in principle affects the frequency response of the device. However, the Ohmic relaxation time τ_Ω is of the order of μs or shorter, and therefore the imaginary part (the product $\omega\tau_\Omega$) is negligible in the frequency range of interest. For a typical *nin* device, the electric field vanishes in the center, which implies that a free electron in the centre will stay there (in absence of current). Fluctuations in the center can thus be disregarded, and therefore the integration is over the full length except the centre, which avoids singularities in the computation.
Because of the short Ohmic relaxation time, the defining equation for the Green's function becomes frequency-independent and reads [17]

$$\hat{\mathcal{L}}(\partial/\partial x)g(x', x) = \delta(x' - x). \tag{3.17}$$

Solving the Eq. (3.17) is in general quite involved due to the spatial dependence of $\mathcal{L}$. Simple cases and solutions are discussed in Ref. [17]. We will proceed by writing down the solution of Eq. (3.17) for our case.

Solution Recently, van Vliet calculated in Ref. [53] the Green's function which applies to the situation of an inhomogeneous space-charge device,

and which is the solution of Eq. (3.17) for the operator $\hat{\mathcal{L}}$ in Eq. (3.16)

$$g(x', x) \;=\; \frac{q}{\varepsilon\varepsilon_0}\, u(x' - x) \exp\left[\frac{q}{\varepsilon\varepsilon_0} \int_x^{x'} dx'' \frac{n_0(x'')}{\mathcal{E}_0(x'')}\right], \tag{3.18}$$

where $u(x' - x)$ is the step function. The dimension of g is Vm^{-1}, and concequently the dimension of W_g is V^2 [after integration in Eq. (3.15)], as it should be, since the weight function converts number fluctuations into voltage fluctuations.
In summary, knowledge of the chemical potential μ, the spatially dependent electron density n_0 and electric field $\mathcal{E}_0$, together with the defect density N_i and their occupation at specific levels suffices to calculate the noise spectrum using Eq. (3.2).

3.3 Calculation of g-r noise intensity

This section is organized as follows: first we specify the defect level distribution, the spatial dependence of the free-electron density, and the electric field. Then, the local relaxation time and the local intensity are computed. Finally, the theoretical g-r noise spectrum is computed, compared to the measurements, discussed, and linked to the intensity of electron-hole recombination noise.

3.3.1 Computational details

Defect levels

To reduce the computer time and at the same time represent faithfully the defect distribution, thirteen levels were taken into account, the conduction band level, leaving us with 12×12 matrices in our computations, due to the requirement of charge conservation. The choice for the location of the defect levels in the gap and their concentration (see Fig. 3.2) is argued as follows: Defects far below the chemical potential or Fermi level μ are almost completely occupied, therefore unable to fluctuate, contribute weakly to the noise, and can be neglected. On the contrary, mid-gap levels in the region $\mu \pm 2k_BT$ do fluctuate and were emphasized in the calculation by finer sampling. Zero energy is set to $\mu = 0$. A reasonable mid-gap defect density ($5{\cdot}10^{15}$ cm^{-3}) is equally distributed over eight levels in the energy range from -0.06 to +0.15 eV relative to μ, separated by 0.03 eV. The

tail-state density per eV is assumed to have an exponential distribution $\propto$ exp$(-(E_C - E)/E_{tail})$ below the mobility edge E_C, with the accepted characteristic energy E_{tail} of 0.03 eV. Tail state densities per level were deduced from this density per eV and condensed in one discrete level. Table 3.3.1 and Fig. 3.2 summarize the energies and defect concentrations of the twelve defect levels. The occupation of the discrete levels was calculated using

Energy (eV)	-0.06 to 0.15	0.24	0.36	0.48	0.60
N_D (cm^{-3})	5·10^{15}	6.3·10^{14}	1.6·10^{16}	1.2·10^{18}	2.4·10^{19}

TABLE 3.1: Defect levels with respect to $\mu = 0$ and their densities, which were distributed over eight mid-gap levels or a tail state energy range, to represent the real situation.

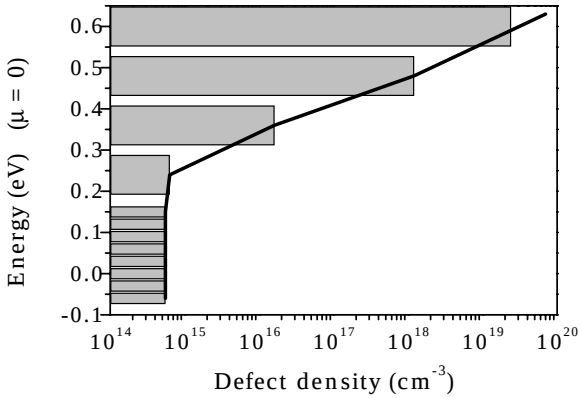

FIGURE 3.2: Defect distribution histogram with zero energy at Fermi level, E_C is 0.63 eV.

Fermi-Dirac statistics. Thermal velocity v_{th} is estimated at 2·10^6 cm s^{-1} at room temperature, and a capture cross section σ of 10^{-15} cm^2 was used (independent of energy level). The standard device area of 0.56 cm^2 was inserted to obtain concentrations per unit length.

Electron density

The electron density and the internal electric field are necessary ingredients for the computation of the local g-r noise and the Green's function. Their

spatial dependencies are obtained from fitting experimental J-V curves with AMPS. The internal electric field in the *nin* structure under investigation is virtually linear and zero in the center of the film. The field strength at the contacts due to band bending is relatively strong: -1.5 V/μm. The external electric field is more than an order of magnitude smaller under experimental conditions (50 mV/μm). The electron concentration n_0 is computed from the activation energy that is assumed to have a parabolic position dependence due to band bending (see section 2.2.4)

$$n_0(x,T) \;=\; n_{00}\exp\Big[-\frac{E_{C0}+\beta(x-x_0)^2}{k_BT}\Big]. \tag{3.19}$$

For device *B1*, the 'band bending parameter' β amounts to 1.6 eVμm^{-2}, the central activation energy E_{C0} is 0.63 eV, and the pre-factor n_{00} amounts to 3.4·10^{19} cm^{-3} according to the AMPS fit. The temperature dependence of n_0 is accounted for via the Boltzmann factor and further in the Fermi function for the occupation of levels, according to Eq. (3.10). All calculations presented in the figures of this chapter were performed for T = 363 K. Specification of $n_0(x,T)$ now makes the integration of the Green's function feasible.

3.3.2 Rates and spectra

Relaxation rates

First, we compute the relaxation rates of the individual traps that eventually determine the *spectral shape* of g-r noise. The relaxation rates τ^{-1} are the eigenvalues of the relaxation matrix $\mathbf{M}$. The case $n \gg N_i$ is treated by Van Vliet [53] and yields simple, position dependent results for the rates of levels i:

$$\frac{1}{\tau_i(x)} \;=\; \sigma v_{th}(\hat{n}_i(x)+n_0(x)). \tag{3.20}$$

This case is quite transparent: each time constant corresponds to a specific trap interacting with the conduction band. However, in our case the two regimes coexist. Near the contacts, doping sets $n \gg N_i$, and the eigenvalues are given by Eq. (3.20). In the central part $n \ll N_i$, and the eigenvalues are a mixture of terms from different levels and the full diagonalization of Eq. (3.6) has to be performed. The computation of the relaxation rates accounting for thirteen classes Of defects, described above, results for T = 363 K in rates in the range from 10^{13} s^{-1} to 10^{3} s^{-1}, and even down to 10^{-2} s^{-1} at

room temperature.
All rates produce a Lorentzian contribution to the spectrum, with a local intensity that scales with τ: The lower rates have more weight, the higher rates will be suppressed and the resulting spectrum will have a high-frequency cut-off. The minimum rate can be approximated as

$$\left.\frac{1}{\tau(x)}\right|_{min} \approx \sigma v_{th} n_0(x). \tag{3.21}$$

The corresponding eigenvector, which tells which level dominates the relaxation on the time scale of that eigenvalue, appears to be the mid-gap state. This is not surprising since transitions involving mid-gap states have a relatively high activation barrier, which makes these processes slow compared to the ones involving tail states. A typical example of the slowest rate *vs* position is presented in Fig. 3.3. Because of spatial symmetry the plot is shown only up to half of the length L of the device.

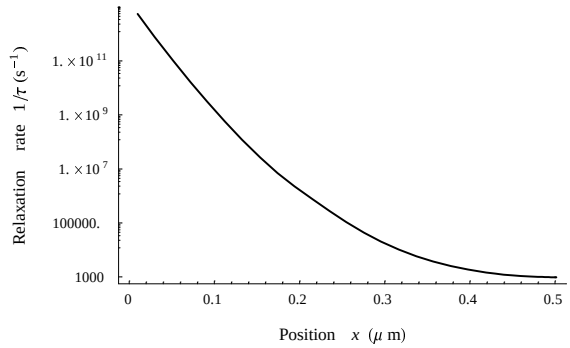

FIGURE 3.3: Slowest g-r rate *vs* position in the device, in the range from 0 to 1/2 L, for T = 363 K.

Local contributions

We proceed with the question which part of our inhomogeneous device contributes most to g-r noise *intensity*. The sources of the g-r noise are local capture and emission processes of carriers, which depend on position. This noise intensity is partially contained in the matrix elements B_{ii}, as explained in section 3.2.2. An example of the computed spatial distribution

of local g-r noise intensity $S_n(x)$, defined in section 3.2, is displayed in Fig. 3.4 for two measuring frequencies. The local g-r noise intensity S_n appears to peak around 0.2 μm from the contacts at all relevant measuring frequencies. Close to the leads, the local intensity is strongly suppressed, because $n_0 \gg N_i$, and the intensity is inversely proportional to n_0. The maximum of S_n corresponds to $n_0(x) = N_i$. Apparently, band bending, defect density and temperature all determine the local g-r noise intensity S_n.

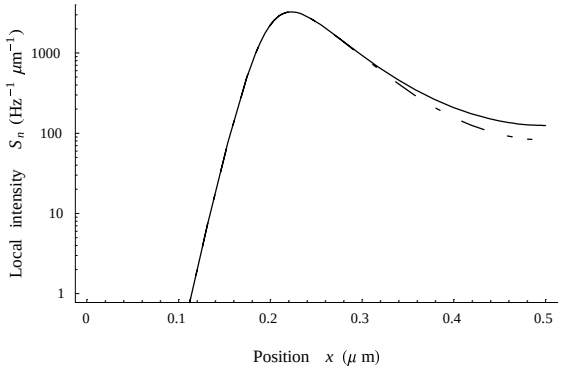

FIGURE 3.4: Local noise intensity S_n calculated for T = 363 K. Contribution to intensity at 1 Hz (full curve) and at 1 kHz (dot-dashed curve).

Green's weight function

The final step in the computation of the g-r noise spectrum is the determination of the *conversion factor* between density and voltage fluctuations, i.e. the Green's weight function. Given the internal electrical field and electron density (see section 3.3.1), the Green's function can readily be calculated. Using Van Vliet's solution Eq. (3.18) for the Green's function, the spatial weight function W_g can be determined (Eq. (3.15)). The result is plotted in Fig. 3.5. The spatial variation of the Green's weight function amounts to about one order of magnitude over the region 0.15 - 0.40 μm, exactly the region of the device that governs the g-r noise (see Fig. 3.4). This is largely due to the spatial dependence of the ratio n_0/E_0. The weight factor W_g appears to be nearly temperature independent.

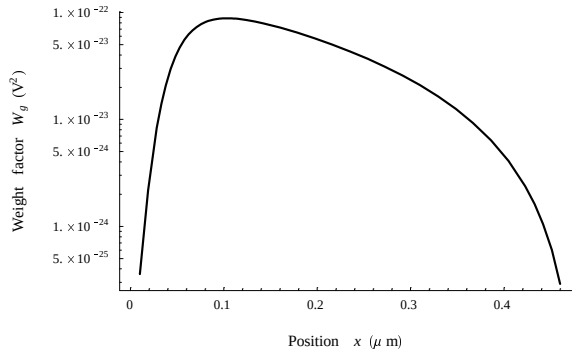

FIGURE 3.5: Weight function, which accounts for conversion of density fluctuations into voltage fluctuations, taking spatial dependent electronic drift into account.

Theoretical spectra

The complete spatial dependence of g-r noise, including transport, now can be obtained from Eq. (3.2), i.e. the product of the local Green's weight function W_g and the noise intensity per unit length S_n. Finally, the g-r spectra are calculated by proper integration of the spatial weight of g-r noise over the device. A typical example of a spectrum, calculated for a temperature of 363 K, is given in Fig. 3.6. The spectrum appears to be nearly frequency independent. This is due to the presence of a slowest rate of ≈ 1 kHz in our system. For the frequencies higher than the 'corner-frequency', located at $\approx 10^4$ Hz, a small decrease of g-r noise intensity is predicted by the model. The temperature dependence of the low-frequency part of the spectrum is listed in Table 3.2. We compare the theoretical predictions with the measured noise intensities. Unfortunately, the prediction of the g-r noise intensity is five to six orders of magnitude lower than the experimentally measured intensity in the relevant temperature range. It is even much lower than the thermal noise level under those conditions. Furthermore, the theoretically predicted intensity increases with temperature, while the experimental intensity in the low-frequency range (at 1 Hz) decreases. At this point the conclusion can already be that g-r noise theory cannot quantitatively explain the experimentally observed noise spectra, at least under the assumptions of our analysis.

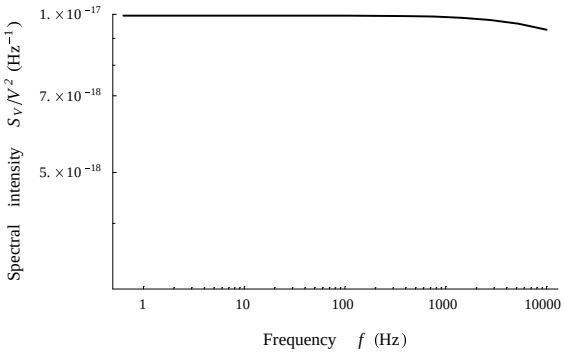

FIGURE 3.6: G-r noise spectrum of an *nin a*-Si:H device at 363 K from Eq. (3.2).

T (K)	S_V^{gr}/V^2 (Hz^{-1})	S_V^{exp}/V^2 (Hz^{-1})
340	$5.8{\cdot}10^{-18}$	$5.9{\cdot}10^{-12}$
363	$9.9{\cdot}10^{-18}$	$3.9{\cdot}10^{-12}$
402	$1.9{\cdot}10^{-17}$	$1.2{\cdot}10^{-12}$
434	$2.6{\cdot}10^{-17}$	$7.8{\cdot}10^{-13}$

TABLE 3.2: Noise intensities at 1 Hz, for g-r noise theory and experiment (*B1*).

3.4 Discussion of the model assumptions

Here, we critically discuss the choices and assumptions in the above analysis. First, the spatial dependence of the activation energy for the conduction was taken in a parabolic approximation, which clearly deviates from the real situation near the contacts. The same holds for the spatial dependence of the electrical field, which was self-consistently taken linear throughout the film. As one can see from spatial contributions of g-r noise, the contact region (< 0.1 μm), however, contributes only weakly to the spectral intensity. Therefore, a better spatial approximation near the contacts will *not* change the prediction.
Second is the choice we made for the histogram of the defect levels. The levels close to the chemical potential are partially occupied, and significantly contribute to the fluctuations. Indeed, from the computation of the noise contributions from the various levels in our *a*-Si:H layer, we conclude that levels around the chemical potential dominate g-r noise. Support for our choice of the histogram comes from the theoretical work of Lee *et al.* [19] on a trap-rich semiconductor in absence of current. The detailed sampling around chemical potential as we did, is indeed needed.
Third, a specific choice of the defect concentrations determines the capture and emission rates, and indirectly the noise intensity. This represents an insignificant uncertainty in the predictions.
We will proceed to discuss our quantitative results for the noise spectra in relation to earlier models and make a comparison with experimental data. In our earlier work [41, 57] g-r noise was treated only phenomenologically and the intensity was not computed. Our present theoretical prediction of relative noise intensity at 1 Hz is much smaller than experimentally observed. Also the maximum value of the spatial weight function (the product of S_n and W_g) deviates from the maximum of the phenomenological weight function [57], which was adjusted to the fit the experimental noise spectrum. In retrospective, for the phenomenological approach an unrealistically large weight was required. With the solution of the Green's function in 2002 by Van Vliet [53] for an inhomogeneous device, we managed to compute the absolute noise intensity for our device and found that the results are at variance with the measurements. Even when all selected values of the device parameters would change by of a factor of 10, this conclusion still holds.
As to the spectral shape, a white spectrum with a weak spectral decay is computed, while experimentally a $1/f$ spectrum is observed. This implies that g-r noise can not be the origin of the *broad distribution of activation en-*

ergies, obtained by Verleg and Dijkhuis [41] using the approach of Dutta, Dimon and Horn [18]. For the case $n_0 \gg N_i$, the spectral shape predicted by Van Vliet's g-r noise theory [53] is a $1/f$ spectrum over at most two decades (in case of a flat distribution of states in the gap), both for homogeneous and inhomogeneous devices. We checked and confirmed that prediction with our program. In our case, however, $n_0 \ll N_i$ in the central part of the device, and $n_0 \gg N_i$ only near the contacts, which results in a much broader distribution of activation energies, and thus in a nearly white spectrum.
Finally, we note that with increasing temperature the slowest rate shifts to higher frequencies exactly as the experimentally observed corner-frequency, defined in section 1.3 does [41]. However, the activation energy of the conduction, being proportional to n_0, equals that of the slowest rate. That is at variance with the experimental value for the corner-frequency, which is ≈ 0.1 eV higher. Therefore the experimental 'fluctuation time' [41] can not be the relaxation time predicted by g-r noise theory, involving capture and emission of the conduction electrons at traps. In relation to this issue, the hypothesis that electron-hole recombination is responsible for the experimentally observed corner-frequency (see Ref. [41]) needs a critical discussion. The relaxation time of electron-hole recombination is exactly the same as for g-r processes, since capture and emission rates determine the relaxation. On the contrary, the net recombination rate, which measures the number of electron-hole recombinations per unit time, is six orders of magnitude lower compared to the total number of capture and emission events in our device. As a result, the noise intensity due to electron-hole recombination is even below the intensity of g-r noise and cannot account for the measured intensity.
This does not mean that g-r noise is always irrelevant. One could think of situations of different geometry, where g-r noise could well be a more dominant noise source. A reduction of device area would increase the charge per unit area *and* the intensity of number fluctuations. G-r noise intensity would therefore grow faster than other types of noise, which are only proportional to inverse area. Next, increasing the device length would lead to reduced band bending, which will lead to a stronger conversion of density fluctuations into voltage fluctuations (Green's weight function).

3.5 Conclusion and perspectives

In conclusion, g-r noise in an inhomogeneous multi-level system cannot explain the observed noise spectra in *nin* devices of hydrogenated amorphous silicon. Neither capture and emission processes, nor electron-hole recombinations are the direct origin of the observed noise spectra. The measured intensities of $1/f$ noise and thermal noise exceed the theoretical predictions by far.
Leaving the geometry considerations for the moment, we are confronted with noise measurements without an explanation. Obviously, another noise source is responsible for the observed fluctuations. That source should exhibit a broad distribution of energies, as found from the Dutta-Dimon-Horn approach. That could be possible for a system with an energy distribution broader than the typical energy width due to Fermi-Dirac statistics of $\approx 4k_BT$. This was suggested by Baciocchi, D'Amico and Van Vliet [39], although they had no clue about the role of local potential fluctuations. The next chapter deals with such fluctuations, and considers charge fluctuations of defects in the structure of the material as the origin of voltage fluctuations.

Chapter 4

Long-range potential fluctuations

4.1 Introduction

In the 1980's it has been recognized that electronic transport in amorphous semiconductors is influenced by the presence of randomly located charged defects, which lead to a random potential landscape. Shklovskii and Efros [58] described a way to treat the electronic transport in a random potential landscape, in which screening plays an important role. A number of studies illustrates the importance of potential fluctuations under various conditions [1, 59, 60, 61]. Our aim is to apply a theory of local potential fluctuations to hydrogenated amorphous silicon, in particular, to a *nin a*-Si:H structure subject to a constant applied voltage perperdicular to the film, to determine the autocorrelation function of the voltage, and ultimately see if we can quantitatively explain the measured voltage noise.
The potential landscape due to the amorphous structure is strongly disordered, largely because of the variation in bond angles and bond lenghts. X-ray diffraction measurements, which are sensitive to the average (nearest) neighbor distance, show however that there is order on a lenghtscale of 1 nm [1]. Variation of the local potential landscape may produce localization of electrons. The precise nature of the localization in *a*-Si:H is unclear. It is neither pure Anderson localization [62] nor a percolation transition. Nevertheless, the typical magnitude of the fluctuations of the local potential can be estimated to be 0.2 eV (see section 4.4), and is comparable to the energy associated with the disorder of the network [1]. The corresponding local-

ization length is of the order of 1-10 nm. The amplitude of the fluctuations depends on the specific origin of the potential fluctuations. As said above, the main cause of the random potential is due to the **amorphous structure** of the material. The strongly disordered structure leads to bound localized electronic states below the mobility edge, known as the tail states. Note that even above the mobility edge, the same random landscape may create locally barriers of extra height for the emission of electrons from defects to the conduction band.
Further, the random potential is due to **charged deep defects**. Deep defects in amorphous silicon are identified as dangling bonds (non-bound silicon orbits). The random location of the defects is schematically depicted in Fig. 4.1, in which $+$ and $-$ signs indicate the charge of the defect, when present. The mean separation between charged defects is approximately 60

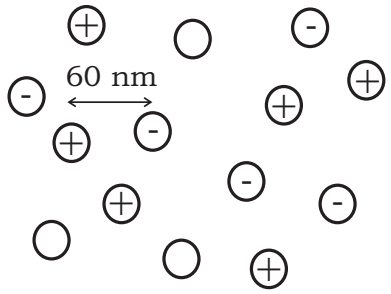

FIGURE 4.1: Random positions of charged deep defects, usually denoted as D^+, D^0 and D^- to distinguish between their charge. The random presence of opposite charge induces a random potential.

nm when two-third of the total defect density of $6{\cdot}10^{15}$ cm^{-3} is taken to be charged [13]. In (near-) intrinsic material the free electrons are relatively scarce and outnumbered far by the charged deep defects. As a result, those deep defects are not effectively screened by free electrons. The random distribution of charged deep defects leads to a static random potential, which is reduced by a *self-screening* mechanism, discussed in detail in section 4.2.3: if the charge on the defect fluctuates the surrounding defects respond by emitting or capturing electons and, as a result, screen the fluctuation of the local potential. Finally, a random potential can fluctuate because **thermally activated capture and emission of charge on deep defects**. The charge on defects located in the window of $\pm k_B T$ around the chemical potential will typically fluctuate on the time scale of the emission time τ_e, which turns out

to be in the millisecond range.
This constitutes the physical background of $1/f$ noise from number fluctuations induced by two-level transitions with a distribution of activation energies, similar to the model of Dutta, Dimon and Horn [18]. That model is phenomenological and treats thermally activated transitions between two energy levels, and a barrier energy distribution that is broad on the scale of k_BT. In a number of materials (e.g. metal oxides [21], *a*-Si:H [41]) it turned out to be a powerful description: the extracted energy distribution simultaneously explains both the frequency and temperature dependence of the $1/f$ noise. However, the model does not address the microscopic origin of the two-state systems and the mechanism by which they couple to the resistance fluctuations. As a result, the intensity of the noise remains an adjustable parameter. The DDH-analysis was successfully applied to devices of *a*-Si:H by Verleg and Dijkhuis [41], resulting in 0.2 - 0.25 eV wide distribution of activation barriers. At that time, the observations were interpreted as g-r noise. The broad distribution was explained by band bending or, alternatively, by a distribution of correlation energies. In Chapter 3 g-r noise was calculated including band bending and a distribution of defects. The noise intensity turned out to be five to six orders of magnitude smaller than observed and the explanation in terms of g-r noise thus failed.
Arkhipov and Adriaenssens [60] considered slow random fluctuations of gap-state energies producing typical $1/f$ noise characteristics in *a*-Si:H, due to a distribution of thermal activation energies for carrier release out of deep states. In their model a sinusoidal fluctuation of the conduction band edge and a $1/f$ spectral dependence were assumed. Again, their model only gives a phenomenological description and does not yield a quantitative result, based on microscopic processes.
The new theory we will use is a first-principle approach of the mechanism described by Shklovskii and Efros [58], suggested by Arkhipov and Adriaenssens for noise in *a*-Si:H, and mainly developed by B.V. Fine [63]. This Chapter describes the essential ingredients of the model and contains a detailed comparison between theory and experiments on noise in *a*-Si:H *nin* devices.

4.2 Theory

4.2.1 Autocorrelation function

In case a constant current I_0 is applied to a film with device resistance R, the measured voltage V can be written as

$$V(t) = V_0 + \delta V(t), \tag{4.1}$$

where V_0 is the average voltage ($I_0 R$) and $\delta V(t)$ is the voltage fluctuation at time t. Using the Wiener-Khintchine theorem [15], the noise spectrum $S_V(f)$ of voltage fluctuations δV can be expressed as

$$\frac{S_V(f)}{V_0^2} = 4\int_0^\infty C_V(t)\cos(2\pi f t)dt, \tag{4.2}$$

where the voltage autocorrelation function C_V reads

$$C_V(t) = \frac{\langle V(t)V(0)\rangle}{V_0^2} - 1. \tag{4.3}$$

A constant applied voltage results in the term -1, which is removed in a real experiment due to the AC coupling by the amplifier. Therefore it can be safely neglected in the rest of the treatment. We will connect the quantity of interest, the voltage autocorrelation function C_V, to resistance fluctuations and finally to potential fluctuations within the material. Our device is connected in series to a relatively high resistance R_{series} (see the setup in Fig. 2.5). Therefore, a constant applied voltage over the circuit results in a constant current I_0 through the electrical circuit. In other words, current fluctuations are negligible. Further, all measurements were performed under Ohmic conditions for the device. Therefore we can write

$$\langle V(t)V(0)\rangle = I^2\langle R(t)R(0)\rangle. \tag{4.4}$$

Experimentally we observed $S_V(f)/V^2$ to be independent of V, at least in the Ohmic regime, which validates Eq. (4.4) in our experiments. The device resistance can be written as $R(t) = R_0 + \delta R(t)$, where R_0 is the average device resistance and $\delta R(t)$ is the resistance fluctuation at time t. Inserting Ohm's law into Eq. (4.4) leads to

$$C_V(t) = \frac{\langle \delta R(t)\delta R(0)\rangle}{R_0^2}. \tag{4.5}$$

The setup thus makes resistance fluctuations observable as voltage fluctuations, provided a constant current is flowing through the film.

4.2.2 Single layer approach

The current flows perpendicularly to the plane of our μm-thin layered *nin*-structure (see Fig. 2.4). The presence of doped *n*-layers that electronically connect the undoped intrinsic layer to the leads, induces band bending of the conduction band (see section 2.2.3), that can be approximated in the center (x=0) as $E_C(x) = E_{C0} - \beta x^2$, where β characterizes the strength of the band bending (see Eq. (2.1)). The typical value of $E_C(0)$, written as E_{C0}, is 0.63 eV above the chemical potential μ. The largest contribution to the film resistance originates from the central part of the device. The fluctuations near the doped areas do not contribute significantly to the relative noise intensity, since that part has negligible resistivity due to band bending. In section 2.2.4 we introduced a "uniform resistivity layer", spreading along the x-axis between $-x_T$ and x_T, to simplify matters and to faithfully approximate the actual resistivity profile. The length of the uniform resistivity layer reads

$$2x_T = \sqrt{\frac{\pi k_B T}{\beta}}. \tag{4.6}$$

Note that band bending is accounted for via β in the value of x_T.
The resistivity within the "uniform resistivity layer" fluctuates as a consequence of the fluctuation of the screened Coulomb potential $\phi(t, \mathbf{r})$ created by all deep defects: When the potential $\phi(t, \mathbf{r})$ fluctuates, the electrons respond and track it, thus effectively $E_C(t, \mathbf{r}) = E_{C0} + e\phi(t, \mathbf{r})$, where e is the electron charge, and E_{C0} characterizes the layer of uniform resistivity.Therefore, a fluctuation of the local potential results in a corresponding change of the activation energy for emission of a carrier from a trap around the Fermi level, $E_{C0} - \mu$, to which the local density of conduction electrons will adjust. Because of the strong band bending in the real situation, the internal electrical field is large ($\mathcal{E} \approx 1.5 \cdot 10^4$ V/cm), resulting in a carrier drift time ($\approx L/\mu_n\mathcal{E}$) of less than 10^{-7} s. That shows that electron drift to and from the contacts is fast enough to be able to adjust to the fluctuating $E_C(t, \mathbf{r})$ on the time-scale of our measurement ($> 10^{-4}$ s). In summary, potential fluctuations give rise to a spatio-temporal dependent electron density.
The resistivity ρ is inversely proportional to the electron density (Eq. (2.2)). The resistivity can be used to rewrite the voltage autocorrelation function C_V in terms of the potential fluctuations ϕ. To do this, we represent the total resistivity as

$$\rho(t, \mathbf{r}) \; = \; \rho_0 + \delta\rho(t, \mathbf{r}), \tag{4.7}$$

where $\delta\rho(t,\mathbf{r})$ is a small deviation from the average resistivity ρ_0 due to local potential fluctuations. The resistivity fluctuations are accompanied by fluctuations $\delta\mathbf{j}(t,\mathbf{r})$ of the current density. The expression for the total current density is

$$\mathbf{j}(t,\mathbf{r}) \;=\; j_{0x}\hat{x} + \delta\mathbf{j}(t,\mathbf{r}), \tag{4.8}$$

with $j_{0x} = I/A$ in the $\hat{x}$-direction, where A is the device area. According to Ohm's law, we have for the electric field $\mathcal{E}(\mathbf{r}) = \rho(\mathbf{r})\mathbf{j}(\mathbf{r})$. The potential difference accross the central layer of the device is given by the integral

$$V \;=\; \frac{1}{A}\int_{-x_T}^{x_T} dx \int_{\mathcal{A}} dy\, dz\; \rho(x,y,z)\; j_x(x,y,z), \tag{4.9}$$

where we made use of the fact that the voltage drop is in the x-direction and therefore may take the current as j_x. Symmetry considerations set a constant potential value in the yz-plane at a fixed x-coordinate. The integration volume $\mathcal{V}_T$ is limited by $\pm x_T$ along the x axis and the edges of the film in the yz-plane (total area A). Linearizing Eq. (4.9) with respect to $\delta\rho$ and $\delta\mathbf{j}$ we obtain

$$\delta V(t) \;=\; \frac{1}{A}\int_{\mathcal{V}_T} [\delta\rho(t,\mathbf{r})j_{0x} + \rho_0\delta j_x(t,\mathbf{r})]d^3r. \tag{4.10}$$

The integration of the second term in Eq. (4.10) yields zero by virtue of the constraint that all current fluctuations *in plane* should cancel out, because of the continuity equation, which prescribes a constant current in the x-direction. Thus, with $j_{0x} = I/A$, we obtain

$$\delta R(t) \;=\; \frac{\delta V(t)}{I} \;=\; \frac{1}{A^2}\int_{\mathcal{V}_T} \delta\rho(t,\mathbf{r})d^3r. \tag{4.11}$$

We now write

$$\rho(t,\mathbf{r}) \propto \exp\!\left(\frac{E_{C0} + e\phi(t,\mathbf{r}) - \mu}{k_BT}\right), \tag{4.12}$$

which can be expanded provided $|e\phi(t,\mathbf{r})| \ll k_BT$ (which is to be confirmed, in Eq. (4.41), to be a reasonable assumption)

$$\delta\rho(t,\mathbf{r}) \propto \frac{e\phi(t,\mathbf{r})}{k_BT}\exp\!\left(\frac{E_{C0}-\mu}{k_BT}\right) = \frac{e\phi(t,\mathbf{r})}{k_BT}\rho_0, \tag{4.13}$$

where ρ_0 defines the average resistivity. Now, we evaluate the autocorrelation function, Eq. (4.5), using $R_0 = 2x_T\rho_0/A$ (from section 2.2.4), and inserting Eq. (4.11) and Eq. (4.13), to obtain

$$C_V(t) \;=\; \left(\frac{e}{2k_BTx_TA}\right)^2 \int_{\mathcal{V}_T} d^3r \int_{\mathcal{V}_T} d^3r' \langle\phi(t,\mathbf{r})\phi(0,\mathbf{r}')\rangle. \tag{4.14}$$

We note that the expression for C_V in terms of spatio-temporal potential fluctuations, is independent of resistivity ρ_0, simply because resistance R_0 and resistance fluctuations $\delta R(t)$ are *both* proportional to ρ_0. The next task is to describe the screening mechanism and specify the deep defects in the undoped *a*-Si:H layer.

4.2.3 Screening

Weak screening of fluctuating charged defects is an important issue in our treatment, and is described by the theory of Shklovskii and Efros [58]. The screening length - the scale at which the Coulomb potentual due to the extra charge is reduced by a factor of 1/e - ranges from 0.1 to 0.5 μm in our device, as we will demonstrate below. First, we will introduce the concept of self-screening, and later we add the other, more obvious screening mechanism, i.e. screening by the contacts.
We will not consider the static part of the Coulomb fluctuations here, but only the *fluctuating part* that we hold responsible for the measured slow timescale of fluctuations. Consider defects located in the gap in the window of $\pm k_B T$ around the Fermi energy, which fluctuate on the timescale τ_e (the emission time from the Fermi level). These defects will be called *active defects*, and are indicated in dark gray in Fig. 4.2. Their density n_T is a fraction $2k_BT/\Delta E$ of the total midgap defect density n_D, where ΔE is the width of the Gaussian distribution of midgap states. Electron emission or capture will change the charge state of a defect, and as a result change the local potential. The defects will be treated as point charges, with a charge q_i= -e for D^-, +e for D^+, and 0 for D_0 (the three charge states of a defect were defined in section 1.1.2). The Coulomb potential caused by unscreened active defects at a point **r** in space is (in CGS units according to the notation used Ref. [63])

$$V(\mathbf{r}) = \sum_i \frac{q_i}{\varepsilon|\mathbf{r} - \mathbf{r_i}|}, \tag{4.15}$$

where the sum is taken over some spatial grid, say of a size of 0.2 nm (we note that this choice will not affect any resulting formula), $\varepsilon \approx 12$ is the dielectric constant and $\mathbf{r_i}$ the radius-vector of the center of the i-th grid element.
Since $V(\mathbf{r})$ is the sum of many small and random contributions, the mean

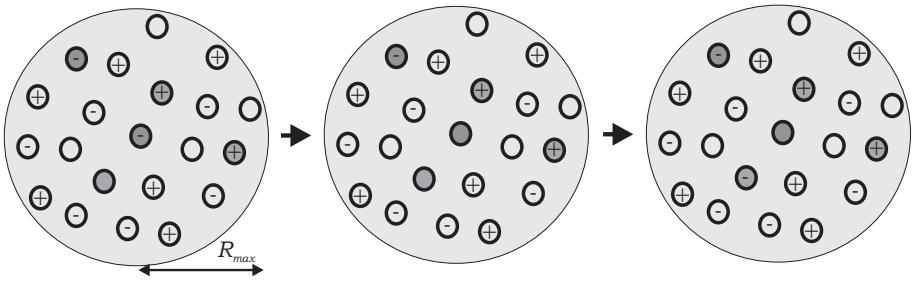

FIGURE 4.2: Cartoon of a charge fluctuation of a D^- defect, affecting the local potential, to which an active D^0 or D^+ defect (indicated by gray filling) might respond within the emission time τ_e, and effectively screen the initial charge fluctuation.

squared average of this potential is given by

$$\langle V(\mathbf{r})^2 \rangle = \sum_i \frac{\langle q_i^2 \rangle}{\varepsilon^2 |\mathbf{r} - \mathbf{r_i}|^2}, \tag{4.16}$$

where

$$\langle q_i^2 \rangle = n_T v_{cg} e^2, \tag{4.17}$$

and v_{cg} represents the volume of one element of the grid. In the last step the general principle of statistical averaging for N particles was used: $\langle N^2 \rangle = N$ (Poisson statistics).

Self-screening

The next step is the introduction of a new variable $\mathbf{R} = \mathbf{r} - \mathbf{r_i}$, and, with the help of Eq. (4.52), to transform the sum in Eq. (4.16) into an integral

$$\langle V(\mathbf{r})^2 \rangle \;=\; \frac{\langle q_i^2 \rangle}{\varepsilon^2} \int_0^{R_{max}} \frac{1}{R^2} \frac{4\pi R^2 dR}{v_{cg}} \;=\; \frac{4\pi n_T e^2}{\varepsilon^2} R_{max}. \tag{4.18}$$

The cutoff R_{max} is introduced in the above integral, in order to prevent the integral from diverging. The physical origin of this cutoff is as follows. If the local potential fluctuates to a value lower than the average E_C, the emission probability of local defects will increase and reactions $D^- \rightarrow D^0 + e$ and $D^0 \rightarrow D^+ + e$ will occur. A local fluctuation of the potential will thus be partly compensated by local feedback reactions. That compensation mechanism, or *self-screening*, causes a significant decrease of the potential fluctuation experienced at the edge of a subvolume R_{max}^3. Now we will demonstrate the existence of such a cutoff R_{max} by a self-consistent procedure.

The length scale R_{max} is taken as the characteristic length scale of The range over which the individual potential fluctuations are felt, and $\frac{4\pi}{3}R_{max}^3$ the corresponding volume. In that typical volume there are $N_{R_{max}} = \frac{4\pi}{3}R_{max}^3 n_T$ active deep defects. Thermal fluctuations of these defects in a limited time span will affect the occupation numbers of active defects. Consequently the potential exprerienced at the border of the volume changes by a typical root-mean-square (rms) value of $V_{rms} = \sqrt{\langle V(\mathbf{r})^2 \rangle}$.
As a result, the occupation number of the active defects will change, since the thermal emission rate $1/\tau_e$ of the defects is affected by the energy barrier change due to the potential fluctuation, while the capture rate remains constant. Capture processes are determined by the collision probability of conduction electrons with a fixed number of defects. The change in the emission rate is

$$\frac{1}{\tau_u} = \frac{1}{\tau_e}\left|\exp\left(\pm\frac{eV_{rms}}{k_BT}\right)\right| \approx \frac{1}{\tau_e}\frac{eV_{rms}}{k_BT}, \tag{4.19}$$

where we assumed $eV_{rms} \ll k_BT$, which will be shown to be valid in Eq. (4.23).
A potential fluctuation thus drives the change in the occupation numbers of the defects via a change in the emission rate $1/\tau_u$. But after a time τ_e, the typical equilibrium emission time (equal to the capture time), the occupation number on the average will be driven in the opposite way. Therefore, during that time τ_e, the number of active defects that will change their occupation numbers in a systematic way is limited to:

$$\Delta N_{R_{max}} = N_{R_{max}}\left[1 - \exp\left(-\frac{\tau_e}{\tau_u}\right)\right] \approx N_{R_{max}}\frac{\tau_e}{\tau_u} = \frac{N_{R_{max}}eV_{rms}}{k_BT}. \tag{4.20}$$

The number of active defects is able to produce a feedback change in screening the local potential amounting to $e\Delta N_{R_{max}}/\varepsilon R_{max}$, which is, using Eq. (4.20)

$$\frac{e\Delta N_{R_{max}}}{\varepsilon R_{max}} = \frac{e^2 N_{R_{max}} V_{rms}}{\varepsilon R_{max} k_B T} = V_{rms}, \tag{4.21}$$

and equals the (effective) root-mean-square potential evaluated at R_{max}, V_{rms}. In this way, the procedure is made self-consistent, i.e. valid for a specific combination of the screening radius and potential. In this example, the value of R_{max} is obtained from condition Eq. (4.21) together with the expressions for $N_{R_{max}}$ and n_T, and using ε = 12, ΔE = 0.15 eV, and n_D =

$6{\cdot}10^{15}\mathrm{cm}^{-3}$,

$$R_{max} \;=\; \sqrt{\frac{3\varepsilon k_B T}{4\pi e^2 n_T}} = \sqrt{\frac{3\varepsilon \Delta E}{4\pi e^2 n_D}} \approx 0.2\mu\mathrm{m}, \tag{4.22}$$

which is smaller than, but of the same order as, the thickness of the device. In what follows, the generalized screening radius r_s will replace R_{max}. This r_s sets the lengthscale of independent regions of potential fluctuations. The current estimate is close to the length of 0.26 μm of the "uniform resistivity layer" (see the previous section). The size of an independently fluctuating region is thus given by an area of $\sim r_s^2$ times a depth $2x_T$, as illustrated in Fig. 4.3. It is therefore justified to regard the device as a single, uniform layer. The number of defects in an independent region is estimated to about 200. Now, the characteristic value of the potential fluctuations can be obtained

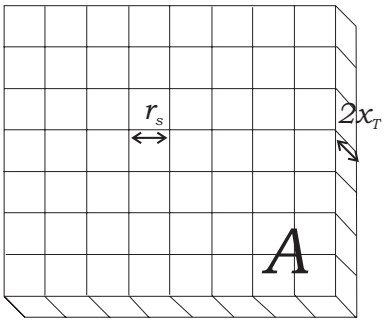

FIGURE 4.3: Illustration of the subdivision of device area A into individual pieces of the typical screening length $r_s = R_{max} \approx 0.2$ μm. The dimension perpendicular to the device area has length $2x_T$.

from Eq. (4.18) to estimate the fraction of thermally active defects

$$eV_{rms} \;=\; \frac{e}{\varepsilon}(12\pi n_D e^2 \varepsilon \Delta E)^{1/4}\sqrt{\frac{k_B T}{\Delta E}} \approx 5\ \mathrm{meV}. \tag{4.23}$$

This estimate justifies our assumption $eV_{rms} \ll k_B T$ for a typical temperature of 350 K ($\approx$ 30 meV) and higher.

4.2.4 Description of deep defects

An important concept is the way in which charge fluctuations of deep defects couple to resistance fluctuations. As mentioned before, charged deep

defects create a random potential landscape due to their random positions. Moreover, defects can switch between positive, neutral, and negative charge states which induces fluctuations in the number of free electrons and is measured as electrical noise. The energy levels E of the deep defects that characterize the transition $D^+ \leftrightarrow D^0$ can be assumed to be distributed according to a Gaussian profile $p(E)$ around a central position E_0 and a width ΔE

$$p(E) \;=\; \frac{1}{\sqrt{2\pi}\Delta E}\exp\Big[-\frac{(E-E_0)^2}{2\Delta E^2}\Big]. \tag{4.24}$$

The defect distribution $p'(E')$ that describes the transition $D^0 \leftrightarrow D^-$ is shifted with respect to $p(E)$ by a correlation energy U, which is required to put a second electron on a defect, and reads:

$$p'(E') \;=\; \frac{1}{\sqrt{2\pi}\Delta E}\exp\Big[-\frac{(E'-E_0-U)^2}{2\Delta E^2}\Big]. \tag{4.25}$$

In intrinsic hydrogenated amorphous the average energy of E_0 and $E_0 - U$ is known to lie in the top half of the band gap. Further, in our device band bending is considerable, and the chemical potential μ is somewhat closer to E_C than for purely intrinsic material. The density of states in the center of the undoped layer is sketched in Fig. 4.4, based on fits with AMPS. We find that μ almost coincides with the central position of the distribution $p'(E')$ associated with the transition $D^0 \leftrightarrow D^-$. Considering the 0.20-eV-difference between μ and $p(E)$, much greater than $2k_BT$, transitions between D^+ and D^0 are rare and their contribution to the average fluctuation of charge Δq is found to be a negligibly small, 0.04 %. In the following, we shall therefore limit ourselves to the description of transitions between D^0 and D^- states. In the calculations and in the paper [63], however, the two distributions were both taken into account.

To compute the average charge fluctuation $\langle \Delta q^2(E')\rangle$ due to defects, we thus consider the part associated with the transition $D^0 \leftrightarrow D^-$, which was derived in the Appendix (section 4.6) and reads:

$$\langle \Delta q^2(E')\rangle_- \;=\; \frac{e^2}{4}\mathrm{sech}^2\Big(\frac{E'-\mu}{2k_BT}+c\Big), \tag{4.26}$$

where $c = \frac{1}{2}\ln 2$ and using $\mathrm{sech}^2 y = \cosh^{-2} y$. Applying the statistical description of the occupation of defects presented in the Appendix, the probability distribution for a charge fluctuation to be caused by a defect charac-

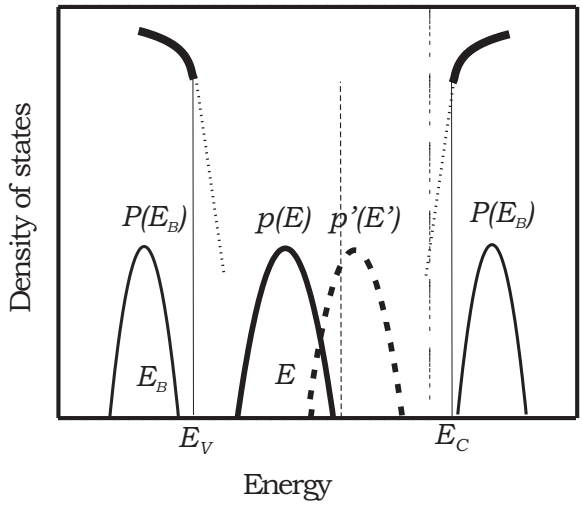

FIGURE 4.4: Schematic presentation of the density of states in the center of the band gap, including extended states below the valence band edge E_V and above the conduction band edge E_C, tail states within the band gap, and two Gaussian distributions $p(E)$ and $p'(E')$ with half-width ΔE representing defect states. Gaussian distributions of activation energies for electron or hole emission from deep traps are depicted as $P(E_B)$, with a half-width ΔE_B.

terized by an energy E' is

$$\tilde{p}'(E') \;=\; p'(E')\mathrm{sech}^2\Big(\frac{E'-\mu}{2k_BT}+c\Big). \tag{4.27}$$

The fraction of defects, which exhibit substantial charge fluctuations, is expressed as $\nu(T)$ and reads

$$\nu(T) = \frac{1}{4k_BT}\int_{-\infty}^{\infty}\tilde{p}'(E')dE', \tag{4.28}$$

where $\tilde{p}'$ represents the active (i.e. those within $\sim 2k_BT$ around μ) part of the defect distribution. To account for the total width of the applied Fermi factor, the expression is scaled by $4k_BT$. The active defects mentioned before are now expressed as $n_D\nu(T)$, representing the fraction of defects which induces the fluctuating part of the Coulomb potential. The product $n_D\nu(0)$ corresponds to the density of the defect states at the chemical potential. We note that $\nu(T)$ is only weakly temperature dependent.

4.2.5 Activation barriers

We will proceed by examining the activation barriers for emission of trapped electrons. The activation barrier E_B is simply defined as the energy difference between the chemical potential and the local value of the conduction band E_C. Due to the random network, there is *medium-range disorder* on the length-scale of 1-10 nm, resulting in a distribution of activation barriers. In Fig. 4.5 a cartoon of this disorder is given. The best description for activation barriers in an amorphous material is again perhaps a Gaussian distribution. A Gaussian distribution of width ΔE_B centered around an average barrier height E_{B0} reads

$$P(E_B) \;=\; \frac{1}{\sqrt{2\pi}\Delta E_B}\exp\Big[-\frac{(E_B-E_{B0})^2}{2\Delta E_B^2}\Big]. \tag{4.29}$$

The central energy, E_{B0}, and width, ΔE_B, of $P(E_B)$ turn out to be the only *adjustable parameters* of this theory. The distribution of activation barriers for electron is represented in Fig. 4.4 by a Gaussian distribution around position E_{B0} with a half-width ΔE_B. Holes are assumed to experience the mirror image of that distribution below the valence band.

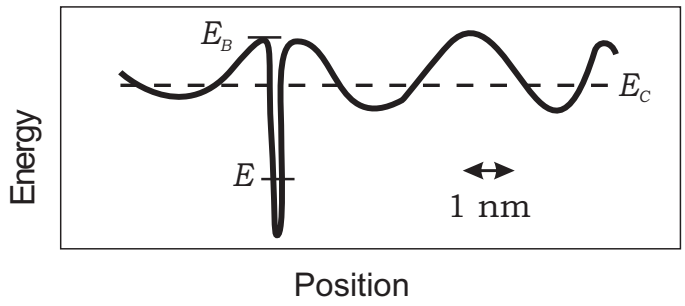

FIGURE 4.5: Cartoon of the potential barriers due to the random network and to the random positions of deep defects.

4.2.6 Rates and rate equations

The presence of a distribution of activation barriers in the material implies that electron emission rates are distributed as well. We will end up with a convolution over the barrier energies and the defect energies in our computation of the noise spectrum. Van Rheenen *et al.* [64] described the fluctuation rate $1/\tau_-$ for the $D^0 \leftrightarrow D^-$ transition

$$\frac{1}{\tau_-(E', E_B)} \;=\; \omega_0(E_B)\left[\frac{1}{2}e^{-\frac{E_B-\mu}{k_BT}} + e^{-\frac{E_B-E'}{k_BT}}\right]. \tag{4.30}$$

Here, the factor $\frac{1}{2}$ originates from the degeneracy of the D^0 state and ω_0 is the so-called attempt rate, which can be written as

$$\omega_0 \;=\; \sigma v_{th} \mathcal{N}_C(E_B). \tag{4.31}$$

Here $\sigma = 10^{-15}\text{cm}^2$ is the capture cross section, v_{th} is the thermal velocity of electrons, which amounts to $3{\cdot}10^7$ cm s^{-1} at room temperature, and $\mathcal{N}_C(E_B)$ is the effective density of states above the mobility edge, the product of k_BT and the empirical value of $N_C(E_B)$ of $1.5{\cdot}10^{22}$ eV^{-1}cm^{-3}. A typical value of ω_0 is therefore $\sim 10^{13}$ s^{-1}. The density of states above the mobility edge was fitted empirically to the data reported in Ref. [1], using $N_C(E_B) = N_C(E_{C0})\sqrt{(E_B - E_{C0} + \epsilon_C)/\epsilon_C}$, where we evaluated at $E_B - E_{C0}$ = 0.27 eV (as will result from the fit to data of device *B1*) and found ϵ_C = 0.02 eV.
The presence of a distribution of activation barriers creates a broad range of

fluctuation times in the system. If a specific defect fluctuates on time scale τ, its potential can only be screened by those defects fluctuating on time scales equal or smaller than τ. The slower defects react - on the average - too slow, keep their charge and do not contribute to the screening. Therefore, the number of active defects which responds fast enough is expressed as $n_D\nu(T)b(\tau)$, with the fraction $b(\tau)$ defined as

$$b(\tau) \;=\; \frac{1}{4k_BT\nu(T)} \int_{\mathcal{E}_-(\tau)} \tilde{p}'(E')P(E_B)dE'dE_B, \tag{4.32}$$

where $\mathcal{E}_-(\tau)$ is the subspace of the E, E_B-space which satisfies the condition $\tau_-(E', E_B) < \tau$. The thermal prefactor $4k_BT$ enters both in $b(\tau)$ and in $\nu(T)$, and therefore cancels in the expression for the generalized screening radius r_{s2}, deduced from Eq. (4.22):

$$r_{s2}(\tau) = \sqrt{\frac{\varepsilon}{4\pi e^2 n_D \nu(T) b(\tau)}}. \tag{4.33}$$

The screening due to defects in the undoped layer is one important screening mechanism in our system. The other mechanism is provided by the doped *n*-layers and contacts. Doping creates a relatively large concentration of free electrons in the *n*-layers, which provides a metallic type of screening: a (fluctuating) defect in the undoped layer is screened by its mirror images, constructed with respect to the mirror planes located at $x = \pm d/2$ (the interfaces between the doped and undoped layers).
The resulting potential is calculated, and the screening radius is determined as the distance between the location of the defect and the point where the value of the bare Coulomb potential is reduced by a factor $1/e$ (where e is the base of the natural logarithm). In Fig. 4.6 a sketch the anisotropic nature of this screening mechanism is indicated. The screening in the yz-plane is taken equal in y- and z-direction. The computation of the screening in the x-direction is more involved for a defect located off-center, since one needs multiple image-charges. The situation for a defect located at $x = 0$, however, can be dealt with using only two mirror images. We computed $r_{sx} = 0.38d$, and $r_{sy} = r_{sz} = 0.54d$. On the basis of our sketch, we estimate the screening radius due to the *n*-layers as

$$r_{s1} \;=\; (r_{sx}r_{sy}r_{sz})^{1/3} \approx 0.48d. \tag{4.34}$$

A typical value of this screening radius is $r_{s1} = 0.43\ \mu m$. In principle, the two screening mechanisms act simultaneously and independently, and add

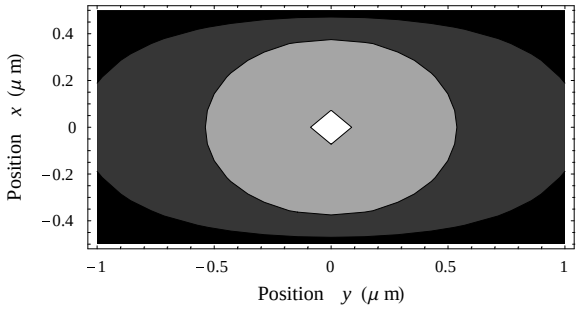

FIGURE 4.6: Anisotropic screening of a charged defect in the origin due to charge in the n-layers and contacts, located at $x \pm 0.5\mu$m. Only 2μm of the 7 mm total length in the y-direction is plotted. The contour between the light and dark gray area indicates the position where the bare Coulomb potential is reduced by a factor of $1/\mathrm{e}$ due to screening.

up. The net effect of the two mechanisms leads to a reciprocal screening radius

$$\frac{1}{r_s(\tau)} = \frac{1}{r_{s1}} + \frac{1}{r_{s2}(\tau)}. \tag{4.35}$$

In order to estimate the value of this screening radius, one needs the details of the defect distribution.

4.2.7 From potential fluctuations to noise

The Coulomb potential of a fluctuating charge Δq at coordinate $\mathbf{a}$ is screened, resulting in a potential

$$\phi(t, \mathbf{r}) = \int \frac{\Delta q(t, \mathbf{a})}{\epsilon |\mathbf{r} - \mathbf{a}|} \exp\left(-\frac{|\mathbf{r} - \mathbf{a}|}{r_s}\right) d^3a. \tag{4.36}$$

To calculate the electrical noise in Eq. 4.14, the autocorrelation function of the potential fluctuations, $\langle \phi(t, \mathbf{r}) \phi(0, \mathbf{r}') \rangle$, needs to be known. In order to be able to compute the autocorrelation function, we note that individual defects fluctuate independently, and take the disorder average. Therefore we can safely assume that the correlation does not depend on the (random) position $\mathbf{a}$ of the defects, resulting in

$$\langle \phi(t, \mathbf{r}) \phi(0, \mathbf{r}') \rangle = \frac{\langle \Delta q(t) \Delta q(0) \rangle}{\epsilon^2} F(\mathbf{r}, \mathbf{r}', \tau). \tag{4.37}$$

Here $F(\mathbf{r},\mathbf{r}',\tau)$ is approximated using the assumption that the correlation depends only on the relative distance $|\mathbf{r}-\mathbf{r}'|$ as

$$F(\mathbf{r},\mathbf{r}',\tau) \equiv \int \frac{\exp\left(-\frac{|\mathbf{r}-\mathbf{a}|+|\mathbf{r}'-\mathbf{a}|}{r_s(\tau)}\right)}{|\mathbf{r}-\mathbf{a}||\mathbf{r}'-\mathbf{a}|} d^3a \tag{4.38}$$

$$\approx 2\pi r_s(\tau)\exp\left(-\frac{|\mathbf{r}-\mathbf{r}'|}{r_s(\tau)}\right). \tag{4.39}$$

Further, for a charge fluctuation Δq_i characterized by a fluctuation time τ_i, we have $\langle \Delta q_i(t)\Delta q_i(0)\rangle = \langle \Delta q^2\rangle \exp(-t/\tau_i)$, and consequently, for the actual range of fluctuation times τ_- in Eq. (4.37):

$$\langle \phi(t,\mathbf{r})\phi(0,\mathbf{r}')\rangle = \frac{n_D}{\epsilon^2}\int\int dE_B dE' P(E_B)p'(E')F(\mathbf{r},\mathbf{r}',\tau_-(E',E_B)) \langle \Delta q(E')^2\rangle_- \exp\left(-\frac{t}{\tau_-(E',E_B)}\right). \tag{4.40}$$

¿From a general perspective, it is interesting to know what the amplitude of the potential fluctuations actually is. Recall that we assumed it to be below $k_BT \approx 30$ meV to justify the approximation made for the local resistivity fluctuations in Eq. (4.13). The amplitude of $|e\phi(t,\mathbf{r})|$ has been estimated using Eq. (4.40) as:

$$e\sqrt{\langle \phi^2(0,0)\rangle} \approx e^2\varepsilon^{-1}\sqrt{2\pi n_D \nu(T) k_B T r_s^*} \approx 3.5\text{meV}, \tag{4.41}$$

and since $|e\phi(t,\mathbf{r})| \ll k_BT$, the fluctuation of resistivity $\delta\rho$ is sufficiently small.

So far the theoretical treatment applied to transitions of the type $D^0 \leftrightarrow D^-$, which will appear to give the main contribution to the calculated noise under the condition $E_0' \approx \mu$. As mentioned above, the contributions from the $D^+ \leftrightarrow D^0$ at energy E should be added in the expressions for the fluctuation time, the screening radius, and the charge fluctuation correlation function (see Ref. [63]). In the calculations, both distributions were taken into account. In our situation this gives a slight improvement ($< 1\%$) with respect to a calculation with a single distribution $p'(E')$. The full expression for the noise is obtained by taking the Fourier transform of the autocorrelation function of ϕ (Eqs. (4.14) and (4.40)). It includes the expression for the fluctuation time τ_+, analoguous to Eq. (4.30), and further $\langle \Delta q^2\rangle$ in Eq. (4.54) resulting in:

$$\frac{S_V(f)}{V^2} = \frac{2\pi^2 e^4 n_D}{\varepsilon^2 (k_BT)^2 A x_T^2}\int dE_B\, P(E_B)$$

$$\times\Big[\int D(f,\tau_+(E,E_B))\,\tilde{p}(E)dE \;+\; \int D(f,\tau_-(E',E_B))\,\tilde{p}'(E')dE'\Big]\,, \quad (4.42)$$

where

$$D(f,\tau) \;=\; \frac{\tau r_s^4(\tau)\Big[4x_T - 3r_s(\tau) + e^{-\frac{2x_T}{r_s(\tau)}}(2x_T + 3r_s(\tau))\Big]}{1+(2\pi f\tau)^2}. \quad (4.43)$$

The Lorentzian spectrum $\tau/(1+(2\pi f\tau)^2)$ in D originates from Fourier transformation of the exponential decay function in time which characterizes the charge fluctuations (see Eq. (4.40)), while the restriction of the integration space by the area A and the length of the uniform resistivity layer x_T, results in the form $r_s^4[\ldots]$ and is responsible for the other terms in Eq. (4.43).
A quantitative analysis is carried out using Eq. (4.42). For the qualitative analysis we can reduce Eq. (4.42) to a more transparant expression for the noise spectrum, by taking the limits $x_T \ll r_s$, valid for the faster fluctuation processes, and $k_BT \ll \Delta E_B$, and finally approximating the number of active defects by the $k_BTn_D/\Delta E$, which sets $\nu(T) = \frac{1}{2\Delta E}$, and approximates the Gaussian defect distribution to a flat one of width ΔE. In these limits, the theoretical expression for the noise reads

$$\frac{S_V(f)}{V^2} = \frac{8\pi^2e^4n_D}{\varepsilon^2k_BT\Delta EA}\int \frac{\tau(E_B)r_s^3(\tau(E_B))P(E_B)dE_B}{1+(2\pi f\tau(E_B))^2}. \quad (4.44)$$

Note that in this approximation the fluctuation time τ does not depend on E' nor E anymore:

$$\tau(E_B) = \frac{3}{2}\omega_0(E_B)\exp\Big(-\frac{E_B-\mu}{k_BT}\Big). \quad (4.45)$$

In contrast to the case of g-r noise (see Eq. (3.2)), *the resulting expression is independent of the number of conduction electrons*. Further, the inverse proportionality of the noise to area A is very common, since takes the number of fluctuators in a volume into account. The dependence on the concentration of deep defects is only weak: the n_D dependence of the prefactor is balanced by the $1/\sqrt{n_D}$ dependence of r_{s2}, which constitutes a part of the screening radius r_s and which enters as r_s^3 in Eq. (4.44). Due to the proximity of the *n*-layers, and the resulting value of r_{s1} which competes strongly with r_{s2} in the relevant low-energy region, the n_D-dependence of the noise intensity is even weaker than $1/\sqrt{n_D}$.
In summary, this theory provides a quantitative prediction for both the prefactor of the noise and the distribution of energy barriers which is eventually responsible for the electrical noise.

4.3 Temperature dependence

The theory of long-range potential fluctuations results in an equation for a noise spectrum which depends on temperature. In this section noise spectra in a broad temperature range are presented and analyzed with the theory of potential fluctuations. The emerging fitted distribution of potential barriers, responsible for the fluctuations is discussed.

4.3.1 Noise spectra

The temperature dependence of conduction and noise was measured for the devices specified in Tab. 2.1. The qualitative behavior of our *a*-Si:H *nin* devices is in accordance with earlier work in our group [41]. The expected inverse proportionality of the noise intensity on device area was verified experimentally.
All measurements described in this section were carried out on device *B1* at 50 mV in the Ohmic regime. The temperature was varied from 295 K up to 434 K, the higher bound in order to avoid out-diffusion of hydrogen and structural rearrangements, the lower bound because below room temperature the device has a too large resistance for carying out low-frequency noise measurements.

In Fig. 4.7 we present a set of noise spectra for a range of temperatures, which are shifted by 30^3, 30^2, and 30 to separate them from each other; scale refers to the 340-K-spectrum. The theoretical curves, using the device parameters mentioned in the previous sections, are included in Fig. 4.7. The prefactor of the theoretical noise intensity in Eq. (4.42) is directly determined, without adjustable parameters, from the known device parameters such as area, defect density, the characteristic length of band bending x_T, and the temperature T. Our main result is that the theoretical prediction of the noise intensity is of the right magnitude for all temperatures. We stress again that the theory has only *two* adjustable parameters: the width ΔE_B and the central position E_{B0} - μ of distribution of potential barriers. These parameters only influence the spectral shape, but not the intensity. The spectral shape and its temperature dependence all fit very well. Below, the fitted values for ΔE_B and E_{B0} will be discussed.

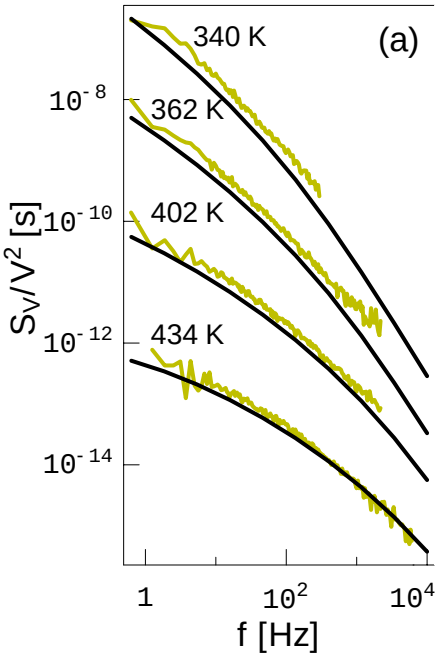

FIGURE 4.7: Noise spectra measured in the Ohmic regime, at 50 mV. Erratic lines indicate experimental data and smooth lines predictions of Eq. (4.42), to real scale for T=434 K. Spectra at 340 K, 362 K, and 402 K are multiplied by 30^3, 30^2 and 30, respectively, to make them distinguishable. When all plotted on the same scale, difference in intensity are less than one order of magnitude.

4.3.2 Distribution of potential barriers

The parameters of $P(E_B)$, the Gaussian probability distribution of potential barriers in the conduction band, is extracted from the data given in Fig. 4.8. The peak E_{B0} is at 0.90 eV above μ and the width ΔE_B = 0.09 eV. Since

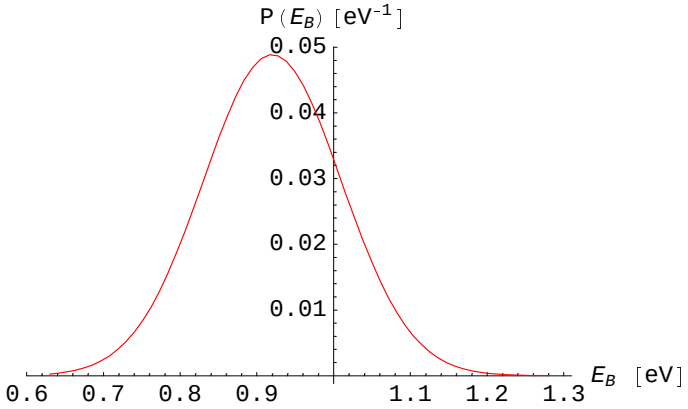

FIGURE 4.8: The Gaussian distribution of emission barriers as experienced by electrons in deep traps. The chemical potential μ is set to zero. The central position E_{B0} and the width ΔE were adjusted to obtain the curvature which fits best to the data.

$E_{C0} - \mu$ = 0.63 eV, we arrive at $E_{B0} - E_{C0}$ = 0.27 eV. According to AMPS simulations (see Table 2.2, the *B1* device parameter n_D is $(6 \pm 2) \cdot 10^{15}\text{cm}^{-3}$ and $E_0' = \mu \pm$ 0.02 eV. As a consequence, the values of E_{B0} and ΔE_B are subject to an error of 20 %.
The screening radius r_s is plotted in Fig. 4.9 in the relevant energy range of E_B. For high energy barriers, a larger fraction of the defects can respond fast enough to screen local potential fluctuations, resulting in a smaller screening radius. For low energy barriers the screening is only by the *n*-layers with a corresponding screening radius of $\sim 0.4\ \mu$m.
In Fig. 4.10, we present as a full line the weight distribution function $r_s^3 P(E_B)$. This function weighs the contribution to the noise from transitions characterized by a barrier of E_B and corresponding to a transition time τ and a Lorentzian noise spectrum $\tau/(1+(2\pi f\tau)^2)$ (see Eq. (4.44). This weight function has a shift of the peak energy of $\approx$ 0.1 eV relative to the maximum of

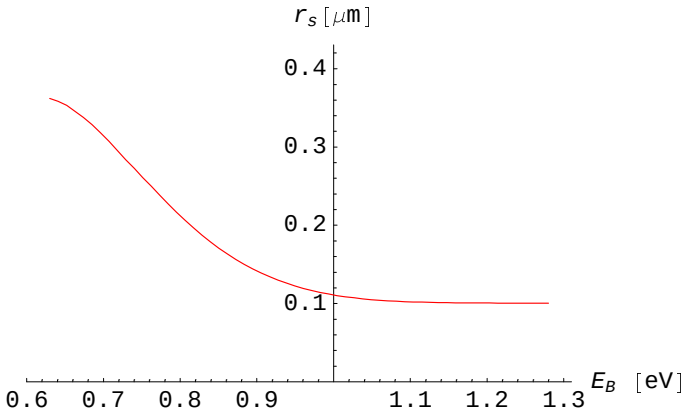

FIGURE 4.9: Screening radius, composed of screening by the free charge in the n-layers and by the self-screening mechanism of the (charged) defects. The self-screening mechanism depends on the characteristic time τ of electron emission from deep defects and thus on the barrier height E_B.

$P(E_B)$ and an asymmetrical distribution in energy.

4.3.3 Dutta-Dimon-Horn analysis

The temperature dependence of the noise spectra in *a*-Si:H was first analyzed by Verleg and Dijkhuis (see section 1.3 and Ref. [41]). The change in the spectral curvature with temperature results in a shift of the so-called characteristic frequency f_1, which is the frequency where the slope of the spectrum equals -1. When temperature is increased, the increase of f_1 appears to be thermally activated. The activation energy of the characteristic frequency for the *nin* device *B1* is 0.81 $\pm$ 0.03 eV (see section 1.3).
The results of DDH analysis on the same data of device *B1* are included in Fig. 4.10 in order to compare it with the distribution $r_s^3 P(E_B)$, the weight function of the present theory. Their shapes are identical, although their maxima are shifted slightly. We note that in case of DDH analysis the energy scale depends very much on the Arrhenius fit to the characteristic frequency f_1 *vs* temperature. The energy shift is therefore attributed to that unavoidable uncertainty. Clearly our theory provides a microscopic basis

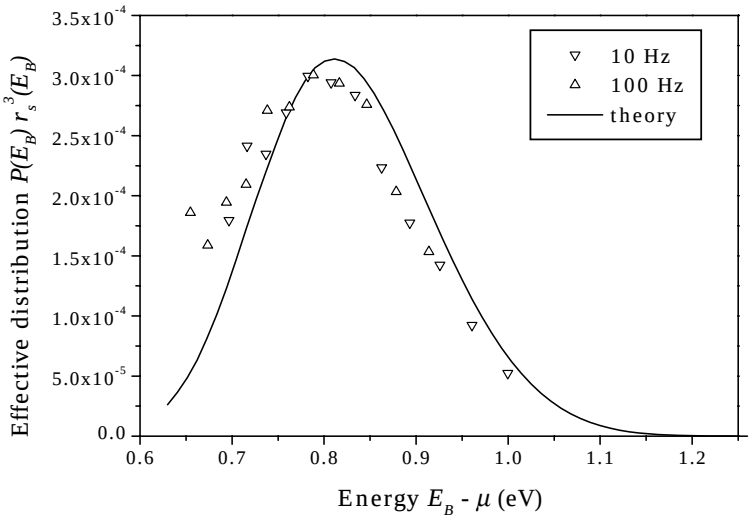

FIGURE 4.10: Effective distribution of emission barriers device *B1* measured at V = 50 mV. In good approximation, the distribution of barriers responsible for the curvature of the spectrum is the original barrier distribution weighted by the screening radius cubed. The effective distribution is peaked at a barrier energy which corresponds to the activation energy of the characteristic frequency f_1 in the noise spectrum. For comparison, the distribution of activation energies obtained with Dutta-Dimon-Horn analysis (see section 4.3.3) is included.

for the phenomenological distribution obtained from the DDH analysis.
The distribution of the barriers peaks above the conduction band edge. We claim that this is the explanation for the fact that the activation energy in the noise spectra exceeds the conductivity activation energy by 0.18 eV. We conclude that the previous assumptions [41] that noise is governed by hole dynamics is wrong.

4.3.4 Discussion of Dutta-Dimon-Horn analysis

In Verleg's analysis, the asymmetry in the DDH distribution function could not be explained. An asymmetric weight function now appears naturally from the theory of random potential fluctuations. According to our theory, the reason why a spectrum close to $1/f$ is observed is explained by the distribution of barrier heights in a random potential landscape. The theory allows for a quantitative prediction of the noise intensity, while in the DDH approach, the noise intensity is an adjustable parameter. It is noted that the $1/T$ dependence of the prefactor in Eq. (4.44) is a feature of the potential fluctuations theory, which apparently predicts the observed decrease of noise intensity with increasing temperature rather well. Also in this respect, the theory works better than the DDH approach, in which the temperature dependence of the prefactor is proportional to T. The mismatch of DDH-analysis for the temperature dependence of noise intensity in *a*-Si:H devices was not noticed before, since the noise prefactor is free to chose in that approach.

4.4 General discussion

The theoretical spectra are accurate within a factor of two, due to a number of uncertainties in the estimates. The attempt frequency ω_0 and the screening function $F(\mathbf{r}, \mathbf{r}', \tau)$ are accurate within a factor of two. Further uncertainty was introduced by the errors in the AMPS determination of the defect parameters n_D, ΔE, and E_0. Given the margin of the theoretical prediction, there is good agreement with the experimental noise spectra.
We now give two rough estimates, of the localization length of electrons and of the typical length scale of the medium-range disorder of the amorphous structure from the fitted distribution of emission barriers. Fig. (4.5) shows schematically a narrow deep energy well, of energy $E_{C0} - E$, and a wider shallower well. First, the localization length of an electron near an active

defect can be determined by the well depth E, equated to μ, and reads

$$\lambda = \sqrt{\frac{\hbar^2}{m_e^*(E_{C0} - \mu)}}, \tag{4.46}$$

where $\hbar$ is Planck's constant divided by 2π. In *a*-Si:H the minimal localization length is approximately 0.5 nm. For a better estimate, one should consider the competition between activation over the barrier and tunneling through the barrier. Second, the same equation can be applied to the barriers in the potential landscape. This gives an estimate of the "penetration depth" of electrons, and is determined by replacing μ by the local barrier height E_B in Eq. (4.46), taking the absolute value, which turns out to be around ~ 0.2 eV, resulting in a "penetration depth" of the barrier in the range from 1 to 10 nm. Also in this second estimate, still the issue will remain whether tunneling is faster of slower then the activation over the barrier.

From a practical point of view, our analysis introduces a new method of characterizing the deep defects in *a*-Si:H. In particular, our finding, that $E_{B0} - E_{C0}$ is 0.27 ± 0.05 eV, which is substantially greater than 0.1 eV - the scale of potential fluctuations seen in the drift mobility experiments [1] - may indicate that the defects are not distributed randomly in the background of the medium-range potential but, instead, located in the regions of greater local strain, i.e. around the peaks of that potential. On the other hand, there is no principal need for a symmetric distribution of barriers around the mobility edge. Therefore it could simply be the result of an asymmetric distribution.

This work is not the first in the field of spatio-temporal fluctuations of a random potential landscape. There are other convincing indications in literature of the existence of strong temporal fluctuations in the potential landscape of disordered materials. In several papers of Arkhipov and Adriaenssens [59, 60] random potential landscapes were modeled in terms of a distribution of activation energies. However, they did not attempt to derive a quantitative expression for the noise intensity, leaving the noise intensity as an adjustable parameter.

Our experimental results all refer to sandwich devices and Gaussian noise [41] and thus may have a different cause than the non-Gaussian $1/f$-noise reported by Kakalios and co-workers obtained in coplanar devices which were interpreted in terms of a limited number of fluctuating filaments [25, 27, 65]. Both in case of coplanar and sandwich devices, however, the noise is produced by temporal carrier fluctuations induced by changes in the local

potential. The coplanar structure studied, leads to non-Gaussian noise, because current has to go via long paths, which are very sensitive to the local potential. Charge fluctuations can cause current filaments to switch on and off, resulting in a noise intensity *which changes with time*. In sandwich geometry the area through which current flows is very large and the filaments, if any, are extremely short and numerous. As a result, the noise becomes uncorrelated, or Gaussian (see Ref. [41]). The time dependence of the noise intensity and thus the non-Gaussian behavior is therefore absent in our configuration. In summary, in a coplanar structure a local charge fluctuation can cause switching of filaments, while in a sandwich structure it can lead to a potential fluctuation on a time-scale related to electron emission of deep defects.
Finally, we discuss the results of Günes, Kasap and Johanson on coplanar *a*-Si:H films (see section 1.3.2) briefly in the light of the theory of potential fluctuations. The noise intensity, measured in a small frequency interval 1 Hz - 1 kHz, is comparable to ours. The strict power-law dependence reported at the lower frequencies might show a deviation at higher frequencies, which is not measurable due to the presence of a second noise mechanism.

4.5 Conclusion

The noise spectra in *nin a*-Si:H sandwich structures based on the theory of potential fluctuations are in good agreement with the experimental data. In particular, the change of the curvature as a result of variation of temperature is reproduced. The microscopic theory presented in this Chapter thus leads to a quantitative expression for $1/f$ noise. That is a quite significant achievement in the field of $1/f$ noise, which, in many cases, is described only phenomenologically, in particular by Hooge's empirical law. Our theory provides the microscopic origin of the observed noise and goes beyond the phenomenological Dutta-Dimon-Horn (DDH) model to explain $1/f$ noise. Furthermore, the theory predicts the intensity of the noise with no adjustable parameters. The noise mechanism proposed is quite general and only requires the presence of charge traps in regions of poor screening.

4.6 Appendix: Equilibrium statistical description

The equilibrium occupation numbers of the D^+, D^0 and D^- states of a defect [66] are, respectivily,

$$f_+^{eq} \;=\; \frac{1}{Z}, \tag{4.47}$$

$$f_0^{eq} \;=\; \frac{2\exp\Big(-\frac{E-\mu}{k_BT}\Big)}{Z}, \tag{4.48}$$

and

$$f_-^{eq} \;=\; \frac{\exp\Big(-\frac{2E+U-2\mu}{k_BT}\Big)}{Z}; \tag{4.49}$$

where

$$Z \;=\; 1+2\exp\Big(-\frac{E-\mu}{k_BT}\Big)+\exp\Big(-\frac{2E+U-2\mu}{k_BT}\Big). \tag{4.50}$$

The average electric charge of the defect is

$$\langle q\rangle \;=\; \frac{e}{Z}\Big[2\exp\Big(-\frac{E-\mu}{k_BT}\Big)+2\exp\Big(-\frac{2E+U-2\mu}{k_BT}\Big)\Big], \tag{4.51}$$

where e is the elementary electron charge. The mean squared value of the charge is

$$\langle q^2\rangle \;=\; \frac{e^2}{Z}\Big[2\exp\Big(-\frac{E-\mu}{k_BT}\Big)+4\exp\Big(-\frac{2E+U-2\mu}{k_BT}\Big)\Big]. \tag{4.52}$$

Thus the mean squared charge fluctuation is

$$\begin{aligned}\langle\Delta q^2(E)\rangle \;&\equiv\; \langle q^2\rangle-\langle q\rangle^2\\ =\; \frac{2e^2}{Z^2}\Big[&\exp\Big(-\frac{E-\mu}{k_BT}\Big)+2\exp\Big(-\frac{2E+U-2\mu}{k_BT}\Big)\\ &+\exp\Big(-\frac{3E+U-3\mu}{k_BT}\Big)\Big].\end{aligned} \tag{4.53}$$

Since $\exp(-\frac{U}{k_BT}) \ll 1$ for all temperatures in the experiment, we can approximate the above expression as

$$\langle\Delta q^2(E)\rangle \;=\; \frac{e^2}{4}\left[\frac{1}{\cosh^2\Big(\frac{E-\mu}{2k_BT}-c\Big)}+\frac{1}{\cosh^2\Big(\frac{E+U-\mu}{2k_BT}+c\Big)}\right], \tag{4.54}$$

introducing the statistical constant $c = \frac{1}{2}\ln 2$, which results from the degeneracy of the D^0 state. Furthermore, the two parts in the expression are associated with the two kinds of transitions, as they follow each from independent treatment from those transitions. As a result, we have for the charge fluctuations associated with the $D^0 \leftrightarrow D^-$ transitions, using $\mathrm{sech}^2 y = \cosh^{-2} y$,

$$\langle \Delta q^2(E') \rangle_- = \frac{e^2}{4} \mathrm{sech}^2 \left(\frac{E' - \mu}{2k_B T} + c \right). \tag{4.55}$$

Chapter 5

Further experimental evidence for the role of long-range potential fluctuations in the mechanism of $1/f$ noise in *a*-Si:H

5.1 Introduction

We present measurements of $1/f$ resistance noise in two different films of amorphous silicon (*a*-Si) and compare the results to the *nin a*-Si:H device studied so far. One of the newly studied films has a *nin* structure with the *n*-layers hydrogenated as well, while the intrinsic layer was deuterated. The other film has a *pip* structure with all three layers hydrogenated. These devices provide a means for new experimental tests of our recent theoretical proposal [63] explaining the origin of low frequency resistance noise in hydrogenated amorphous silicon (*a*-Si:H).
Usually, this kind of noise has a spectral shape close to $1/f$, where f is frequency. Our theory was fully developed for μm-thick films in the presence of a electric current perpendicular to the plane. It explained the resistance fluctuations by linking them to the thermal fluctuations of the occupation numbers of deep charged defects identified as dangling bonds. The noise mechanism involved the fluctuations of the long-range Coulomb potential created by those defects. The $1/f$-like spectral shape was related to the dis-

tribution of potential barriers limiting the charge carrier escape from deep defects. This theoretical picture is amenable to a first-principle calculation of the integrated noise intensity. It also yields the prefactor in front of the $1/f$ frequency dependence. In the previous Chapter we studied $1/f$ noise in an *nin* structure of *a*-Si:H . In that structure the resistance noise originated from the middle of the undoped layer, where electrons are the majority carriers. In this Chapter these spectra are compared to that of the *pip* device and deuterated device.

The above mentioned theory implies two clear predictions. First, it should be directly generalizable to the case of *pip* structure, where holes are the majority carriers in the middle of the undoped layer. In Ref. [63], it was assumed that the distribution of the potential barriers for electron escape from deep defects is related to the medium range disorder of the local potential around the defects. This type of disorder should not be much different for the holes with respect to the valence band edge E_V as compared with that of the electrons with respect to the conduction band edge E_C. Therefore, the natural expectation is that: (i) our theory should give correct $1/f$ noise intensity for *pip* structures and (ii) if the samples are grown under identical conditions, the distribution of the potential barriers obtained from the studies of *pip* structures should be nearly the same (if counted from E_V). We test the above prediction on a *pip* structure, grown in the same reactor and under similar conditions as the *nin* structure studied in Chapters 2, 3 and 4.

The second theoretical prediction is that, if the mechanism of charge fluctuations on deep defects is correctly identified in previous Chapter with the escape and the capture of carriers, then the $1/f$ noise spectrum should not depend on the substitution of hydrogen with its heavier isotope deuterium - subject of the other test presented in this Chapter.

Potentially, the "deuteration" test can also distinguish the mechanism of defect charge fluctuations due to the emission and the capture of charge carriers from another one associated with the diffusion of hydrogen atoms. This diffusion mechanism can create or annihilate the dangling bonds. Such a mechanism will certainly depend on the substitution of hydrogen with heavier deuterium. Unfortunately, the quantitative theory of $1/f$ noise associated with hydrogen diffusion is lacking. In principle, it is possible, that the isotope substitution affects only the activation prefactors of hydrogen diffusion, which would have only a very small effect on the resulting noise intensity; or, otherwise, it can also affect either the activation energies and/or the coupling to the observed noise variable $\phi(\mathbf{r}, t)$, in which case the "isotope effect" should be more noticeable.

To apply the theory described in Chapter 4 to the hole conduction noise in *pip* structures, the energy axis should be reversed, E_C and E_{C0} should be replaced with E_V and E_{V0}, respectively, and effective electron mass should be replaced by effective hole mass. In this way, all variables describing the $D^+ \leftrightarrow D^0$ transition will describe the $D^0 \leftrightarrow D^-$ transition and *vice versa*.

5.2 Devices

In this section, the most important device parameters, partly covered in Chapter 2, are given. The first device, *B1*, is the *nin* film of *a*-Si:H , the same as reported in Chapter 4. The second device, *C*, is the *pip* structure of *a*-Si:H . The third device, *D1*, is the *nin* structure, where the undoped layer was deuterated, while the *n*-layers were hydrogenated. The amorphous silicon layers were all grown by Plasma Enhanced Chemical Vapor Deposition (PECVD) at an RF field of 13.56 MHz and a substrate temperature of 468 K. The intrinsic layer of thickness d_i and area A was sandwiched between either $\sim$ 50-nm-thick *n*-type layers or, in case of device *C*, 28-nm-thick microcrystalline *p*-type layers. Doped crystalline silicon wafers were used as a substrate, and the top contact consisted of Ti/Cu layers. Further details of deposition and devices can be found in Table 5.1 and section 2.1.

The energy distribution of deep defects was modelled by two Gaussians,

	nin B1	*pip C*	*nin D1*
d_i (μm)	0.91	0.84	1.12
A (cm^2)	0.55	0.57	0.57
n_D (cm^{-3})	6·10^{15}	6·10^{15}	4·10^{15}
$E_0 - \mu$ (eV)	-0.2	0.0	-0.2
β (eV/μm^2)	1.59	1.54	1.24

TABLE 5.1: Devices parameters, defect density n_D, defect energy E_0 and band bending parameter β from AMPS analysis of J-V-curves.

shifted with respect to each other by the correlation energy U = 0.2 eV. One of the Gaussians described the $D^+ \leftrightarrow D^0$ transition and the other one $D^0 \leftrightarrow D^-$ transition. We applied the one-dimensional device simulation program AMPS [48] to fit to the measured current-voltage characteristics and thus obtained the concentration of deep defects n_D, the band bending coefficient, β, and the positions of the maximum of the first of the above

Gaussians E_0. The best fit was obtained for the values of the defect parameters reported in Table 5.1. The half-width of the Gaussian distribution ΔE was fixed at 0.15 eV, the bandgap at 1.80 eV, the carrier mobility at 10 $cm^2V^{-1}s^{-1}$, the capture cross sections at 10^{-15} cm^2, effective electron mass at 0.4 m_e, effective hole mass at m_e, and the density of states at the mobility edge at $4{\cdot}10^{21}$ $eV^{-1}cm^{-3}$. The values of $E_{C0} - \mu$ for the *nin* devices and $E_{V0} - \mu$ for the *pip* devices were obtained from the temperature dependence of the resistivity.

We measure the voltage noise spectra at frequencies in the range from 1 to 10^4 Hz and in the temperature range 340 K 434 K. All calibrated spectra were taken at 50 mV, in the Ohmic regime, and are the result of averaging over 300 individual spectra. The expected inverse proportionality of the noise intensity on device area was found experimentally. Further details of our experimental setup are described in Ref. [41].

5.3 Experimental results

***pip a*-Si:H device.** The noise mechanism for holes is tested using the *pip a*-Si:H device. The noise spectra are curved $1/f$-like spectra, with a characteristic frequency f_1 that is thermally activated (see Fig. 5.1). The experimental activation energy E_{Bexp} of frequency f_1 equals 0.94 $\pm$ 0.04 eV. The qualitative behavior of the noise spectra in Fig. 5.2 turns out to be analogous to that of *nin* devices. The theoretical curves were calculated using Eq. (4.42) but now for the hole transitions to and from charged deep defects. The integrated noise intensity is determined from the numbers given in Table 5.1 and 5.2 and in section 5.2. The central position E_{B0} of the Gaussian distribution of defects $P(E_B)$ and its width ΔE_B are the only adjustable parameters. They govern the curvature of the noise spectra. The theoretically predicted noise spectra, which have a accuracy of a factor of two, are in good agreement with the measurements. We note that the measured activation gap to the conduction band $E_{\sigma,nin} < E_{\sigma,pip}$, caused by the fact that intrinsic *a*-Si:H is slightly *n*-type. Because of the larger conductivity activation energy E_σ, the input value for E_{B0} - μ in *pip* devices is 0.15 eV larger than the corresponding value for *nin* devices (see Table 5.2 and Fig. 5.3). However, when counted from the valence mobility edge, the value of $E_{B0} - E_{V0}$ is very close to E_{B0} - E_{C0} for the *nin* device *B1*. The values of ΔE_B for the two devices are also in reasonable agreement. For this device (and for the two others), the peak of the effective distribution E_{Bdist} coincides with the experimental

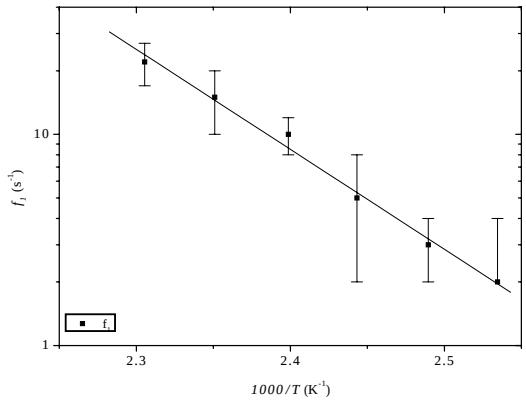

FIGURE 5.1: Arrhenius plot of the characteristic frequency f_1 as determined from the noise spectra of the *pip* device: f_1 is the frequency where the slope equals -1. The experimental activation energy is associated with the barrier energy E_{Bexp} for emission from deep traps to the valence band.

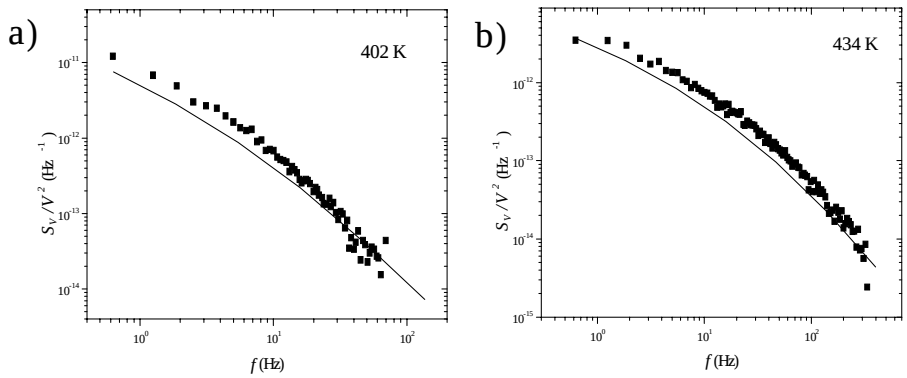

FIGURE 5.2: Noise spectra of *pip* device *C* measured at a) 402 K and b) 434 K together with the theoretical predictions.

	B1, nin	*C, pip*	*D1, nin with D*
σ_0 (Ω^{-1}m^{-1})	$(2.3 \pm 0.5)\cdot 10^4$	$(7 \pm 1)\cdot 10^3$	$(1.7 \pm 0.5)\cdot 10^4$
E_σ (eV)	0.63 ± 0.03	0.82 ± 0.03	0.67 ± 0.03
f_0 (Hz)	$(2.3 \pm 2.8) \cdot 10^{12}$	$(2 \pm 4) \cdot 10^{12}$	$(4 \pm 13) \cdot 10^{12}$
E_{Bexp}(eV)	0.81 ± 0.03	0.94 ± 0.04	0.88 ± 0.04
$E_{Bdist} - \mu$ (eV)	0.81 ± 0.06	0.98 ± 0.06	0.86 ± 0.06
$E_{B0} - \mu$ (eV)	0.90 ± 0.05	1.05 ± 0.05	0.99 ± 0.05
$E_{B0} - E_{C0}$ (eV)	0.27 ± 0.05	0.23 ± 0.05	0.32 ± 0.05
ΔE_B(eV)	0.09 ± 0.02	0.07 ± 0.02	0.11 ± 0.02

TABLE 5.2: Energy barriers and their corresponding prefactors for conduction and noise, respectively. The first four parameters are obtained experimentally. Below the line: fitted energy barriers and widths from theory.

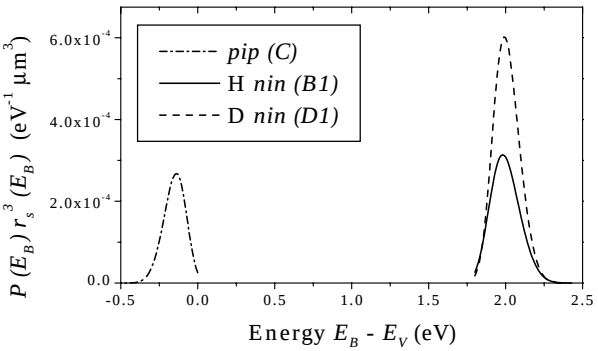

FIGURE 5.3: Effecitve distribution of emission barriers of *pip* device (*C*) below E_V and deuterated *nin* device *D1* above E_C. For comparison, the distribution of *nin* device *B1* is included.

activation energy E_{Bexp} of the characteristic noise frequency (defined in Ref. [41]), as it should.
Another parameter accessible from the experimental noise data is the *prefactor* f_0, determined from the Arrhenius plot of the characteristic frequency f_1 (see Table 5.2). For device *C*, *B1* and also for device *A* the result is the about $2 \cdot 10^{12}$ Hz. This compares well with the theoretical attempt frequency from Eq.(4.31): $f_0 = \omega_0/2\pi \approx 1.6 \cdot 10^{12}$ s^{-1}.

***nin a*-Si:D device.** Typical spectra for device *B1* (passivated with hydrogen) and device *D1* (passivated with deuterium) are shown in Fig. 5.4. There is virtually no difference between noise spectra from devices with

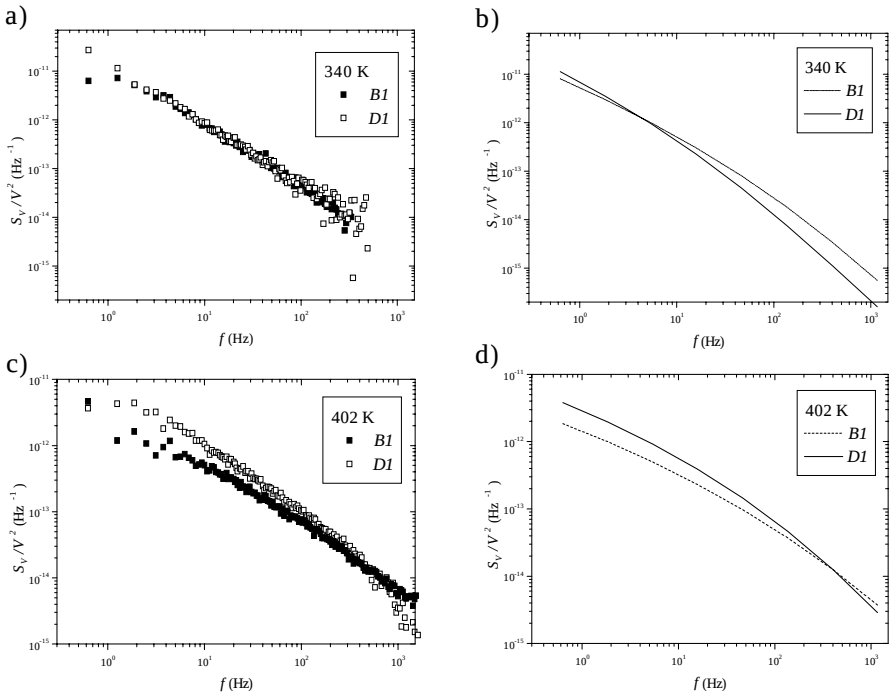

FIGURE 5.4: Noise spectra measured at a) 340 K and c) 402 K for devices *B1* and *D1*, which contain H and D, respectively. The theoretical predictions for the devices are plotted in (b) and (d) using the parameters of the Gaussian distribution of barriers, listed in Table 5.2.

hydrogen or deuterium in the temperature range from 295 K to 350 K. Elec-

tronically, the devices are identical, but have a 23 % difference in thickness (see Table 5.1). In the theory, this results in a slightly higher noise intensity for the deuterium device predominantly in the low-frequency region in the temperature range from 350 K to 434 K. Given the agreement between experiment and theory, we conclude that the main reason for the small difference of the curvature between the two devices lies in the difference in thickness, which induces an increase of the screening radius in the deuterium device. The barrier distribution for this device is characterized by the values of $E_{B0} - E_{C0}$ and ΔE_B, which are close to the values of the same parameters obtained for the hydrogenated device.

5.4 Conclusion

We have measured the $1/f$ noise spectra in *nin* and *pip* *a*-Si:H devices and in an *nin* *a*-Si:D device. In all three cases, we have found a very good quantitative agreement between the experiments and the theory proposed in Chapter 4. The theory is valid both in the regime, where electrons are the majority carriers (*nin* devices), and in the regime, where holes are the majority carriers (*pip* device). The comparison of the results gives further support for the existence of a universal distribution of emission barriers in *a*-Si:H /D for the carrier escape from deep defects.
The maximum of that distribution is located approximately 0.27 eV above the conduction band or valence band mobility edges for electrons and holes, respectively. The width of this distribution is about 0.09 eV. Comparing the results for the deuterated and hydrogenated devices, we observed no significant difference, which was also consistent with the theory.

Chapter 6

Noise study of degradation

6.1 Motivation

Metastability of *a*-Si:H is still an important scientific issue, several decades after the discovery of the Staebler-Wronski effect (SWE) in 1976. It was observed that the defect density increases upon light soaking [6]. There has been a long dispute about the microscopic origin of the SWE. Questions were raised about if and how far hydrogen atoms would diffuse after the breaking of a Si-H bond. And how saturation of the defect density would be reached. Recent developments in the field of metastability of *a*-Si:H were discussed in section 1.1.3. In this Chapter we examine the effects of degradation on the resistance noise. With the microscopic theory developed in Chapter 4, it is possible to explain changes in the noise spectra upon prolonged illumination by microscopic changes in the local potential. As in Chapter 4 and 5, the input device parameters are obtained from analysis of conductivity data. The theory of long-range potential fluctuations predicts a very weak dependence on the defect density n_D: a slight increase by a factor of ~ 1.2 for the given increase in n_D (see section 6.4.4). The theoretical prediction, however, is at variance with explorative experimental results on degradation effects on the noise spectra obtained by Verleg [41].

6.2 Measurements on silver-epoxy contacted devices

6.2.1 Measurement conditions

The first part of the degradation study was carried out on devices with similar contacts as the devices used by Verleg, while the second part of the study is on devices with wire-bonded contacts. In the first case, a silver-epoxy was used as a connection between the Ti/Cu top-contact and the Cu wire, and between that wire and a gold pad on the ceramic substrate (see Fig. 2.1). Devices were degraded in subsequent steps using 0.2 W/cm^2 irradiation from a halogen lamp, which is filtered to emit predominantly in the visible. For comparison: the intensity of the sun corresponds to 0.1 W/cm^2. An infrared filter was used to prevent the device from heating and a lens to focus the light on a few square cm and to irradiate the complete device area. After each degradation step, the conductivity and noise were measured in absence of light. The hydrogenated *nin* device in this study is device *B1*, the properties of which are described in Chapter 4, while the deuterated *nin* device *D1*, which was treated in Chapter 5. It was observed that using deuterium instead of hydrogen as passivators did not affect the resistance noise and other electronic properties of the material. Another deuterium device (*D3*) was made with aluminum bonded contacts, which appears to reduce the effect of degradation on the change in the conductivity. We refer to the original state of these devices as the 'annealed state'.

6.2.2 Effect of degradation

It is generally accepted that the defect density increases rapidly in the first stage of degradation, subsequently slows down, and finally reaches a saturation value. As a result, the device resistance increases and saturates. The devices *B1* and *D1* were degraded in four and two steps, respectively, until saturation was achieved. Deuterated amorphous silicon is known to have slower degradation kinetics [67], and was therefore illuminated longer and, in the second step, with twice as much intensity. For a good comparison, the integrated irradiated energy is used as the measure for the degradation in Table 6.1. The reduction in dark conductivity after the last degradation step is a factor of 6 and 12 for device *B1* and *D1*, respectively. This difference is mainly caused by a the higher amount of irradiated energy on device *D1*. Before presenting the noise data, the concept *'variance'* is introduced. Variance of a fluctuating quantity a is defined as $var(a) = \overline{a^2} - \bar{a}^2$.

Device	*B1*	*D1*	*D3*
Irradiated energy (J)	$1.0{\cdot}10^{3}$	$3.0{\cdot}10^{3}$	$3.6{\cdot}10^{3}$
Dark σ_0 ($\Omega^{-1}\mathrm{m}^{-1}$)	$3.0{\cdot}10^{-6}$	$9.8{\cdot}10^{-7}$	$5.0{\cdot}10^{-7}$
Dark σ_{degr} ($\Omega^{-1}\mathrm{m}^{-1}$)	$4.8{\cdot}10^{-7}$	$6.9{\cdot}10^{-8}$	$1.1{\cdot}10^{-7}$

TABLE 6.1: Conductivity characteristics at 329 K before (σ_0) and after several degradation steps (σ_{degr}) of hydrogenated device *B1* and deuterated device *D1* with silver-epoxy contacts. Another deuterated device, *D3*, was connected by wire-bonding.

For a series of random events obeying Poisson statistics, the noise power S_a is twice the average number of fluctuations per unit time (Milatz' theorem: $S_a = 2\bar{a} = 2var(a)$ [15]). The variance can be obtained from experiment by integration of the measured noise intensity over the complete frequency range. In practice, the variance can only be approximated, since the integration is limited by the experimentally accessible frequency range. We study the effect of degradation on both the variance and the noise spectra.
All relative noise spectra exhibit an increase of the noise intensity upon degradation. The shape of the spectra, however, was not very much affected. Also in that respect, the integrated noise intensity does sense the effect of degradation very well. The integrated relative noise intensity, or variance, of device *D1* measured in the dark was increased by a factor of 5 due to degradation. The increase for device *B1* amounted to a factor of 2. The question is how to explain the observation of the large increase in the variance.

6.3 Analysis of noise data of silver-epoxy contacted devices

6.3.1 Parallel resistances

The use of a small dot of silver-epoxy for the top-contact has the effect that light can not penetrate into the amorphous silicon beneath the dot. As a consequence, degradation does not occur in that region, and the devices are only partially degraded. To correct for this rather trivial effect we consider two parts of the device area: the covered fraction α of approximately 4.5 ± 1 %, and the degraded fraction $1 - \alpha$.
The resistance R_α of the part α is unaffected by degradation. Since resistance is inversely proportional to the area of the conducting film, it is equal to

R_0/α, where R_0 is the total device resistance in the annealed state. The total device resistance R in a degraded state depends further on the value R_d of the uncovered part, which is connected in parallel to the covered part, and reads

$$R = \frac{R_\alpha R_d}{R_\alpha + R_d}. \tag{6.1}$$

The relationship between resistance and degradation time t_d is $R_d \propto t_d^{-1/3}$ according to experiments and to the solution of a proper set of kinetic equations [8]. Using Eq. (6.1) we find a power law dependence of R_d on t_d of -0.32 $\pm$ 0.03, in accordance with the value mentioned above.

6.3.2 Extraction of the degradation term in the noise

Now we consider resistance fluctuations in a device which is locally degraded, and we treat resistance fluctuations in the degraded part $\delta R_d(t)$ and resistance fluctuations in the non-degraded part $\delta R_\alpha(t)$. The time development of the device resistance $R(t)$ in a state of degradation is now included as an average value R and a fluctuating part $\delta R(t)$. Linearizing $R(t)$, the fluctuations in both parts give

$$\delta R(t) = \frac{R_\alpha^2}{(R_\alpha + R_d)^2}\delta R_d(t) + \frac{R_d^2}{(R_\alpha + R_d)^2}\delta R_\alpha(t). \tag{6.2}$$

The quantity of interest is the autocorrelation function of fluctuations in R: $\langle \delta R(t)\delta R(0)\rangle$. It can be expressed in terms of autocorrelation functions of both parts, as in Eq. (6.2), with the prefactors properly squared. There is no cross correlation term between the two parts, due to the separation in space. In order to compute the voltage noise power, we apply Ohm's law, $V = IR$, which implies $\delta V = I\delta R$ under constant current conditions of the experiments, use Eq. (6.1) for R, and obtain:

$$\left(\frac{S_V}{V^2}\right)_{\alpha d} = \frac{R_\alpha^2}{(R_\alpha + R_d)^2}\frac{S_{R_d}}{R_d^2} + \frac{R_d^2}{(R_\alpha + R_d)^2}\frac{S_{R_\alpha}}{R_\alpha^2}. \tag{6.3}$$

Here the noise power S_V of a quantity V denotes the Fourier transform of the autocorrelation function $\langle \delta V(t)\delta V(0)\rangle$. The measured noise relative intensity upon partial degradation (denoted by suffix αd) consists of two coupled terms. To separate these terms, the degradation-independent noise term from the covered part is expressed in the measured voltage noise intensity of the annealed state $\left(\frac{S_V}{V^2}\right)_0$. Again using Ohms' law, we have $S_R/R^2 =$

S_V/V^2 [15]. Reminding that noise intensity is inversely proportional to area, and thus to α, we obtain $\frac{S_{R_\alpha}}{R_\alpha^2} = \frac{1}{\alpha}\left(\frac{S_V}{V^2}\right)_0$. Rewriting Eq. (6.3) results in:

$$\left(\frac{S_{V_d}}{V_d^2}\right)_{\alpha d} = \frac{(R_\alpha + R_d)^2}{R_\alpha^2}\left(\frac{S_V}{V^2}\right)_{\alpha d} - \frac{1}{\alpha}\frac{R_d^2}{R_\alpha^2}\left(\frac{S_V}{V^2}\right)_0. \tag{6.4}$$

The expression is frequency independent, and therefore also applies to the integrated noise intensity (or variance).

6.3.3 Noise data of degraded part

The examination of the noise contributions from the covered and the uncovered parts tells us that in early stages of degradation, the total resistance is dominated by the uncovered part, and this part contributes greatly to the noise. Further, as light soaking continues, and the resistance of the degraded part increases, the resistance of the uncovered part becomes comparable to the (high) resistance of the small column of material below the silver dot. Then the total variance gradually will be taken over by the covered part. In the limiting case $R_d \to \infty$, no current will pass the degraded part and the noise intensity is increased by a factor $1/\alpha$, i.e. equal to the reduction of area. The correction results in a smaller increase of the integrated noise intensity upon degradation than observed in the raw data.
Fig. 6.1 shows the dependence of the variance on the degradation time for the raw data and for the degraded part only of the sample. Due to uncertainty in the measurement of the covered fraction α of the area, the prediction of the true effect of degradation varies between *no effect* for a coverage of 0.055 to *an increase* for a coverage of 0.035. In the degraded part both the spectral shape and the variance changed only by a relatively small amount. Now we will describe devices in which those small effects can be studied to better advantage.

6.4 Measurements in wire-bonded devices

Although the use of silver epoxy for the contact connections is a good choice to avoid contact noise, even the smallest dot which is possible, will cover such an area, that large corrections are needed in analyzing noise measurements due to degradation. To reduce the covered area by the contact, we used the technique of wire bonding to provide the electrical contact between

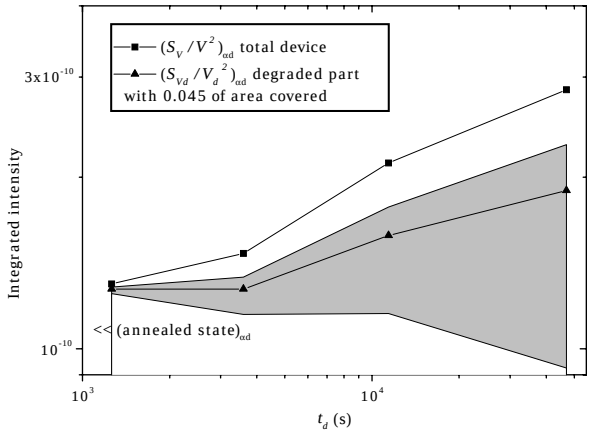

FIGURE 6.1: Variance of the *a*-Si:H device *B1* for the raw data from the entire device, and for the recalculated data, related to the degraded part, for a covered fraction of 0.045. The light gray region indicates the range of the predicted variance, given the uncertainty in the area of the covered part.

the top layer and the gold pad. We used an aluminum wire of 125-μm thickness and length of 1 mm. The value of the covered area fraction α is 0.002, a value for which the degraded part dominates the conduction and noise in the full range of degradation stages. The remaining part of the degradation study was performed on a *nin a*-Si:D device (*D3*) from the same batch as the devices *D1* and *D2*.
The rest of this Chapter will contain the characterization of this device in various stages of degradation. In the analysis with our model we need values for the defect density in subsequent stages of degradation. For that purpose, we apply and discuss two methods to the J-V characteristics. The AMPS simulation program is used to trace back the defect density by fitting to the non-linear part of the J-V curve. Alternatively, the Space-Charge-Limited-Current method (SCLC) is applied to that feature to arrive at the defect density. In section 6.4.4 we will present the degradation results, and discuss then in the light of the theory of long-range potential fluctuations.

6.4.1 Measurement conditions

The device conductivity was determined in the linear part of the J-V characteristics (see Fig. 6.3) after each degradation step, in the temperature range

from 295 K to 434 K. The activation energy of the conductivity E_σ for the device in the annealed state is 0.67 ± 0.01 eV, equal to that of *D1* and *D2*. Only after the last stage of degradation, the activation energy showed a slight increase to 0.70 ± 0.03 eV.
The degradation experiments were identical to those of section 6.2, except that a cutoff filter was placed in the beam which only transmitted light of wavelengths above 645 nm. Light of these wavelenghts (which corresponds to energies of the band gap and lower) has a relatively low absorption coefficient, and therefore a large penetration depth. As a result, the optical excitation within the layers of amorphous silicon is homogeneous, in contrast to earlier measurements. As a consequence, recombination of electrons and holes, which induces degradation, is almost uniform.
The conductivity, measured after subsequent degradation steps , is plotted in Fig. 6.2. The conductivity has a power-law dependence on degradation time, with a power 0.21 ± 0.04, close to the value of 0.25 for deuterated devices reported in literature [67]. After a number subsequent degradation steps the device broke down.

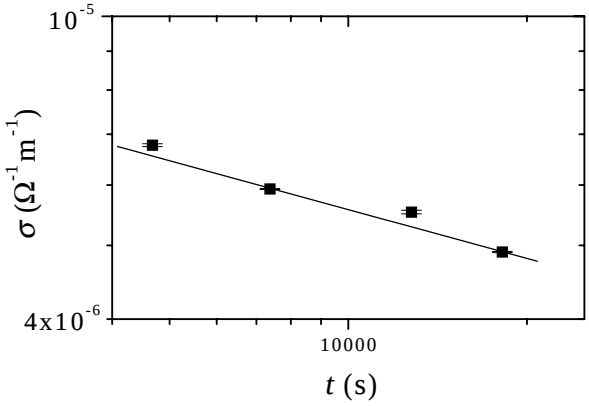

FIGURE 6.2: Conductivity of device *D3 vs* degradation time.

6.4.2 Device simulations

The one-dimensional simulation program for amorphous silicon devices AMPS-1D [48] is used to determine the density of the deep defects before and after the last stage of degradation. The idea was to determine the device parameters which fit best to the J-V characteristics of the device in the

annealed state, and subsequently to adjust exclusively the defect density and mobility to obtain an equally well fit of the J-V curve in the last stage of degradation. The obtained defect density after degradation will then be used as the higher border in theoretical calculations of the noise spectra.
The measured J-V characteristics are given in Fig. 6.3 together with the best fits of the AMPS simulation program. The non-linearity is smaller after degradation, due to a larger space charge density. The simulation program yields the defect density. As input, the following quantities were used: a

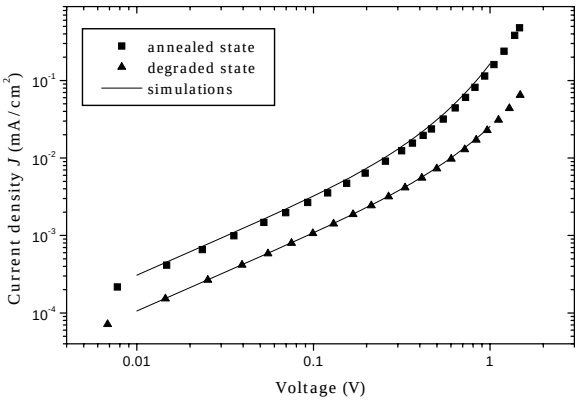

FIGURE 6.3: J-V characteristics of device *D3* before and after light soaking. For both cases the device parameters (see Table 6.2) were obtained by the best fit using AMPS.

band gap E_g of 1.80 eV, a correlation energy U of 0.2 eV, a width of 0.15 eV of the deep defect distributions, a capture cross section σ of 10^{-15} cm^2, and the measured layer thicknesses (see Table 2.1). The fit to the data in the annealed state was obtained using an electron mobility μ_n of 8 cm^{2}V^{-1}s^{-1}, a DOS $N_C(E_C)$ of 5·10^{19} cm^{-3}, and a central position of the deep defect distribution E_0 located 0.17 eV below the Fermi level. As a result of the fit, the deep defect density was determined at 6·10^{15} cm^{-3}, and the band bending parameter β at 0.85 eV/μm^2.
Next, to fit to the non-linear part of the $J-V$ curve of the device in the degraded part, all parameters were kept constant, except the defect density n_D = 1.0·10^{16}cm^{-3} and μ_n = 7.2 cm^{2}V^{-1}s^{-1}. The decrease of the electron mobility compared to the annealed state is plausible. As a result, we obtained 0.69 eV for E_σ after degradation. From the AMPS simulations of the data, the relative increase of the defect density after degradation is found to be a

factor of 1.7 (see Table 6.2).

method	annealed	degraded
AMPS	$6.0{\cdot}10^{15}$ cm^{-3}	$1.0{\cdot}10^{16}$ cm^{-3}
SCLC	$6.8{\cdot}10^{15}$ cm^{-3}	$1.1{\cdot}10^{16}$ cm^{-3}

TABLE 6.2: Defect density before and after degradation of device *D3* using a white light source. The two applied methods are described in the text.

6.4.3 SCLC analysis

The SCLC method is a simple technique to determine the defect density from the non-linearity in the J-V curve [68]. We ensured that the voltage and current determination (of the data in Fig. 6.3) were accurate enough to calculate a reliable defect DOS according to the requirements in Ref. [69]. With the known length L of the intrinsic layer and temperature T, and taking $\varepsilon = 12\varepsilon_0$ for *a*-Si:H, the defect density was determined in a relatively small energy range, where it was constant. Just as in the defect model in AMPS, we assume a Gaussian distribution of defects with a halfwidth ΔE = 0.15 eV. The SCLC result is in correspondence with the AMPS result (see Table 6.2), and confirm the increase of the defect density upon degradation by a factor of 1.7. The AMPS values will be used in the theoretical prediction of the noise spectrum after degradation.

6.4.4 Noise measurements in wire-bonded devices

The effect of degradation on the noise spectra appeared to be minute: the spectral shape was unaffected while the intensity increased only by 10 %, as was found from integration over a reasonable frequency range. In Fig. 6.4 the noise spectra before and after degradation are plotted. The remarkable part of this observation is that resistance increases (see Fig. 6.2) while the noise intensity does hardly change, while in other kinds of experiments (e.g. temperature variation) a change in the resistance is usually accompagnied by a change of the noise intensity. The long-range potential fluctuation theory is applied to describe the noise spectra in the annealed and degraded stages, which differ in the defect densities and band bending parameters. The AMPS results for the defect density n_D and band bending parameter β were inserted into the theoretical calculation to produce predictions, illustrated in Fig. 6.5 for the annealed state and the last stage of degradation,

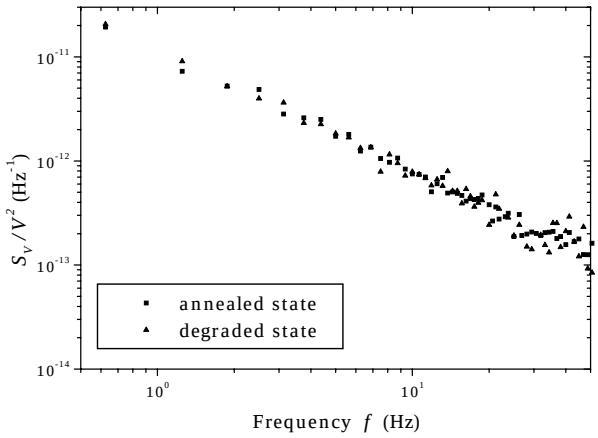

FIGURE 6.4: Noise spectra before and after prolonged light soaking. The difference is so small that the noise spectra of the intermediate steps are not shown. Measured at 329 K with 50 mV bias voltage and in absence of light.

respectively. Other input parameters taken after AMPS analysis were the energies with respect to the chemical potential: $E_C - \mu$ = 0.70 eV; $E_0 - \mu$ = -0.14 eV. In theory, the Gaussian distribution of emission barriers governs the spectral slope of the noise spectra. Since experimentally the curvature did not change significantly, the central energy $E_{B0} - \mu$ and the width ΔE_B were kept constant to their values of the annealed state (0.90 and 0.09 respectively).
Before and after degradation, the theoretical predictions for the shape agree very well with the data, and for the variance, at least within a factor of two, which is the accuracy of the theoretical prediction. On the basis of the theory, one would expect only minor changes in noise intensity and curvature, as observed.

6.5 Conclusion

The effect of prolonged illumination in an *nin* wire-bonded device (with small contact area) produced a factor of 1.7 increase of the defect density and a relative increase of the noise intensity by only 10 % at 329 K. The spectral shape remains the same. The results for the degraded part of a silver-epoxy contacted device are in correspondence with these observations in a

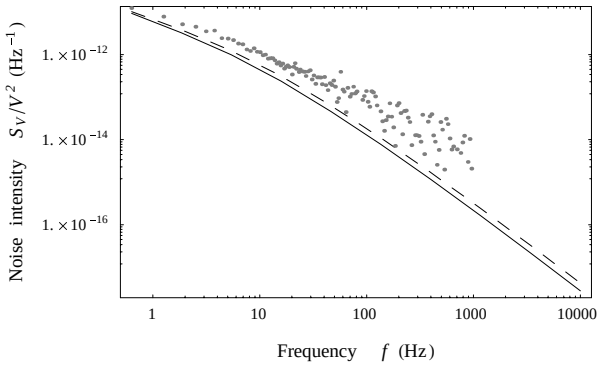

FIGURE 6.5: Theoretical predictions using the defect density from analysis with AMPS as an input parameter. The solid line is calculated using the value obtained for the annealed state, the dashed line indicates the spectrum of the degraded state. For comparison, data of the degraded state are included.

wire-bonded device. The theoretical predictions of the noise spectra are in accordance with the data, when the defect density as obtained from AMPS simulations is inserted for a limited range of defect densities.
The theory of long-range potential fluctuations as a mechanism for $1/f$ noise seems to predict the weak effect of degradation on the noise intensity properly. We recommend to redo the experiment, but with a longer degradation time to confirm our observations in a larger range of defect densities. From the constancy of the spectral shape we tend to conclude that degradation does not change the electronic energy of the defects nor their distribution in energy. To put it differently, a confirmation of this experimental study might tell that the medium-range order probed by noise measurements is not affected by degradation.

Chapter 7

Diffusion noise in TFTs

7.1 Introduction

The invention of the bipolar transistor - the first electronic switch - has been of crucial importance for the development of information technology. In computers for example, one will find the follow-up of the bipolar transistor, the field-effect transistor (FET). The current in a FET runs from source to drain, and is controlled by a gate, usually formed by a Metal-Oxide-Semiconductor (MOS) structure. The voltage applied at the gate of a MOSFET creates a conduction channel.

7.1.1 Thin-film transistors

The production of a modern version of the transistor, the thin-film transistor (TFT), is attractive because of low material costs and flexible design of devices, owing to etching techniques. The expensive *c*-Si substrate used in MOSFETs can be replaced by glass, which is cheap and allows for large-area depostion. The gate electrode in a TFT is separated from the conducting channel by a thin insulating layer (see Fig. 7.1). The gate voltage generates an electrical field at the insulator-semiconductor interface, to which electrons in the semiconductor respond. Variation of the gate voltage induces a change in the electron density near the interface, which can be used to effectively switch the resistance of the channel. Nowadays, such thin-film transistors (TFTs) are applied in active matrix displays, better known as flat panel displays, described in Ref. [70]. The transistors of our study consist of thin films of hydrogenated amorphous silicon (*a*-Si:H).

7.1.2 $1/f$ noise in the on-state of TFTs

In transistors $1/f$ noise is generally observed. Measurements have been reported on crystalline MOSFETs [71], on amorphous silicon [72, 73, 74], and polycrystalline silicon thin-film transistors [75, 76]. These measurements were invariably performed in the Ohmic regime and, of course, as a function of gate voltage. In Table 7.1 an overview of TFT noise studies is given. All mentioned transistors exhibit $1/f$ noise in the on-state, have a top-gate

Device	$W(\mu m)/L(\mu m)$	Noise	Authors
c-Si MOSFET	24/12	$1/f$ noise	Xu *et al.* [71]
a-Si:H TFT	10/4 to 400/32	$1/f$ noise	Valenza *et al.*[72]
a-Si:H TFT	15/15 to 240/15	$1/f$ noise	Boudry *et al.*[77]
Polysilicon TFT	50/10 to 50/3.5	$1/f$ noise	Dimitriadis *et al.*[75]
Polysilicon TFT	10/10	$1/f$ noise	Angelis *et al.*[76]
Polysilicon TFT	150/75 to 400/4	$1/f^{\alpha}$ noise $0.8 < \alpha < 1.2$	Deen *et al.* [78]

TABLE 7.1: Overview of earlier noise studies in TFTs.

configuration and a ratio W/L ranging from 1 to 100. A quite different class of transistors, polymer TFTs of poly-thienylene vinylene (PTV) revealed $1/f$ noise as well [79]. Usually the $1/f$ noise is described by Hooge's empirical law for voltage noise S_V [80]

$$\frac{S_V(f)}{V^2} = \frac{\alpha_H}{Nf}, \tag{7.1}$$

where N is the number of free carriers and α_H a proportionality constant, which appears to be approximately 10^{-5} to 10^{-4} in *c*-Si [72] and 10^{-2} in *a*-Si:H [72, 74]. In PTV samples the values of α_H are in the range of 0.01-0.08 [79]. In Ref. [81] a model is discussed which incorporates both number fluctuations and surface mobility fluctuations, that was later extended to include trapping noise with correlated mobility fluctuations [82]. In the latter case, trapping of charge carriers on oxide traps near the oxide-semiconductor interface leads to charge fluctuations which in turn affect the interface carrier mobility. All these measurements were performed well above threshold. We are aware of only one paper reporting on noise measurements in the off-state of *a*-Si:H TFTs, achieved by applying a negative gate voltage bias resulting in $1/f^{\alpha}$ noise with α = 0.77 $\pm$ 0.06 [77].
In recent years, much fundamental interest was raised in noise measurements on sub-micron MOSFETs at low temperatures. Especially when the

channel is at pinch-off, thus when the number of conduction electrons gradually decreases to zero along the channel, quantum-confinement phenomena were observed in the random telegraph signal (RTS) noise [83, 84, 85]. We note, however, that the pinch-off situation in MOSFETs is not comparable to the sub-threshold regime in TFTs.

7.1.3 Aim

The noise study in this Chapter is aimed to asses the effects of electron diffusion and the corresponding drift mobility in the sub-threshold regime of *a*-Si:H TFTs at temperatures in the range from 295 K to 417 K. It is of interest to answer the following questions for the near-threshold limit: (i) what is the drift mobility? (ii) how large is the induced charge in the channel? To this end we measure the effect of the gate voltage on the noise intensity. One might anticipate that, when the gate voltage is increased and the Fermi level is shifted from mid-gap to far into the tail states, the noise might contain information on the defect density.

7.2 TFT characterization

7.2.1 TFT fabrication

A batch of *a*-Si:H TFTs was deposited by HWCVD (Hot-Wire Chemical Vapor Deposition) on glass in a top-gate configuration (see Fig. 7.1). The gate electrode was deposited directly on the substrate and made accessible from the top by etching away the gate oxide and the amorphous layers. The ratio W/L was made as large as 950 by means of a meander structure, while L was kept at 50 μm. The reason for selecting a batch with a high W/L ratio is that the device resistance is sufficiently low as to perform low-frequency noise measurements successfully. The deposition of the amorphous silicon(-nitride) layers was performed in the Utrecht Solar Energy Lab. (USEL).

Further details of this batch are the following. A 300-nm-thick *a*-SiN$_x$:H layer (dielectric constant $\varepsilon_i = 7.9$) is used to separate the gate from the channel. In succession, a 200-250 nm undoped HWCVD *a*-Si:H layer and a 50-nm n^+ doped PECVD *a*-Si:H layer were deposited. Three minutes prior to the n^+ deposition, a hydrogen-plasma treatment of the silicon surface was performed to passivate surface defects and reduce contact resistance. As in all amorphous silicon transistors, an n^+-doped layer provides low-resistivity connections to source and drain. Deposition and definition of the electrodes

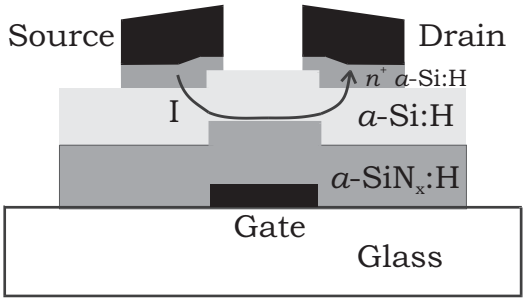

FIGURE 7.1: Schematic cross section of the top-gate TFT on a glass substrate. Patterned gate contacts are covered by a silicon nitride insulator layer. Conducting channel in the *a*-Si:H layer is near the insulator/semiconductor interface. Doped layers provide Ohmic contacts. Direction of current I is indicated by the arrow.

was performed at Philips Redhill, UK. Source and drain electrodes are 35-nm-thick layers of TiW and 500-nm-thick layers of Al sputtered on top of the n^+ layer, while gate electrodes consist only of 35-nm-thick TiW layer. Further details of the devices and the back-channel etching can be found in Refs. [86, 87].

7.2.2 Linear transfer characteristics

The output characteristics are measured by variation of the applied voltage between source and drain. As soon as the gate voltage V_G reaches the so-called threshold voltage V_T the channel starts to conduct. For low drain voltages, the drain current increases linearly with V_d, but for $V_d > V_G$, the current gradually saturates. In order to avoid saturation effects and to remain well in the Ohmic regime, we select V_d = 200 mV, where the conductance is linear with the gate voltage (see Fig. 7.2). In the on-state of a field-effect transistor the drain current I_d reads [88]

$$I_d(V_G) = \mu_D \frac{W}{L} C_i V_d \cdot (V_G - V_T), \tag{7.2}$$

where μ_D is the drift mobility, $C_i = \varepsilon_i / d_i$ is the insulator capacitance per unit area, with d_i the thickness of the insulator. Fitting to the linear part of the current-gate voltage dependence, the values of the drift mobility μ_D and threshold voltage V_T can be determined. The threshold voltage at the three

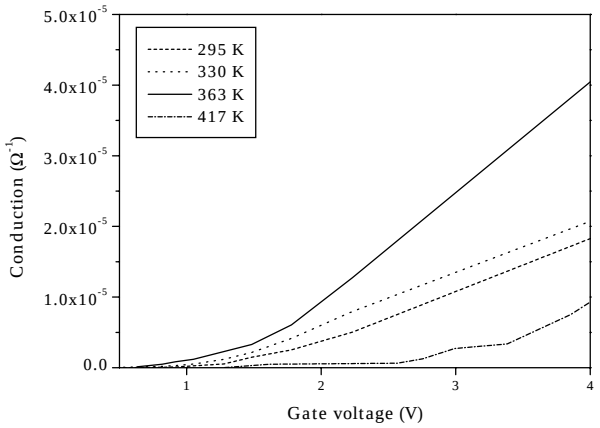

FIGURE 7.2: Linear transfer characteristics of an *a*-Si:H top-gate nitride TFT on glass, at V_d=200 mV, for various temperatures. The linear fit yields the drift mobility in the on-state (0.5 $cm^2V^{-1}s^{-1}$ at T = 417 K).

lowest temperatures of our measurements is approximately $V_T = 1.8 \pm 0.6$ V, while at T = 417 K and after some time had passed, V_T was shifted to 2.7 $\pm$ 0.6 V, probably due to structural degradation. We note that a threshold shift is commonly observed in *a*-Si:H TFTs under comparable circumstances, and that the magnitude of the observed shift is reasonable for a 'stable' HWCVD TFT. The drift mobility μ_D is determined at 0.5 to 0.6 $cm^2V^{-1}s^{-1}$, weakly dependent on temperature. These findings are in agreement with the values found by Stannowski [87] for identical devices apart from the ratio W/L (which has no effect on μ_D and V_T).

The electron mobility in amorphous materials is generally orders of magnitude smaller than in their crystalline counterparts. The value of the free-electron or microscopic mobility μ_0 in device-quality *a*-Si:H is 10 $cm^2V^{-1}s^{-1}$ and in standard-quality *c*-Si amounts to 200 $cm^2V^{-1}s^{-1}$ [1, 88]. The lower value of the microscopic mobility μ_0 is explained by disorder, which reduces the electronic mean free path. Further, the electrons contribute to the current I_d only during the time when they are free to move: The presence of defects leads to an average trapping time τ_t for electrons which is large compared to the time electrons spend freely in the conduction band, τ_f. This factor is

contained in the drift mobility μ_D quite straightforwardly,

$$\mu_D = \frac{\tau_f}{\tau_f + \tau_t}\,\mu_0. \tag{7.3}$$

Taking the usual value for μ_0 = 10 cm^{2}V^{-1}s^{-1} in device-quality *a*-Si:H, the fraction of the time an electron spends freely appears to be 0.05 for the TFT in the on-state.

7.3 Noise measurements

Noise spectra were measured using the setup described in section 2.3. A large series resistance was connected to the device in order to keep the drain current I_d supplied by the battery virtually constant. The gate voltage was provided by an additional battery. In the Ohmic regime we find $S_{V_d}(f)/{V_d}^2$ to be independent of V_d in our TFT. Given the constant current, we have $S_{V_d}(f)/{V_d}^2 = S_G(f)/G^2$, where G is the device conductance [15]. We can conclude that we deal with conductance fluctuations. Noise experiments were performed at a voltage V_d = 200 mV where the TFT is Ohmic. The spectra resulted from averaging over 300 individual spectra.

7.3.1 Noise in the above-threshold regime

In the above-threshold regime of the TFT (see Fig. 7.3) the usual $1/f$ noise-component is observed [72, 73, 74, 75, 76, 77]. That component of the noise appears to scale with $1/N$ (Hooge's law [80]), where N is the number of electrons, which can be derived from conductivity data. With decreasing N, however, a $1/f^{1/2}$-contribution gradually takes over the $1/f$ noise. The analysis of low-frequency noise data in the off-state is virtually impossible due to the high device resistance ($>$ 3 MΩ). Owing to the large W/L ratio of our device, the range in the near- and below-threshold regime accessible for noise measurements is large enough before the off-state is reached, enabling us to carry out a detailed analysis.

7.3.2 Noise spectra in the sub-threshold regime

In Fig. 7.4 a typical noise spectrum of a TFT near threshold is plotted. This spectrum was measured at T = 417 K and just at the threshold voltage. Characteristic for the noise spectra near and below threshold and at temperatures in the range from 295 K to 417 K is a power law with a slope of -1/2 at low

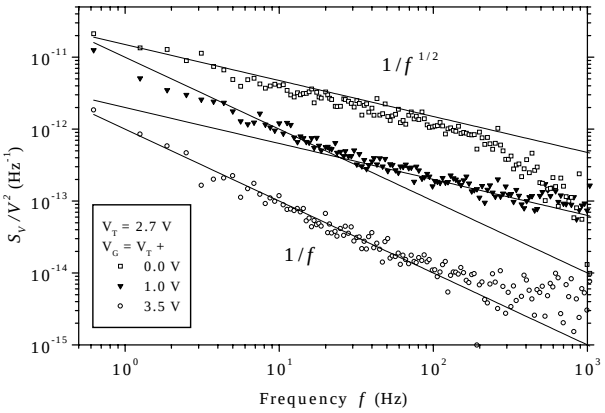

FIGURE 7.3: Illustration of two noise mechanisms effective just above threshold (at V_G=V_T+1.0 V). In the 'on-state' of the transistor, $1/f$ noise rules, whereas near threshold a $f^{-1/2}$ spectral component shows up, indicative of diffusion noise. Measurements at V_d = 200 mV and at T = 417 K.

frequencies. Another feature is the 'kink' from the -1/2- slope to a slope of -3/2 in the high-frequency range. The kink in this spectrum is at a frequency f_{kink} = 260 $\pm$ 40 Hz. The noise spectrum is quantitatively accounted for by diffusion theory, which is explained in the next section.

7.4 1D Diffusion noise

7.4.1 1D diffusion noise theory

The problem of one-dimensional diffusion noise was treated by MacFarlane and Burgess, while in two and three dimensions the problem was solved by Van Vliet and Fassett (for an overview see Ref. [17]). The problem can be solved by Green's function theory (see Chapter 3). Although our problem is in principle two-dimensional, with electrons diffusing across the length and width of the channel, the large W/L ratio of 950 reduces the problem to only one dimension: In 2D one would expect two spectral kinks corresponding to W and L, which should then be $950^2 \approx 10^6$ Hz apart from each other (see Eq. 7.6), and can not both be observed in our experimentally accessible frequency range. The transition to a spectral slope of -3/2 corresponds to the diffusion time on the shortest length scale [89] in the (2D-) system, which is clearly the channel length L. The solution of the diffusion noise equation

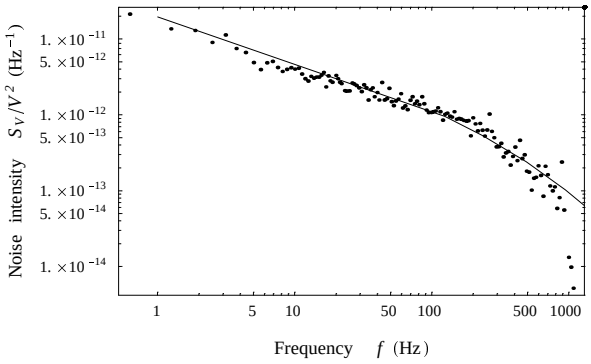

FIGURE 7.4: Typical noise spectrum of a TFT at threshold (V_G=2.7 V), V_d=200 mV and T=417 K, where G_{exp} = 1.25 $\mu\Omega^{-1}$. Full line is fitted diffusion noise spectrum, Eq. (7.4), using an effective diffusion coefficient D_{eff}=0.011 cm^{2}s^{-1} and N = 1.3·10^9.

is written in terms of the number N of electrons in a capacitive channel. Applying Poisson statistics $\overline{\Delta N^2} = N$ to the general form of 1D diffusion noise [17], we obtain

$$\frac{S_N(f)}{N^2} = \frac{L^2}{N D_{eff}\,\theta^3}(1 - e^{-\theta}[\cos\theta + \sin\theta]), \tag{7.4}$$

where $\theta = L(\pi f/D_{eff})^{1/2}$, D_{eff} is the effective diffusion coefficient and L the channel length. The solution can be separated into two spectral regions [15]:

$$\begin{aligned}\frac{S_N(f)}{N^2} &= \frac{L}{N\sqrt{\pi f D_{eff}}}, \ (f^{-1/2}\text{ branch}) \\ &= \frac{\sqrt{D_{eff}}}{NL(\pi f)^{3/2}}. \ (f^{-3/2}\text{ branch})\end{aligned} \tag{7.5}$$

7.4.2 Fits to the spectral kink

The transition between the two branches leads to a kink in the spectrum at a frequency

$$f_{kink} = \frac{D_{eff}}{\pi L^2}. \tag{7.6}$$

As mentioned above, the effective diffusion coefficient is the relevant parameter here taking due account of the fact that only a fraction of the carriers is mobile, (c.f. the drift mobility in Eq. (7.3)). In Fig. 7.4 the exact theoretical solution, Eq. (7.4), was applied to fit to the data, with the values of N and D_{eff} as fitting parameters, and with the channel length L fixed to 50 μm. The spectral form of the exact solution tracks the 417 K-data (see Fig. 7.4) satisfactorily for a value of N and of D_{eff} listed in Table 7.2. In the next sec-

$G_{exp}(\mu\Omega^{-1})$	$G_{kink}(\mu\Omega^{-1})$	N (dim.less)	D_{eff} (cm^{2}s^{-1})
1.25	2.56	$(1.3 \pm 0.2) \cdot 10^9$	0.011 ± 0.002
0.64	1.37	$(1.1 \pm 0.2) \cdot 10^9$	0.007 ± 0.003

TABLE 7.2: Fit results to the noise spectra in the sub-threshold regime of an *a*-Si:H TFT held at T = 417 K and operated at 200 mV drain bias voltage, using Eq. (7.4). Using the fit results, the conduction G_{kink} is calculated from Eq. (7.9).

tion we will see that the product ND_{eff} scales with G, resulting in value of G_{kink}, which turn out to be correspond to the measured values G_{exp} within a factor of two! We conclude already now that the electrical noise in the near-threshold region of our TFT is governed by diffusion noise.

7.4.3 Mobility from noise intensity

For most noise spectra we do not find the kink in the accessible spectral range, but do observe the $f^{-1/2}$ branch. Therefore, we can determine the values for the diffusion coefficient and thus the mobility directly from the noise intensity. Mobility and diffusion do originate from the same physical process: a random walk with a characteristic mean free path and velocity. For such a process, the *Einstein relation* is valid, which connects μ_0 to D_0, the fundamental diffusion coefficient of free carriers. The Einstein relation reads

$$\mu_D \;=\; \frac{eD_{eff}}{k_B T}. \tag{7.7}$$

Next, we use the experimental fact that S_V/V^2 is constant. Therefore, the relative number fluctuations S_N/N^2 equal the relative voltage fluctuations S_V/V^2. The expression for the noise in the $f^{-1/2}$ branch now reads:

$$\frac{S_V(f)}{V^2} \;=\; \frac{L\sqrt{e}}{N\sqrt{\pi f k T \mu_D}}. \tag{7.8}$$

We have two unknown parameters, N and μ_D, but can also measure G *vs* gate voltage. The expression for the conductivity $\sigma = Ne\mu_D/AL$ can generally be written in terms of the gate voltage V_G as:

$$N(V_G) \;=\; \frac{G(V_G)L^2}{e\mu_D(V_G)}. \tag{7.9}$$

We can compute the drift mobility *vs* gate voltage by eliminating the number N of electrons (this section), or, vice versa, eliminate μ_D to compute N (next section). Substituting Eq. (7.9) into Eq. (7.8), we obtain for the drift mobility:

$$\mu_D(S_V/V^2, V_G) \;=\; \frac{\pi f k_B T}{e^3}\left(LG(V_G)\; S_V(f)/V^2\right)^2. \tag{7.10}$$

The resulting values of the mobility are plotted as symbols in Fig. 7.5. The values for the diffusion coefficient obtained from the kinks using the Einstein relation are included in the plot as open symbols. Alternatively, the drift mobility was also determined directly from the conduction and plotted as lines in the full range of V_G. That alternative approach will be discussed in section 7.4.5. The mobility decreases slightly as the number of electrons in the channel decreases gradually, as expected from the ratio $\tau_f/(\tau_f + \tau_t)$, which also decreases. The transition to a constant mobility level at high gate voltages is in agreement with the general behavior of a transistor in the on-state, Eq. (7.2). The decrease is different for the 417 K-data, since at the time of the measurements the device had reached a different state by gate stressing, and becomes characterized by a different threshold voltage.

7.4.4 Total number N from noise intensity

The second unknown parameter, which can be extracted from combined noise and conduction measurements by elimination of the mobility, is the total number N of electrons in the channel, which yields

$$N \;=\; \frac{e^2}{\pi f k_B T G (S_V/V^2)^2}. \tag{7.11}$$

The resulting value of N is plotted in Fig. 7.6 as symbols. The dependence on the gate voltage is similar to that of conduction (see Fig. 7.2), as it should. The procedure to obtain N directly from conduction data is based on the procedure described in section 7.4.5 and results in the four lines in Fig. 7.6, for the four temperatures.

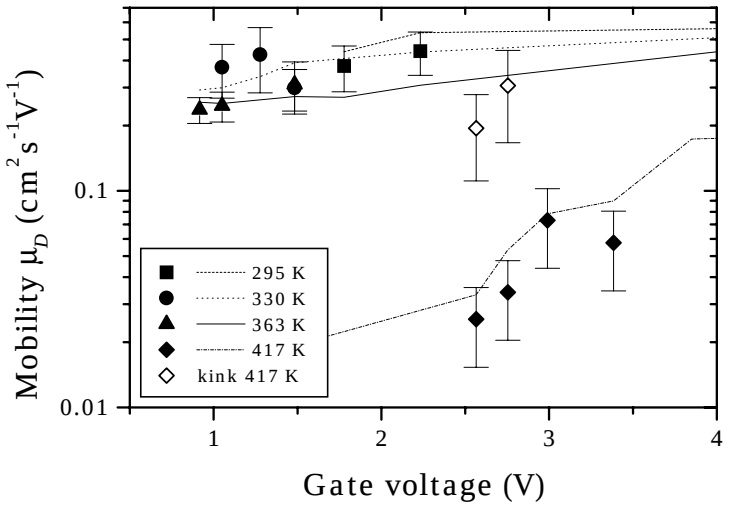

FIGURE 7.5: Drift mobility determined in three ways; from the kink (open symbols), from the combination of measured noise intensity and conduction (filled symbols), and from the measured conduction only (lines).

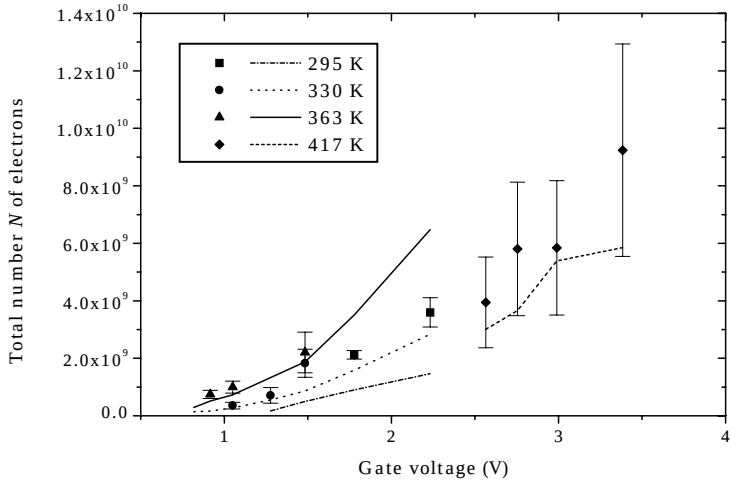

FIGURE 7.6: Total number N of electrons *vs* gate voltage. Combined noise intensity and conduction produce the data points, lines were obtained from measured conduction.

7.4.5 Mobility and N directly computed from the conduction only

In the sub-threshold regime, the current is strongly suppressed (approximately by a factor of 25, see left-hand side of the curve in Fig. 7.2). As a matter of fact, the physics of the sub-threshold regime is very complicated, because the electron concentration nearly vanishes in the channel. We consider the effects on the various parts of the expression for the current, Eq. (7.2). First, according to Eq. (7.3) a reduction in the number of free carriers results is a lower value of the drift mobility, because τ_f is reduced by trapping. Second, the capacitance C_i may decrease with decreasing V_G, because the average distance d_i at which electrons in the channel are separated from the gate contact increases. At high gate voltages, the insulator thickness limits the separation to 300 nm. At low gate voltages the average distance may rise, but no more than 400 nm, resulting in a decrease of the capacitance by a factor of two at maximum (due to the inverse propotionality of C_i to d_i). This is not sufficient to explain the full suppression of the current. Third, the width W and length L could change, but we consider these effects to be negligible.
From the above considerations, only the mobility is expected to vary with gate voltage. Then, we apply the current-voltage relation for the transistor, Eq. (7.2) to the sub-threshold regime, compute $\mathrm{d}G/\mathrm{d}V_G$ (see Fig. 7.2), and derive

$$\frac{\mathrm{d}G}{\mathrm{d}V_G} \;=\; C_i\frac{W}{L}\mu_D(G) + C_i\frac{W}{L}\frac{\mathrm{d}\mu_D(G)}{\mathrm{d}V_G}(V_G - V_T). \tag{7.12}$$

In the on-state this gives $\mathrm{d}G/\mathrm{d}V_G = C_i\frac{W}{L}\mu_D$, as it should be. In order to determine the drift mobility μ_D, we take the second derivative $\mathrm{d}^2G/\mathrm{d}V_G^2$. Neglecting the third order term, we have $\mathrm{d}^2G/\mathrm{d}V_G^2 \approx 2\,C_i\frac{W}{L}\mathrm{d}\mu_D/\mathrm{d}V_G$. Substitution in Eq. (7.12) gives for the drift mobility

$$\mu_D(G) \;\approx\; \frac{L}{C_iW}\frac{\mathrm{d}G}{\mathrm{d}V_G} - \frac{1}{2}\frac{L}{C_iW}\frac{\mathrm{d}^2G}{\mathrm{d}V_G^2}(V_G - V_T). \tag{7.13}$$

This result allows us to experimentally determine the variation of the ratio $\tau_f/(\tau_f+\tau_t)$ as a function of gate voltage (cf. Eq. (7.3)).
This approach works well, regarding the correspondence with the mobility value from the noise data in Fig. 7.5 and with N in Fig. 7.6. Apparently, keeping the derivatives of the conduction up to the second order is sufficient for a realistic determination of N and μ_D. Despite the complex physics of the sub-threshold regime, our calibration with the diffusion noise data

shows that the standard current-voltage relationship Eq. (7.2) with a varying mobility Eq. (7.13) holds satisfactorily.

7.5 Discussion

7.5.1 Diffusion noise phenomenon

Well documented examples of diffusion noise are rare. In semiconductor literature only a few examples of diffusion noise are reported [15]. The reason is that relaxation of carriers is generally dominated by other processes such as drift, generation and recombination or $1/f$ noise. Indeed, the noise spectra in Fig. 7.3 show a transition from diffusion dominated noise to $1/f$ noise when the gate voltage is increased. We do observe the usual $1/f$ noise in the on-state of the *a*-Si:H transistor [72, 74, 77]. Owing to the lithographic fabrication of a contact pattern which sets the W/L ratio to 950, large currents could flow which enabled noise measurements in the sub-threshold regime of TFTs. Consistent with Hooge's law, the $1/f$ noise observed in the above-threshold regime is proportional to $1/N$, like diffusion noise. From this we may conclude that the transition from $1/f$ noise into diffusion noise when the gate voltage is decreased, is caused by the decrease of μ_D in the sub-threshold regime characteristic for amorphous semiconductors.

7.5.2 Mobility values

When we compare the value of the drift mobility $\mu_D \approx 0.3$ cm^{2}V^{-1}s^{-1} (for T=295, 330 and 363 K) with the estimate for the microscopic mobility μ_0 in *a*-Si:H of 10 cm^{2}V^{-1}s^{-1} [1], we arrive at $\tau_f/(\tau_t + \tau_f)$ of 0.03. For the datasets measured at 295, 330 and 363 K, the values of D_{eff} found are around 0.01 cm^{2}s^{-1} (see Fig. 7.5), which would lead to a kink around 130 Hz. Unfortunately, a kink around that frequency can not be observed due to suppression of the noise by the RC-time of the detection system, which is in the same range.
The 417 K-data are found to have smaller values of the mobility, due to a smaller values of $\tau_f/(\tau_t + \tau_f)$, which was confirmed independently by direct determination of the mobility from conduction measurements only. Also, the dependence on V_G is stronger for the 417 K-data. The explanation for the quantitative differences with the data measured at 295, 330 and 363 K is the threshold shift due to gate stressing before the 417 K-data set was measured.

We have found that the direct determination of both μ_D and N using conduction measurements only results in values which are for the larger part within the error of values from the combination of noise intensity and conduction. Therefore we propose Eq. (7.13) as a quick approach to determine the mobility in the near- and sub-threshold regime.

7.6 Conclusion and outlook

We find in an *a*-Si:H TFT operated in the sub-threshold range, that the $1/f$ noise becomes buried under 1D diffusion noise, because the drift mobility decreases. Theoretical 1D diffusion noise spectra in that regime fit well to the measured spectra, and explain the observed $f^{-1/2}$ branch in the low-frequency region of the spectrum. Combined noise and conduction measurements enable to separate and determine in the sub-threshold regime both the number of electrons N and the drift mobility $\mu_D \approx 0.3$ cm^{2}V^{-1}s^{-1}. A decrease of the gate voltage in the sub-threshold regime leads obviously to a decrease of the number of electrons, and further to the a decrease in the ratio $\tau_f/(\tau_t+\tau_f)$, observed as a decrease of μ_D. The calculated ratio between μ_D and μ_0 is consistent with the results from conduction measurements only and with the literature value of the microscopic mobility μ_0=10 cm^{2}V^{-1}s^{-1}. The noise spectra in the sub-threshold regime can consistently and quantitatively be described by 1D diffusion noise. Noise measurements enable the separate determination of the number of electrons in the channel and the drift mobility. Especially in the sub-threshold regime, where the conduction deviates from the usual behavior, this leads to valuable results. It turns out that application of the standard current-voltage relation for a field-effect transistor with a mobility that is allowed to vary is in agreement with a procedure using combined noise and conduction measurements. We finally remark that the noise spectra after a small (1V) threshold shift still satisfy 1D diffusion noise spectra.
It would be interesting to carry out noise measurements in the sub-threshold regime of polycrystalline Si TFTs, to investigate the contribution of diffusion noise in relation to other kinds of noise. The W/L ratio of the TFTs should exceed 500 to be able to measure noise in the sub-threshold regime. Another interesting suggestion is to carry out measurements on a TFT with a two-dimensional channel, which should result in a spectrum which is devided in three regions of different spectral slopes [89].

References

[1] R. Street, *Hydrogenated amorphous silicon*, Cambridge University Press, Cambridge, 1991.

[2] N. Mott and E. Davis, *Electronic Processes in Non-crystalline Materials*, Clarendon Press, Oxford, 2 edition, 1979.

[3] N. Ashcroft and N. Mermin, *Solid state physics*, Hartcourt Brace College Publ., New York, 1976.

[4] P. Thomas and H. Overhof, *Properties and Applications of Amorphous Materials*, pages 261–290, NATO Science Series, Kluwer, 2001.

[5] J. van Hapert, PhD thesis, Utrecht University, 2002.

[6] D. Staebler and C. Wronski, Appl. Phys. Lett **31**, 292 (1977).

[7] M. Powell, S. Deane, and R. Wehrspohn, Phys. Rev. B **66**, 155212 (2002).

[8] H. Branz, Phys. Rev. B **59**, 5498 (1999).

[9] S. Deane, R. Wehrspohn, and M. Powell, Phys. Rev. B **58**, 12625 (1998).

[10] R. Wehrspohn, S. Deane, I. French, and M. Powell, J. Non-Cryst. Solids **266-269**, 49 (2000).

[11] G. Munyeme, PhD thesis, Utrecht University, 2003.

[12] M. Stutzmann, M. Brandt, and M. Bayerl, J. Non-Cryst. Solids **266-269**, 1 (2000).

[13] M. Powell and S. Deane, Phys. Rev. B **48**, 10815 (1993).

[14] M. Powell and S. Deane, Phys. Rev. B **53**, 10121 (1996).

[15] A. van der Ziel, *Noise in Solid State Devices and Circuits*, Wiley and Sons, New York, 1986.

[16] M. Kirton and M. Uren, Adv. Phys. **38**, 367 (1989).

[17] K. van Vliet and J. Fassett, *Fluctuation Phenomena in Solids, ed. R.E. Burgess*, chapter 7, Academic Press, New York, 1965.

[18] P. Dutta, P. Dimon, and P. Horn, Phys. Rev. Lett. **43**, 646 (1979).

[19] K. Lee, K. Amberiadis, and A. van der Ziel, Solid State Electronics **25**, 999 (1982).

[20] F. Hooge, IEEE Trans. Electron Dev. **41**, 1926 (1994).

[21] P. Dutta and P. Horn, Rev. Mod. Phys. **53**, 497 (1981).

[22] D. Quicker and J. Kakalios, Phys. Rev. B **60**, 2449 (1999).

[23] J. Belich and J. Kakalios, Phys. Rev. B **66**, 195212 (2002).

[24] J. Belich and J. Kakalios, to be published, SPIE Conf. Proc.

[25] L. Lust and J. Kakalios, Phys. Rev. Lett. **75**, 2192 (1995).

[26] H. Overhof and W. Beyer, Philos. Mag. B **43**, 433 (1981).

[27] J. Fan and J. Kakalios, Phys. Rev. B **47**, 10903 (1993).

[28] D. Quicker, P. West, and J. Kakalios, Mat. Res. Soc. Proc. **467**, 73 (1997).

[29] C. Parman and J. Kakalios, Phys. Rev. Lett. **67**, 2529 (1991).

[30] P. Verleg, PhD thesis, Utrecht University, 1997.

[31] G. Snyder, M. Weissman, and H. Hardner, Phys. Rev. B **56**, 9205 (1997).

[32] M. Günes, R. Johanson, and S. Kasap, Phys. Rev. B **60**, 1477 (1999).

[33] R. Johanson, D. Scansen, and S. Kasap, J. Vac. Sci. Technol. B **17**, 73 (1999).

[34] R. Johanson, S. Kasap, F. Gaspari, D. Yeghikyan, and S. Zukotynski, J. Vac. Sci. Technol. A **18**, 661 (2000).

[35] M. Günes, R. Johanson, S. Kasap, J. Yang, and S. Guha, J. Non-Cryst. Sol. **299-302**, 425 (2002).

[36] S. Kasap et al., J. Mat. Sc., in press, 2003.

[37] E. Ullersma, PhD thesis, Utrecht University, 1998.

[38] A. D'Amico, G. Fortunato, and C. van Vliet, J. Non-Cryst. Solids **77-78**, 499 (1985).

[39] M. Bacoicchi, A. D'Amico, and C. van Vliet, Solid-St. Electron. **34**, 1439 (1991).

[40] F. Bathaei and J. Anderson, Phil. Mag. B **55**, 87 (1987).

[41] P. Verleg and J. Dijkhuis, Phys.Rev. B **58**, 3904 (1998).

[42] P. Verleg and J. Dijkhuis, Phys. Rev. B **58**, 3917 (1998).

[43] S. Reynolds, C. Main, and M. Rose, J. Non-Cryst. Solids **227-230**, 233 (1998).

[44] C. Main, S. Reynolds, and R. Badran, Mat. Res. Soc. Symp. Proc. **715**, A2.2 (2003).

[45] S. Kasap, 2003, personal communication.

[46] R. Schropp, personal communication.

[47] R. Schropp and M. Zeman, *Amorphous and microcrystalline silicon solar cells; modeling, materials and device technology*, Kluwer, Boston, 1998.

[48] S. Fonash, *A manual for AMPS-1D for Windows 5/NT; a one-dimensional device simulation program for the analysis of microelectronic and photonic structures*, Pennsylvania State University, 1997, see also http://www.psu.edu/dept/AMPS.

[49] P. McElheny, J. Arch, H. Lin, and S. Fonash, J. Appl. Phys. **64**, 1254 (1988).

[50] M. Zeman, M. Kroon, and J. van den Heuvel, *Amorphous Semiconductor Analysis (ASA)*, Delft Univerity of Technology, Delft, the Netherlands, user manual version 3.0 edition, 1999.

[51] M. van Veghel, Master's thesis, Utrecht University, 1999.

[52] M. von der Linden, PhD thesis, Utrecht University, 1994.

[53] C. van Vliet, J. Appl. Phys. **93**, 6068 (2003).

[54] C. van Vliet, IEEE Transactions **41**, 1902 (1994).

[55] A. van der Ziel, *Solid State Physical Electronics*, Prentice-Hall, 3rd edition, 1976.

[56] J. Fassett, *Electronic fluctuations in solids involving thr transport, generation, and recombination of charge carriers*, PhD thesis, Univ. Minnesota, Minneapolis, USA, 1962.

[57] J. Bakker, P. van Capel, B. Fine, and J. Dijkhuis, Mat. Res. Soc. Symp. Proc. **715**, A2.6 (2003).

[58] B. Shklovskii and A. Efros, *Electronic properties of doped semiconductors*, volume 45 of *Springer Ser. Solid-State Sciences*, Springer, Heidelberg, 1984.

[59] V. Arkhipov and G. Adriaenssens, Phil. Mag. B **76**, 11 (1997).

[60] V. Arkhipov and G. Adriaenssens, Phys. Rev. B **54**, 16696 (1996).

[61] F. Zhong and J. Cohen, Phys. Rev. Lett. **71**, 597 (1993).

[62] P. Anderson, Phys. Rev. **109**, 1492 (1958).

[63] B. Fine, J. Bakker, and J. Dijkhuis, Accepted for publication in Phys. Rev. B (2003).

[64] A. van Rheenen, G. Bosman, and R. Zijlstra, Solid-St. Electron. **30**, 259 (1987).

[65] G. Khera and J. Kakalios, J. Appl. Phys. **56**, 1918 (1997).

[66] D. Adler and E. Yoffa, Phys. Rev. Lett. **36**, 1197 (1976).

[67] J. Wei, M. Sun, and S. Lee, Appl. Phys. Lett. **71**, 1498 (1997).

[68] R. Weisfield, J. Appl. Phys. **59**, 6401 (1982).

[69] V. Cech, Solid-state Electronics **41**, 81 (1997).

[70] W. O'Mara, *Liquid crystal flat panal displays: manufacturing, science and technology*, Van Nostrand Reinhold, New York, 1.ed. edition, 1993.

[71] J. Xu, P. Lai, and Y. Cheng, J. Appl. Phys. **86**, 5203 (1999).

[72] M. Valenza et al., J.Appl.Phys. **79**, 923 (1996).

[73] J. Rhayem, M. Valenza, D. Rigaud, N. Szydlo, and H. Lebrun, J. Appl. Phys. **83**, 3660 (1998).

[74] J. Rhayem, D. Rigaud, M. Valenza, N. Szydlo, and H. Lebrun, J. Appl. Phys. **87**, 1983 (2000).

[75] C. Dimitriadis, J. Brini, G. Kamarinos, V. Gueorguiev, and T. Ivanov, J. Appl. Phys. **83**, 1469 (1998).

[76] C. Angelis et al., Appl. Phys. Lett. **74**, 3684 (1999).

[77] J. Boudry and L. Antonuk, J. Appl. Phys. **76**, 2529 (1994).

[78] M. Deen, S. Rumyantsev, and J. Orchard-Webb, J. Vac. Sci. Technol. B **16**, 1881 (1998).

[79] L. Vandamme, R. Feyaerts, G. Trefán, and C. Detcheverry, J. Appl. Phys. **91**, 719 (2002).

[80] F. Hooge, Phys. Lett. A. **29**, 139 (1969).

[81] K. Hung, P. Ko, C. Hu, and Y. Cheng, IEEE Trans. Electron Devices **ED-37**, 654 (1999).

[82] G. Ghibaudo, O. Roux, C. Nguyen Duc, F. Balestra, and J. Brini, Phys. Status Solidi A **124**, 571 (1991).

[83] D. Cobden and B. Muzykantskii, Phys. Rev. Lett. **75**, 4274 (1995).

[84] R. Keijsers, O. Shklyarevskii, and H. van Kempen, Phys. Rev. Lett. **77**, 3411 (1996).

[85] M. Peters, J. Dijkhuis, and L. Molenkamp, J. Appl. Phys. **86**, 1523 (1999).

[86] B. Stannowski and R. Schropp, Thin Solid Films **383**, 125 (2001).

[87] B. Stannowski, PhD thesis, Utrecht University, 2002.

[88] S. Sze, *Physics of semiconductor devices*, John Wiley and Sons, New York, 2nd edition, 1981.

[89] R. Voss and J. Clarke, Phys. Rev. B **13**, 556 (1976).

Summary

Noise measurements on two classes of semiconductor devices are reported in this thesis: on solar-cell devices and thin-film transistors. The aim is to provide a quantitative description of the experiments. The first class of devices displays one of the most intruiging physical phenomena in semiconductors: $1/f$ noise. The term refers to resistance fluctuations with a $1/f$ frequency dependence of the noise intensity. This kind of noise is reported in many different systems but lacks a universal explanation. Hydrogenated amorphous silicon (*a*-Si:H) is an example of a semiconductor which is known to exhibit a large degree of disorder, and, as a result, a large variation in microscopic energy barriers, that govern capture and emission of charge carriers. Two mechanisms to explain the observed $1/f$ resistance noise in *a*-Si:H devices are investigated: generation-recombination noise and potential fluctuations at defects. The latter mechanism appears to yield a quantitative prediction of the noise spectra.

We study the electronic properties of hydrogenated amorphous silicon. This material finds an application in the two studied classes of devices: solar cells and thin-film transistors (TFTs). These devices have the unfortunate property to degrade upon prolonged light-soaking and gate bias stressing, respectively. In order to study the properties of undoped *a*-Si:H, relevant for solar cells, an intrinsic layer is sandwiched between thin doped layers, resulting in *nin* and *pip* device structures. Chapter 2 of this thesis deals with current density - voltage (J-V) characteristics, which are nearly Ohmic at low voltages ($<$0.15 V) and gradually become superlinear at high voltages due to the presence of space charge. A simulation program takes band bending into account and was applied to fit J-V characteristics measured at different temperatures simultaneously. As a result, the defect density, the energy position, and width of the Gaussian distributions of deep defects are obtained. These material parameters are used as input parameters in two quantitative theories to describe the observed noise in *nin* devices.

The first mechanism, generation-recombination (g-r) noise, is addressed in Chapter 3. G-r noise originates from local emission and capture events between traps and the conduction band (in case electrons are the majority carriers). Using Green's function theory, g-r noise is calculated for a one-dimensional semiconductor device with traps, taking due account of carrier transport. Although capture and emission times are in the right (ms) range, the calculated noise intensity turns out to be five to six orders of magnitude below the measured noise level and thus is negligible. Clearly, another noise source must cause the $1/f$ noise in *a*-Si:H. The observations turn out to be explained very well by a microscopic mechanism treated in Chapter 4. The timescale of the fluctuations is again the capture or emission time for deep defects. But now it is used, when an electron is emitted or captured, that the charge state of a deep defect fluctuates. As a result, the potential around that defect will fluctuate, depending on the degree of screening by surrounding defects and the contacts. Free electrons will instantaneously adjust to the fluctuating local potential. That adjustment causes a carrier number fluctuation, which is measured as a voltage fluctuation in presence of a constant current. Our theory treats fluctuations of charged deep defects in the presence of screening by surrounding defects and the contacts using the equilibrium description of defects. Since there is only a small number of (randomly located) deep defects which is able to change their charge state, the potential landscape exhibits long-range fluctuations.
The theory predicts the noise *intensity* accurately, without any adjustable parameters. The *shape* of the noise spectrum is fitted by two parameters of the potential landscape. The complete temperature dependence of the noise spectra is consistently described by a Gaussian distribution of potential barriers, located 0.27 ± 0.05 eV above the conduction band edge, and with a halfwidth of 0.09 ± 0.02 eV. These material parameters, obtained with noise spectroscopy, cannot be obtained from other (electrical) measurement techniques. In Chapter 5 experiments on different devices are explained by the theory of long-range potential fluctutations. The area and thickness dependence is examined, the absence of an isotope effect is demonstrated and *pip* devices are studied, where holes are the majority carriers. The comparison of the results obtained from the *pip* and *nin* devices demonstrates the existence of a universal distribution of emission barriers in *a*-Si:H/D for the carrier escape from deep defects.
In Chapter 6 the relation between degradation and noise is studied in *nin* devices. Additional conductivity measurements are analyzed to determine the defect density before and after degradation. After degradation, the cur-

vature of noise spectra is unaffected, while the intensity increases by a small factor. These observations are consistent with the theoretical predictions using the measured increase of the defect density. The potential landscape does not seem to change significantly upon degradation, as judged from the constant shape of the spectra. The theory of long-range potential fluctuations successfully and quantitatively predict the $1/f$ noise spectra in our films of *a*-Si:H and most likely in other materials with regions of poor screening.

Noise measurements on *a*-Si:H TFTs are described in Chapter 7. Earlier experiments revealed $1/f$ noise which satisfied Hooge's empirical law in the on-state of the transistor. We were able to measure noise in the subthreshold regime of the transistor. At the threshold voltage and below, diffusion noise dominates over $1/f$ noise. Diffusion of electrons through the one-dimensional channel is identified as the source of the noise. The number of free electrons as determined from combined noise and conduction measurements is in quantitative agreement with the usual approximation from conduction measurements only. As expected, the drift mobility extracted from the combined noise and conduction data varies with the conditions of the channel, and amounts to 0.3 $cm^2V^{-1}s^{-1}$ near threshold.

Samenvatting voor niet-vakgenoten

> 'Morfografisch amorf,' mompelde professor Prlwytzkofski al schrijvend. 'Der fenomeen is niet uit kristallijnen opgebouwd en kan deswegen niet existeren. Toont echter ener buitenordentelijk accomodatievermogen, dat nader studeerd worden moet.'
> *- De Kon Gruwer, Marten Toonder (1971)*

In dit proefschrift staan elektrische fluctuatiemetingen aan een ingewikkeld materiaal centraal. Het gaat om de halfgeleider amorf silicium waarin waterstof is opgenomen. Het is een wanordelijk materiaal, in tegenstelling tot kristallijn silicium, waar de silicium atomen netjes gerangschikt zijn. In amorf silicium bevinden de atomen zich op verschillende afstanden van elkaar. Er bestaan ook plaatsen waar zelfs geen bindingen tussen de silicium atomen bestaan. Op die plaatsen blijven bungelende bindingen over, die 'defecten' worden genoemd. Het proces waarbij door externe factoren, zoals sterke en langdurige belichting, het aantal defecten in een monster vergroot wordt, heet degradatie. Een halfgeleider kan licht absorberen, waarbij zowel positieve als negatieve lading vrijgemaakt wordt. Dit principe is toegepast in een zonnecel, waarin vrijgemaakte deeltjes met tegengestelde lading van elkaar gescheiden worden hetgeen tot een elektrische spanning leidt. Een andere belangrijke toepassing van amorf silicium is de dunne laag transistor of TFT structuur, wel gebruikt in flat-pannel displays. Een transistor is niets anders dan een elektonische schakelaar. Ook al zijn er technologische verbeteringen denkbaar in de genoemde bestaande gelaagde structuren of devices, toch is deze studie er niet op gericht om daarvoor praktische oplossingen aan te dragen. Het doel van dit werk is om fluctuaties kwantitatief te meten en te beschrijven. Zodoende kan meer vat gekregen worden op het complexe, wanordelijke materiaal en de gevolgen van degradatie op de

eigenschappen van het materiaal. Er worden twee meetmethoden en diverse analysemethoden uit de kast gehaald. In meerdere gevallen moest een bestaande theorie worden toegepast op de omstandigheden van de devices. In één geval werd een complete theorie van de grond af aan opgebouwd. Ter ondersteuning van de ruismetingen, die centraal staan in dit proefschrift, dienen metingen van de elektrische geleiding. Met geleidingsmetingen in een groot temperatuurbereik kan het aantal geleidingselektronen in het monster worden gemeten, alsmede de gemiddelde energie benodigd voor thermische overbrugging van de barrière voor geleiding.
De eigenlijke fenomenen waarvan studie gemaakt is, zijn de weerstandsfluctuaties. Elektrische fluctuaties worden gemeten als ruis in de spanning in een variant van de zonnecel en in een transistor. Het ruissignaal wordt versterkt en omgezet naar de frequentie componenten die er in zitten. Dit ruisspectrum geeft precies weer hoe sterk het materiaal ruist bij bepaalde frequenties. In de praktijk gaat het om zwakke signalen, waarin vaak microscopische verschijnselen verborgen zijn. Het is de uitdaging om de intensiteit en de vorm van de gemeten ruisspectra te kunnen begrijpen. De eerder genoemde geleidingsmetingen zijn daarbij handig, omdat ze dezelfde toestand karakteriseren waaronder ruismetingen worden verricht. Geleidings- en ruismetingen hangen echter op een andere manier af van de elektrische eigenschappen van het materiaal. Door de meetgegevens te combineren kan een completer beeld van de elektrische eigenschappen van het materiaal verkregen worden.
In Hoofdstuk 2 staat beschreven hoe een simulatieprogramma gebruikt is om een deel van de elektrische eigenschappen van een device te achterhalen. Op deze manier kan de verdeling van bungelende bindingen gekarakteriseerd worden. Zoals gezegd zijn deze defecten plekken in het netwerk, waar silicium niet gebonden is aan een ander silicium atoom of waterstof. Dergelijke defecten leveren geladen toestanden op in het materiaal, waar bewegende lading op terecht kan komen (vangst) en van waaruit lading kan ontsnappen (emissie). Deze processen vormen de basis van twee verschillende theorieën.
Het ruistype waar lokale vangst- en emissie processen leiden tot fluctuaties aan de contacten, wordt generatie-recombinatie ruis genoemd (Hoofdstuk 3). De intensiteit van dit type ruis blijkt ver beneden het waargenomen niveau van $1/f$ ruis uit te komen. Er moet dus een andere oorzaak voor het fenomeen zijn. Die oorzaak is gevonden in de fluctuaties van de lokale elektrische potentiaal, ten gevolge van ladingsveranderingen van defecten, op de tijdschaal van dezelfde vangst- en emissieprocessen. Die processen

worden gekarakteriseerd door het energieverschil tussen het defect en de locale barrière voor emissie. De sterkte van deze potentiaalfluctuaties hangt af van de afscherming van lading door naburige defecten (Hoofdstuk 4). Zowel de fluctuatiefrequenties als de ruisintensiteit blijken goed overeen te komen met de metingen. Metingen in het gehele temperatuurbereik kunnen beschreven worden met behulp van één verdeling van potentiaal barrières. Daarmee komen we op een essentiëel ingrediënt van de nieuwe theorie: dat de willekeurige ordening van de atomen leidt tot een landschap van potentiaalbergen en -dalen. Met ruismetingen is het mogelijk om dit landschap te beschrijven - wat onmogelijk is voor geleidingsmetingen, die slechts voor de dalen (de geleidingsband) gevoelig zijn. Een reeks experimentele resultaten, beschreven in Hoofdstuk 5, ondersteunt deze theorie. Zo worden de effecten ten gevolge van een andere laagdikte goed voorspeld, en is er geen afhankelijkheid van het gebruikte isotoop van waterstof. Anders gezegd, gebruik van zwaar waterstof in plaats van het gebruikelijke waterstof had geen invloed op de ruismetingen. Uit een experiment met positieve ladingsdragers blijkt dat het potentiaallandschap er vrijwel hetzelfde uitziet als het landschap voor elektronen. Het degradatie experiment, beschreven in Hoofdstuk 6, laat zien dat bij een geringe toename van de aantallen defecten de ruisintensiteit nauwelijks toeneemt en qua vorm gelijk blijft. De lichte stijging is in overeenstemming met de theorie. De ongewijzigde vorm van het spectrum zou erop kunnen duiden dat het potentiaallandschap niet essentieël verandert in de aanwezigheid van meer defecten. Met de theorie van potentiaalfluctuaties is een bevredigende verklaring gevonden voor de ruismetingen aan amorf silicium. Omdat het beschreven mechanisme gebaseerd is op algemene natuurkundige beginselen, is het waarschijnlijk dat het ook in andere (halfgeleider) systemen op zal treden. En dan met name in die gebieden, waar een zwakke mate van afscherming bestaat, net als in het bestudeerde materiaal. Ruismetingen bevatten dus unieke informatie over het potentiaal landschap, dat ongevoelig voor degradatie lijkt te zijn. Daarmee is aanvullende experimentele informatie gewonnen in een belangrijk onderzoeksveld.

Naast bovenstaand onderzoek werden ruismetingen uitgevoerd aan dunne laag transistoren bestaand uit amorf silicium (Hoofdstuk 7). Transistoren zijn elektronische schakelaars, die met behulp van een spanning de zogenaamde 'gate' (hek) geschakeld worden. Het is bekend dat dit type transistor $1/f$ ruis produceert in de situatie dat het hek open staat. We hebben met name metingen gedaan in de buurt van de drempelspanning, als er een kleine stroom door het geleidende kanaal loopt. In die toestand

blijken elektronen aanleiding te geven tot fluctuaties zodra ze het kanaal overgestoken zijn volgens de gang van een dronken man. Dit zogenaamde 'diffusief transport' in de lengterichting van het kanaal bepaalt dus het ruisspectrum. De vorm van een diffusie ruisspectrum wordt gekarakteriseerd door een scherpe overgang tussen twee gebieden met een verschillende frequentie-afhankelijkheid. Er is kwantitatieve overeenstemming tussen het aantal elektronen bepaald uit de geleiding en uit een theoretisch diffusieruisspectrum. Daardoor kan de parameter die het gemak aangeeft waarmee elektronen door het materiaal diffunderen met zekerheid gegeven worden. Dit is de (drift) mobiliteit, en deze bedraagt 0.3 $cm^2V^{-1}s^{-1}$ bij het openen van de gate (het hek). Deze waarde klopt aardig met de bepaling op grond van de geleiding, en is bovendien in overeenstemming met de mobiliteit die in het algemeen gevonden wordt. Met ruismetingen kan de mobiliteit - een maatgevende grootheid voor de industrie - nu ook bepaald worden in de buurt van de drempelspanning van een transistor.

Dankwoord

Niet alleen het onderwerp, maar zeker ook de samenwerking met anderen vormden voor mij ruim vier jaar lang de motivatie voor dit onderzoek. Aan het uiteindelijke resultaat hebben velen een belangrijke bijdrage geleverd, waarvoor ik hen graag op deze plaats wil bedanken.
Mijn promotor prof. Jaap Dijkhuis dank ik voor zijn goede ideëen, zijn enthousiasme en zijn durf met betrekking tot het opzetten van grensverleggende experimenten. Zijn kritische houding bleek steeds weer waardevol, met name in onze discussies, waarin hij graag de rol van 'advocaat van de duivel' speelde. Ten slotte wist hij ingewikkelde zaken terug te brengen tot de essentie, waar ik veel van opgestoken heb.
Voor het inwijden in de ruisspectroscopie dank ik Frans Wollenberg. Met zijn uitgebreide kennis op het gebied van electronica en daarbuiten wist hij voor al mijn vragen praktische oplossingen aan te dragen. Samen met Paul Jurrius zijn prachtige flexibele meetopstellingen tot stand gekomen, waarvoor veel dank aan beide heren. De laatst genoemde 'heer van het goede leven' wist op het mechanische en sociale vlak alles soepeltjes te laten verlopen.
Met de theoretisch onderzoeker dr. Boris Fine deelde ik mijn interesse voor $1/f$ ruis in amorf silicium. Hij wist een theoretische afleiding van meer dan 100 formules te produceren die de uiteindelijke verklaring van onze ruismetingen bleek te leveren. Boris, bedankt voor je scherpzinnigheid, je precisie en je grote theoretische bekwaamheid. Ook kijk ik terug op een onvergetelijk Russisch feest bij jou en Ada thuis.
Bij prof. Ruud Schropp en dr. Jatin Rath stond de deur altijd open voor vragen omtrent amorf silicium. Voor het verzorgen van met name de depositie van het dure 'zwaar waterstof', amorf silicium, alsmede de gelegenheid deel te nemen aan de werkbesprekingen ben ik hen zeer erkentelijk. De kennis en kunde op het gebied van dunne laag transistoren van dr. Bernd Stannowski zijn van groot belang geweest voor het ruisexperiment aan die transistoren.

De basis voor alle devices werd gelegd door Karine van der Werf, die de vele lagen deponeerde, rekening houdend met mijn specifieke wensen.
De ruimtevaart-technologen Marcel de Bruin, Nanny Snijder, Ward Haalebos en Marcel Ridder (SRON, Utrecht) dank ik voor het sputteren van uitstekende elektrische contacten. Ook mocht ik frequent gebruik maken van de laagdiktemeetfaciliteit. In een verkennend stadium waren Johan Keijzer en Gert Hartman behulpzaam bij het opdampen van contacten. Voor de speciale contactering van de dunne-laag transistoren ben ik dank verschuldigd aan Philips Redhill, GB.
De Nederlandse Amerikanen, prof. Van Vliet en prof. Bosman ben ik zeer erkentelijk voor hun bezoek in Utrecht en hun waardevolle aanwijzingen met betrekking tot verschillende ruistheorieën. For interesting discussions I would like to acknowledge dr. Main, dr. Reynolds, prof. Kakalios, prof. Stutzmann and prof. Adriaenssens. Voor de interesse in mijn werk dank ik prof. Van der Weg en prof. Habraken.
Met veel plezier heb ik met de chemici samengewerkt aan een ambitieus experiment: ruis in een elektrochemische cel. Aan de chemie met prof. Kelly, prof. Vanmaekelbergh, dr. Erik Bakkers en dr. Marcel di Vece heeft het niet gelegen, evenmin aan de mooie opstelling! Helaas bleken de tijdschalen van de bestudeerde processen in één geval te snel en in een ander geval te traag te zijn.
De ervaring en de kennis van mijn jaargenoot Marijn van Veghel op het gebied van computersimulaties van amorf silicium structuren waren zeer welkom bij de aanvang van de promotie. Bedankt voor je nuttige adviezen. Ook heb ik veel gehad aan de werkgroep "opzet en analyse van experimenten met behulp van statistische technieken", mede dankzij de bijdragen van Gijsje Koenderink, Bas Feddes en Elwin de Wolf.
Ik heb het altijd heel leuk gevonden om met studenten op onderzoek uit te gaan. Allereerst met Bernard van der Horst, die met succes zijn tanden heeft gezet in een lastig onderwerp: fotogeleiding. Zijn kritische houding en zijn toewijding heb ik zeer gewaardeerd. Met Peter van Capel heb ik op vele onderzoeksterreinen van gedachten gewisseld. Voor zijn inzet, lef en inzichten ben ik hem dankbaar. Daarnaast hebben we veel lol beleefd aan het geëxperimenteer op de politieke aandelenmarkt. Timon van Wijngaarden heeft in korte tijd een leuke combinatie van bestaande methoden gemaakt, petje af. Ook bedankt voor jullie gezellige aanwezigheid op de kamer.
Voor controle-berekeningen aan het device ben ik Raul Jiminez Zambrano en Geoffrey Munyeme dankbaar. Bij hen kon ik terecht voor gesprekken over amorf silicium of geheel andere onderwerpen. Arnoud Witt dank ik

voor het lezen van een gedeelte van mijn proefschrift. Voor waardevolle reacties op werkbesprekingen en conferenties zou ik een hele waslijst aan mensen kunnen noemen, maar ik beperk me tot Otto Muskens, Dima Mazurenko, Marjolein van der Voort, Ruurd Lof en Anke Brockhoff. Gedurende vier jaar in de Debye AiO Commissie heb ik met plezier samengewerkt met Tonnis, Marije, Aarnoud, Marieke, Anne, Harm, Gijsje, Claire, Nilesh, Reza en Didi.
Mijn kamergenoten Marjolein van der Voort en later Lennart Karssen stonden garant voor een prettige werksfeer. Met Clarien Derks kon ik over van alles en nog wat praten. Die gezelligheid zal ik missen. Een speciale noot voor al diegenen die zich met grote veerkracht hebben ingezet voor de interne verhuizing, met name Cees de Kok, Paul Jurrius en Gerard van Lingen.
De verhuizing bracht ook een geleidelijke verschuiving en verbreding van het vakgroepsleven met zich mee. Denkend aan de prettige sfeer van de afgelopen jaren noem ik met name, en met inbegrip van hen die al eerder genoemd werden, de fysici Peter, Michiel, Dries, Erik, Richard, Carolijn en Toine. Verder de chemici Andries, Hans, Stefan, Zeger, Stephen, Paul, Sander, François, Harold, Peter, Ageeth en Liesbeth. En ten slotte de colloidfysici Alfons, Arnoud, Carlos, Didi, Christina en Alexander. Onder lunchtijd heb ik samen met andere spelletjes-freaks Tim, Jeroen, Marijn, Beat, François, Peter en Pim talloze bordspellen uitgeprobeerd.
Mijn familie en vrienden dank ik voor hun interesse in mijn werk. In het bijzonder dank ik mijn schoonouders voor hun meelevendheid en betrokkenheid. Ik wil mijn ouders bedanken omdat ze mij hebben gestimuleerd in de richting die ik gegaan ben. Mams, fijn dat je steeds zo betrokken was, en dat je echt wilde weten waar ik nu mee bezig was. Paps, bedankt dat je er op belangrijke momenten voor me was.
Lieve Mirjam, het was super dat ik jou steeds aan mijn zijde vond in de afgelopen periode, waarin je geduld aardig op de proef gesteld werd. Het was een worsteling om in woelige tijden het hoofd boven water te houden, maar het is ons gelukt!

Curriculum Vitae

De schrijver van dit proefschrift werd op 16 februari 1976 geboren in Oss. Na het behalen van het VWO-diploma (cum laude) op de Christelijke Scholengemeenschap Melanchthon te Rotterdam in 1994, begon hij aan de studie Natuur- en Sterrenkunde aan de Universiteit Utrecht. In december 1998 werd het doctoraalexamen Experimentele Natuurkunde aan de Universiteit Utrecht met genoegen afgelegd. Het laatste jaar van zijn doctoraalstudie bestond uit een onderzoek naar de oxidatie van ijzer bij de sectie Grenslaagfysica (Universiteit Utrecht) en een stage bij Shell Solar te Helmond. Op 1 januari 1999 trad hij in dienst bij de faculteit Natuur- en Sterrenkunde van de Universiteit Utrecht als assistent in opleiding bij de sectie "Atom Optics and Ultrafast Dynamics"van het Debye Instituut. De resultaten van het onderzoek zijn beschreven in dit proefschrift en gepresenteerd op een drietal conferenties: 'the International Conference on Amorphous and Microcrystalline Semiconductors' (Nice, Frankrijk, 2001 en Campos do Jordão, Brazilië, 2003) en 'Spring Meeting of the Materials Reseach Society' (San Fransisco, VS, 2002). Tevens werd de zomerschool 'Properties and applications of amorphous materials' bezocht (Sec, Tjechië, 2001). Naast het onderzoek begeleidde hij tweedejaars studenten bij het hoofdvak natuurkunde, en was hij actief binnen de Debye AiO Commissie.